FACULTY OF SCIENCE
UNIVERSITY OF COPENHAGEN

A Thesis Presented for the Degree of
Cand. Scient. in Geophysics

Particulate air pollution and its characteristic sources in the high Arctic at Station Nord, N.E. Greenland

Anna Groth Grube

Internal supervisor Peter Ditlevsen,
Center for Ice and Climate
Niels Bohr Institute (NBI)
University of Copenhagen

External supervisor Andreas Massling
External co-supervisors Henrik Skov,
Lise Lotte Sørensen and Jacob K. Nøjgaard
Department of Environmental Science
Aarhus University

Niels Bohr Institute (NBI)
University of Copenhagen
Denmark
September 1, 2011

AARHUS UNIVERSITY

Abstract

The present project uncovers the characteristics of particulate Arctic air pollution and its sources at the high Arctic at Station Nord, N.E. Greenland with special attention to Black Carbon.
The purpose was approached by analysing *Black Carbon* (BC) concentrations measured with a *Particle Soot Absorption Photometer* (PSAP) in the time period from March 2008 to April 2011 at Station Nord. This measurement show a seasonal variations in accordance with the Arctic haze cycle (maximum in winter and early spring). An exceptional high BC event ($110\,\mathrm{ng\,m^{-3}}$) was found to occur in the early spring of 2008 with subsequent years reaching a low winter concentration (about $60\,\mathrm{ng\,m^{-3}}$). This exceptional high BC event was found coincide with a strong Polar Vortex (high indices of the *Arctic Oscillation* (AO) and the *North Atlantic Oscillation* (NAO) mode). An additional analysis of BC concentrations from Flade Isblink ice core covering the time period 1950 to 2000 verifies to some extent the trend of high BC events during high positive winter modes of AO and NAO.

Filter samples were analysed for *Organic Carbon* (OC) and *Elemental Carbon* (EC) by a *carbon analyser* (OC EC analyser) in the time period from July 2008 to February 2011. The mean concentrations are found for OC ($0.11\pm0.08\ \mu\mathrm{g\,m^{-3}}$), EC ($0.01\pm0.01\ \mu\mathrm{g\,m^{-3}}$) and *Total Carbon* (TC) ($0.12\pm0.08\ \mu\mathrm{g\,m^{-3}}$). The relative contribution of EC to TC is found to 11 ± 8 %. Furthermore, EC concentrations and the *sulphate* (SO_4^{2-}) concentrations analysis by *Ion Chrometography* (IC) were studied and found to have similar seasonal patterns as BC concentrations. An analysis of the correlation between EC and the light absorption coefficient reported from PSAP resulted in a specific absorption coefficient $\sigma_{specific} = 7.82\,\mathrm{m^2\,g^{-1}}$, which is in agreement with literature.

The total chemical dataset retrieved by *the Proton Induced X-ray Emission* (PIXE) method together with BC and SO_4^{2-} was analysed by the *COnstrained Physical REceptor Model* (COPREM) in order to investigate sources and source apportionment at Station Nord. The results of this analysis show that the anthropogenic sources, combustion and metal industry are the main contributors to BC concentrations. Further, metal industry contributes with the largest fraction to the source apportionment in early spring. The same pattern is found for SO_4^{2-} with a small contribution from marine sources in late autumn and winter.

Preface

Many people have contributed with help and advice to my master thesis at Niels Bohr Institute (NBI), University of Copenhagen, devised in collaboration with the Department of Environmental Science, Aarhus University. I am very grateful for all the people who have supported me through my last year of study both supervisors, colleagues, friends and family.

I would like to thank my two formal supervisors; internal supervisor Associate Professor Peter Ditlevsen and external supervisor Senior Scientist Andreas Massling, but also external co-supervisors Henrik Skov, Lise Lotte Sørensen and Jacob K. Nøjgaard, for supervising me throughout this study. Thank you for always being there through emails and taking me into the group. Being in your group was a giving experience. Special thanks to Henrik Skov for always taking time to answer questions and confronting the problem. Furthermore, I would like to thank the staff at the Department of Environmental Science, Aarhus University, and great thanks are particularly owed to PhD student Quynh Nguyen and Research Technician Bjarne Jensen.

Particularly, a great thanks to Rajani Møller Hansen and Stephanie Østblom for giving me feedback on my writing. In addition, a great thanks to; my fellow students at the office at NERI for making the long days not seem that long; my colleagues at TV2 Vejrcenter and at the Centre for Ice and Climate; my sail racing team in J80, as well as the guys in CB66 for believing in me and making this year successful and unforgettable.

I am very thankful to my family, especially my parents Gitte & Jørgen Grube, for supporting me and made me go to the Summer School Alpbach 2010 when I needed it the most. Your love and support has brought me to where I am today, and it gives me the courage to always move forward.

Particularly, a great thanks to my friends for their patience and support. I would therefore like to express my gratitude to Joanna Levinsen, Nynne Lauritsen and Julie Spanggaard for believing in me and encouraging me to pursue my dreams. Thank you!

Contents

Chapter 1

Introduction

The Earth's climate system has a high variability due to a multiplicity of factors such as the shortwave radiation from the sun, the Earth's rotation rate and orbital characteristics. One important factor is the chemical composition of the atmosphere and the interaction between the atmosphere and other components of the Earth's climate system, because these factors greatly determine the fluxes of mass, energy and momentum at the Earth surface. The atmospheric composition can be damped by external forces e.g. emissions through human activity. The effect of such external forced variability depends on the amplitude of the forcing as well as the sensitivity of the climate system. Since the late 1970's carbon dioxide (CO_2) has reieved much attention in the scientific world due to its effect as a greenhouse gas, whereas short-lived climate forcers e.g. *Black Carbon* (BC), ozone (O_3) and methane (CH_4) have long been considered to be of marginal importance to global climate change.

In the last decade the scientific world has realized the importance of short-lived climate forcers on the Earth's radiation budget and particularly on the Arctic radiation budget. Here BC has gained the greatest interest due to its strong effects on the radiative balance in the Arctic. BC is the most efficient atmospheric particulate specie to absorb visible light, which results in a warming effect of either the surface-atmosphere aerosol column or at altitudes above and within the BC-haze layer. BC consists of a mixture of other chemical compounds, such as sulphate, and therefore the overall effect of BC-haze layer depends on other chemical species present in the BC-haze layer as well as the albedo of the underlying surface [Quinn et al., 2011].
Like other aerosols, BC influence the microphysical properties of cloud droplets and thus clouds. A strong presence of cloud-active BC particles increases the cloud droplet number and decreases the size of the droplets, which results in a corresponding increase in shortwave cloud albedo, and hence a cooling at the surface. In addition, aerosol-cloud interactions can also result in longwave forcing and hence a warming at the surface.

Another important forcing mechanism caused by BC aerosol particles result from deposition on snow or ice covered surface. Such a deposition enhance the absorption of shortwave radiation at the surface, which can warm the lower atmosphere and result in snow or ice melting. The Arctic environment is among the most sensitive to such climate changes as warming and ice melting on a global scale. Therefore, knowledge regarding the magnitude of forcing due to BC aerosol particles as well as the Arctic BC-haze layer is of great importance in a global attempt to prevent global warming and ice melting.

1.1 Objectives of this study

Accurate modelling of the radiative forcing due to Arctic aerosols requires an adequate knowledge of the spectral properties and spatial and temporal variability of the aerosol. This is in great contrast to the limited measurements of Arctic aerosols and their characteristics.
Several monitoring sites have been established since the 1980's in the Arctic region. Only a few of those monitoring sites have a long-term record of Arctic aerosol properties and together with aircraft measurements of the vertical structure of aerosols they represent the limited knowledge of Arctic Haze aerosols in the Arctic. Those measurements give valid characteristics of aerosols, which are needed for model validation and quantification in order to improve estimates and results of the modelling of the Arctic aerosol's radiative forcing.

The aim of this thesis is to identify and analyse characteristics of Arctic air pollution and its sources at Station Nord in order to increase and improve knowledge regarding processes involving BC aerosol particles and to improve the estimate of radiative forcing on the Arctic radiation budget. This leads to the following main research questions for this thesis:

- What are the meteorological characteristics and how do they affect the transport pathways of particulate Arctic air pollution at Station Nord?
- What are the characteristics of particulate Arctic air pollution at Station Nord, north-eastern Greenland, and are they consistent over the years?
- What types of sources contribute to particulate Arctic air pollution at Station Nord, and how are they distributed over the year?

To answer the first research question the meteorological conditions were studied by analysing the 500 mb geopotential height-contours in the northern hemisphere from autumn 2007 to spring 2011. These analysis were performed in order to study the strength of the Polar Vortex, which is associated with high pollution levels.
In order to answer the second research question, measurements collected from March 2008 to April 2011 by the *Particle Soot Absorption Photometer* (PSAP) at Station Nord were analysed and interpreted together with different elements also reported from Station Nord.
To answer the third research question, a source to receptor analysis was composed

using the COPREM (COnstrained Physical REceptor Model), where the investigated Black Carbon concentrations were used as input parameters. The applied COPREM is a simple hybrid model that unifies qualities from factor analytic models and chemical mass balance.

Chapter 2

Properties and effects of aerosol particles

This chapter will first introduce air pollution in a historical perspective. Thereafter the basic concept and processes in atmospheric aerosol chemistry, with emphasis on the chemistry of black carbon and sulphate. The following section is dealing with climate feedback due to the role of aerosol particles on the radiation budget. Finally, a section which covers the role of aerosol particles in the Arctic and the chemical elements and their sources found within the Arctic.

2.1 Historical perspective on air pollution

Humans have been aware of airborne particles since ancient history, but associate black carbonaceous particles with coal combustion was first realised in the medieval Europe [Giere and Querol, 2010]. By recognising this, health effects due to black smoke became an important subject for King Edward I of England (17 June 1239 - 7 July 1307). He may have enforced the first air pollution law by declaring that burning coal would be punished by death and at least one man was executed for violating the law [Giere and Querol, 2010].
Despite this law smoke pollution kept increasing, especially during the industrial revolution. At the very end of the industrial revolution one of history's most famous air pollution episodes occurred in December 1952 in London, of-

Figure 2.1: Traffic during London's infamous "Great Smog" episode in December 1952 [Giere and Querol, 2010]

ten known as the "Great Smog" (Figure 2.1). During this event cold air moved from the English Channel across London and produced a well-developed temperature inversion, which induced a dense mixture of polluted air and fog. "The smog was so thick that people had to grope their way along the streets, buses crawled along at a walking pace led by pedestrians with flashlights, and indoor events were cancelled because the stage could not be seen" [Wallace and Hobbs, 2006].
Visibility degradation is probably the most dominating impact of air pollution. This visibility degradation occur because of absorption and scattering of light by both gases and particles, where the last-mentioned is the most important phenomenon in the atmosphere. However, the smoke persisted for five days and by the time the smog had lifted, approximately 4000 people had died of respiratory problems, but the related medical conditions implied that 8000 people died in the months that followed.

Particulate matter has a high impact on human health, especially in large cities due to high exposure levels. There appears to be an increasing risk of lung cancer and mortality with increasing concentration of particulate matter, especially with diameters below 2.5 µm [AMAP 2006]. This is due to the fact that small size particles can penetrate deeper into the smaller airways of the lungs. It is very difficult to associate health effects with individual pollutants, because other pollutants, such as SO_2 and O_3 increase with increasing concentrations of particulate matter [Wallace and Hobbs, 2006]. In addition, the current weather situation also play a significant role together with exposure level.
In general the Arctic perspective of health effects is the same as the global perspective, but with an addition of point sources related to heavy metallic industrial activity, especially due to the metallurgical industry in Siberia, Russia [AMAP 2006]. However, studies of health effects due to heavy metals have been unable to show any significant health effects that are directly related to emissions from the nickel refineries [AMAP 2006].

Particulate matters which affect the human health and the visibility can have an anthropogenic as well as a natural origin. Some natural emissions have a grate potential to affect our society on a short time scale as well as a long time scale. An example is volcanic eruptions, wildfires and dust storms which greatly can reduce visibility and affect transportation systems worldwide such as the eruption of the volcano at Eyjafjallajokull, Iceland, in April 2010. The eruption of the volcano at Eyjafjallajokull reminded the people of Europe that pollutants can be transported over large distances with a relatively small dilution. This is also the case in the Arctic where long-range anthropogenic pollution often is associated with an air pollution episodes known as *Arctic haze*.

2.1.1 Arctic Haze

The Arctic atmosphere was long believed to be extremely clean. However, Arctic explorers in the late 19th century and early 20th century had noticed atmospheric haze and dirty deposits on the snow. Arctic haze was first noticed in the 1950's by pilots in the Canadian high Arctic who began using the term *Arctic haze* to describe

this smog, which caused limited visibility on the horizon and was most prominent in early spring. In the beginning it was believed to be a natural phenomenon caused by dust particles. The idea that Arctic haze was due to anthropogenic sources was first realised in 1970s. It was surprising since it was widely believed that aerosols were generally not transported more than a few hundreds of kilometers from its source region [K. et al., 2006].

Arctic haze is a persistent, brown haze with a varying mixture of sulphate and *particulate organic matter* (POM) and, to a lesser extent, ammonium, nitrate, dust aerosols and black carbon [Heidam, 1984; Heidam et al., 1999]. Arctic haze is also rich in heavy metals which originate from industrial sources and it is furthermore related to relatively high levels of ozone precursors, such as *nitrogen oxides* (NOx) and *volatile organic compounds* (VOCs) [Heidam et al., 2004, 1999; K. et al., 2006; Law and Stohl, 2007].
The Arctic haze layer has a seasonal pattern with a maximum in tropospheric aerosol concentrations in late winter and early spring and a minimum concentration in summer; "*Arctic haze cycle*". In general, the haze starts disappearing in April close to the surface, but layers at higher altitudes can persist until May [Law and Stohl, 2007].
A study of Arctic haze layer by Engvall et al., 2009 found the particles as fine particles dominated by particles in the accumulation-mode size ranges [Engvall et al., 2009]. This mode is associated with processes of condensation and coagulation, which affects the size distribution and its mixing state. This size range is very efficient at scattering visible solar radiation since the peak in the particle surface-area size distribution is near the maximum efficiency for Mie scattering, see section 2.5. Besides the scattering, the haze layer consiste of weakly absorbing material due to presence of BC particles, and it is actually this absorption that has an effect on the radiation budget within the Arctic. Furthermore, it is the combination of scattering and absorbtion in the haze layer that result in reduced visibility reported by pilots [Seinfeld and Pandis, 2006].

2.2 Properties of atmospheric aerosols

Atmospheric particles emitted directly into or formed within the atmosphere are generated by both natural processes and human activity. Particles emitted directly are known as *primary particles* and particles formed in the atmosphere by gas-to-particle conversion processes are known as *secondary aerosols*. Although atmospheric particles are derived mostly from sources that are spatially and temporally confined they are found globally due to atmospheric transport and mixing. Most particles are found in the troposphere, where a significant fraction is of anthropogenic origin [Seinfeld and Pandis, 2006]. This gives a highly non-uniform geographic distribution with varying concentrations and composition of tropospheric aerosols over the Earth. To some extent, atmospheric particles are also found in the stratosphere, but only limited and often related to the frequency of very big volcanic eruptions.
Solid particles and liquid droplets in the atmosphere are referred to as *particulates* or *particulate matter (PM)*. In contrast, the term *aerosol* defines the suspension

of fine solid or liquid particles in a gas, which usually refers to the aerosol as the particulate component only [Seinfeld and Pandis, 2006].

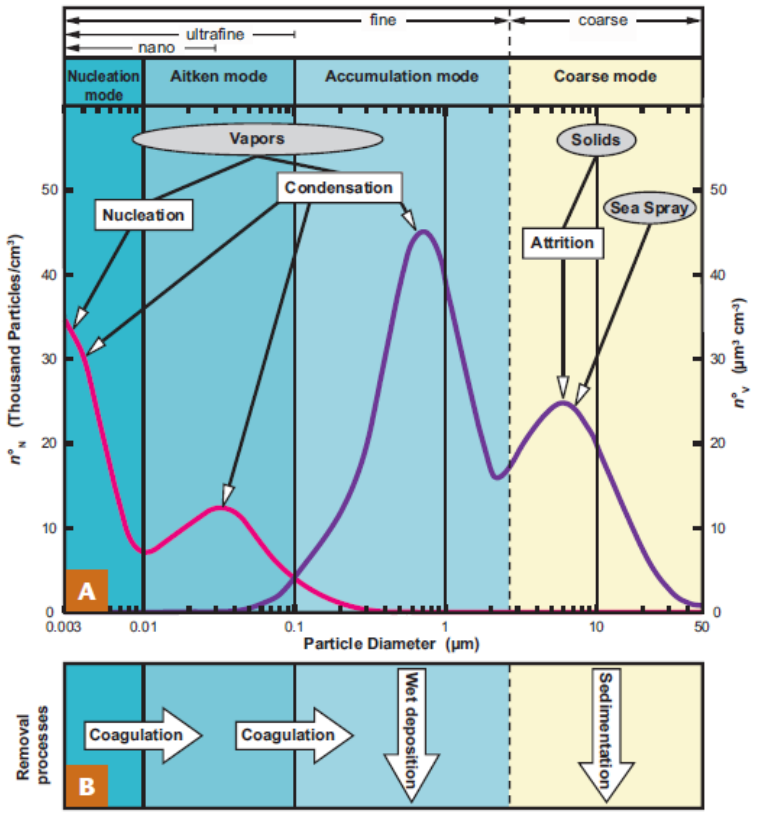

Figure 2.2: A) The different size range and modes particles can be divided into. Furthermore, the typical size distribution of the number ($n°_N$, Pink line) and the volume ($n°_v$, Purple line) of atmospheric particles per cm^3 of air. The sources of particles are shown in grey ellipses, where the transformation processes of particles are shown in white rectangles with associated arrows. B) Shows particle removal processes [Giere and Querol, 2010].

Atmospheric or airborne particles can change size and composition by various processes. The different processes and phenomena related to the particles sizes are illustrated in figure 2.2. Aerosol particles can change size and composition by the following processes:

- Coagulation with other particles, which is produced by Brownian motion or as a result of motion produced by hydrodynamic, electrical or gravitational forces.
- Chemical reaction, which transforms the mixing state and chemical composition of the aerosol particles
- Condensation of vapour species or by evaporation.
- Activation of droplets in the presence of supersaturation, where particles work as *cloud condensation nuclei (CCN)* and grow into fog and cloud droplets.

Different size distributions of aerosol particles lead to different behaviour within the above described processes and phenomena. Therefore, aerosol particles can be divided into different modes related to their size range as shown in figure 2.2.
Particles $\gg 2.5\,\mu m$ in diameter refers to particles in the *coarse* mode, where particles less than $2.5\,\mu m$ in diameter refers to particles in the *fine* mode. The *fine* mode is further divided into 3 sub-modes; the *nucleation (or nuclei)* mode, which are particles with diameters less than $0.01\,\mu m$; the *aitken* mode, which spans the size range from about $0.01\,\mu m$ to $0.1\,\mu m$ ($100\,nm$); the *accumulation* mode, which are particles with a diameter from $0.1\,\mu m$ to $2.5\,\mu m$. The first two modes account for the main part of particles by number, but due to their small size these particles only account for a small percent of the total mass [Seinfeld and Pandis, 2006].

In the nucleation and aitken modes particles are formed from condensation of vapour during combustion processes and from nucleation of atmospheric species to form particles. The primary removal processes from the atmosphere, of particles at this size range, are by coagulation with larger particles. In the accumulation mode the particles originate from the nuclei mode and from condensation of vapours onto existing particles. This cause the particles to grow into the size range of the accumulation mode. The removal mechanisms in this size range are least efficient, which also gives rise to the name of the accumulation mode. The particles found in the coarse mode is often formed by mechanical processes such as attrition due to friction which form natural dust particles. These particles are removed by sedimentation and have large sedimentation velocities, which result in a short residence time in the atmosphere.

In general, the removal processes of aerosol particles from the atmosphere to the surface of land or seabed are expressed in terms of wet and dry deposition. *Dry deposition* is deposition at the Earth's surface e.g. removal by sedimentation, where *wet deposition* is an expression for aerosol particles incorporated in a cloud droplet and thereby removed by precipitation. Wet and dry deposition lead to a relatively short residence times of aerosol particles in the troposphere.
Typically aerosol particles have a residence time in the troposphere from a few days to a few weeks, where atmospheric trace gases have lifetimes ranging from less than a second to a century or more [Seinfeld and Pandis, 2006].

2.3 Carbonaceous aerosol particles

Carbonaceous particles exist in the atmosphere either as insoluble particles or in mixtures that are considered as partly soluble, which makes those carbonaceous aerosol particles more or less efficiently removed by dry and wet deposition processes. Carbonaceous aerosol particles are often found in the atmosphere as fine particles [Andreae and Gelencser, 2006] and often divided into two major components: *elemental carbon* (EC) and *organic carbon* (OC). EC represent the carbon content which has similar chemical structure as impure graphite and when it is emitted into the ambient air it immediately cluster together and form aggregates as shown in figure 2.3.

OC represent all the organic compounds or material, which often is emitted directly (primary OC) or form by condensation of low-volatile products of the photo-oxidations of hydrocarbons (secondary OC) [Seinfeld and Pandis, 2006]. Secondary OC starts its atmospheric life in the gas phase as a *Volatile organic compound* (VOC) e.g. *formaldehyde* (CH_2O), undergoes chemical transformation in the gas phase into a less volatile compound and finally transfer to the particulate phase by condensation or nucleation.

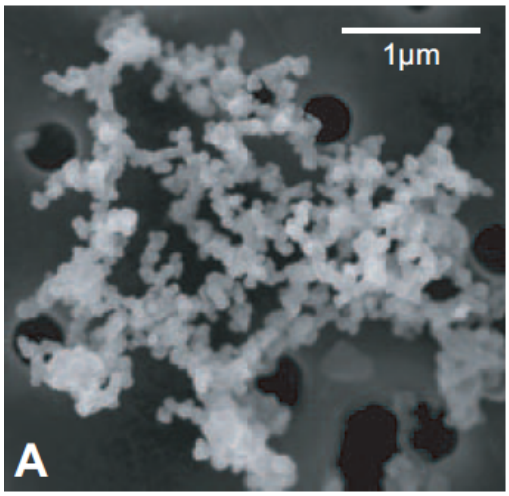

Figure 2.3: Scanning electron microscope images of typical aggregate of soot particle [Giere and Querol, 2010].

In general, atmospheric carbonaceous aerosol particles can be viewed as a mixture of EC, OC and small amounts of other elements such as oxygen, nitrogen and hydrogen incorporated in its graphitic structure. The exact size and morphology of the clusters varies widely with a chain size of up to a few micrometres (Figure 2.3) [Seinfeld and Pandis, 2006]. Furthermore, the exact chemical composition of the aggregate depends strongly on the chemical and thermal environment under which they are formed and on the time available for ageing [Andreae and Gelencser, 2006]. In general, an aggregate is the most stable form and therefore residents for transformation regarding heat and oxidation processes.

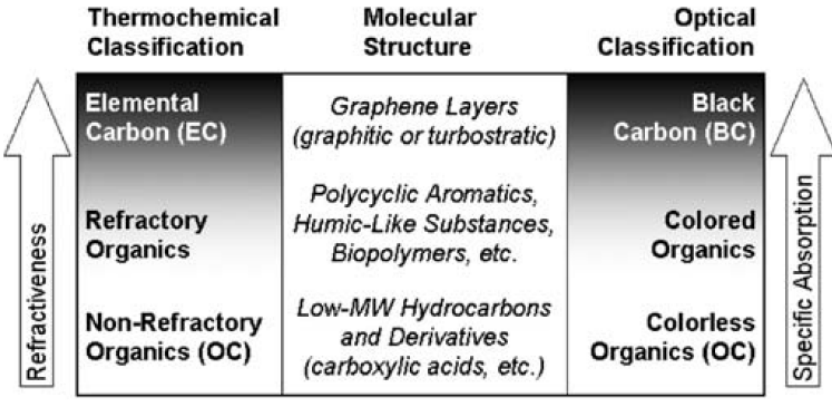

Figure 2.4: Classification and molecular structure of carbonaceous aerosol components, where the specific absorption increase with a more pronounced graphitic structure [Pöschl, 2003].

The exact use of the term EC or OC depends on the applied thermochemical method. The term *BC* or *soot* are often used in relation with optical methods and

represent the EC with a pure uniform graphitic structure which result in a higher specific absorbance as illustrated in figure 2.4. In comparison a carbonaceous aerosol particle with a more organic structure has a decrease in the refractiveness and the specific absorption. In general, an atmospheric carbonaceous aerosol particle consist of a mixture of elements which lead to some deviation in the optical methods from reality. Therefore can the light absorbing BC concentrations reported from optical method only be regarded as approximation or estimate for the actual concentration of the pure elemental carbon particles in the atmosphere.

2.3.1 Ageing of carbonaceous aerosol particles

Atmospheric carbonaceous aerosol particles can be transformed by ageing processes either physically or chemically. Physical processes include the *condensation* of sulphuric and nitric acid onto the BC particle, and *coagulation* with more soluble aerosols such as sulphates and nitrates.

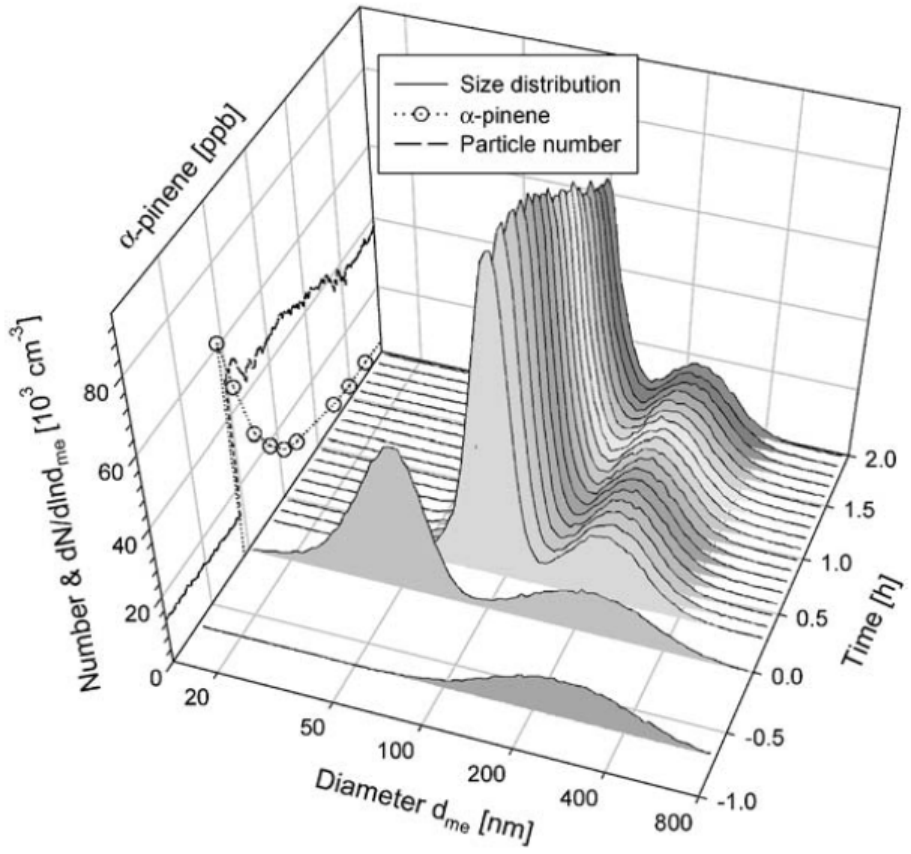

Figure 2.5: Change of the size distribution and number concentration of soot formed by ozonolysis of α-pinene. Here the size distribution of α-pinene is seen as the first peak (Diameter $20\,\mathrm{nm}$ to $50\,\mathrm{nm}$) and the soot size distribution is seen as the subsequent peak (Diameter $150\,\mathrm{nm}$ to $400\,\mathrm{nm}$). The significant narrowing of the fractal dimension of soot particles is clearly seen after coating with α-pinene in the time interval of $0.0\,\mathrm{h}$ to $2.0\,\mathrm{h}$ [Saathoff et al., 2003].

Chemical processes that may age the BC particles include *oxidation* of organic coatings by *Hydroxyl radicals* (OH). Condensation, coagulation and oxidation determine the ageing process and thereby change the mixing state, size distribution and the solubility of the BC particles.

In an experiment by Saathoff et al. [2003] soot particles were coated with products of the α-pinene ozonlysis (Figure 2.5). α-pinene ozonlysis is found to be one of the major atmospheric sources of *secondary organic aerosol (SOA)* formation. The result from this experiment proves that the coating coasted changes of the agglomerate structure by an increase of the fractal dimension (2.5) and a more compact soot agglomerates (2.6). The change in fractal dimension is seen in figure 2.5, where the change in size distribution of α-pinene at time 0.0 h is seen as the first peak (Diameter 20 nm to 50 nm) and the change in size distribution of soot is seen as the subsequent peak (Diameter 150 nm to 400 nm). In the following time (0.0 h to 2.0 h) after the coating event a significant narrowing occurred in the fractal dimension of soot. The coating also resulted in a more compact soot agglomerate (Figure 2.6), which enhance the sedimentation, but decrease the coagulation rate. Furthermore, it was also found that the deposition of more hygroscopic condensable ozonlysis products of α-pinene on soot agglomerates results in an increase of the *hygroscopic growth factor (HGF)* and thus enhance the ability to act as a CCN [Saathoff et al., 2003].

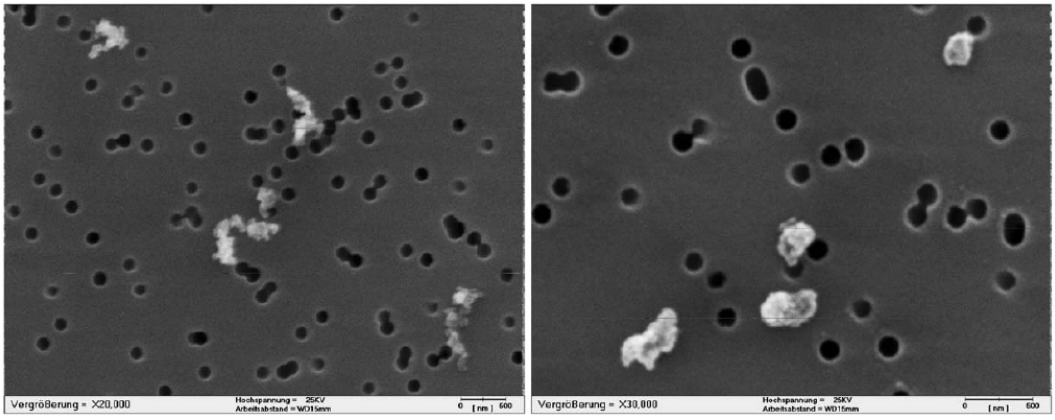

Figure 2.6: Images from a electron micrographs of soot particles before (left) and after coating (right) with α-pinene oxidation. Here is the compaction of soot agglomerates clearly seen [Saathoff et al., 2003].

Fresh smoke BC particles tend to form more open structures [Andreae and Gelencser, 2006], which are more prone to transformation by ageing processes and to become more hygroscopic. However, particles associated with biomass combustion are usually present as much larger spherical and compacted aggregates, which seem to be more resistant to atmospheric ageing processes [Andreae and Gelencser, 2006]. In addition, the growth processes in a smoke layer within the first 1-4 days is known to be dominated by condensation and coagulation/gas-to-particle conversion, and thereafter dominated by coagulation [Engvall et al., 2009].

2.4 Sulphate aerosol particles

Sulphur species are present in the Earth's crust, ocean and atmosphere, but in the atmosphere sulphur is found in a more reduced state. The most important reduced sulphur compounds are *Hydrogen sulfide* (H_2S), *Dimethyl sulfide* (DMS), *Carbon disulfide* (CS_2), *Carbonyl sulfide* (OCS) and *sulphur dioxide* (SO_2) [Seinfeld and Pandis, 2006]. The sulfides have both anthropogenic and natural sources.

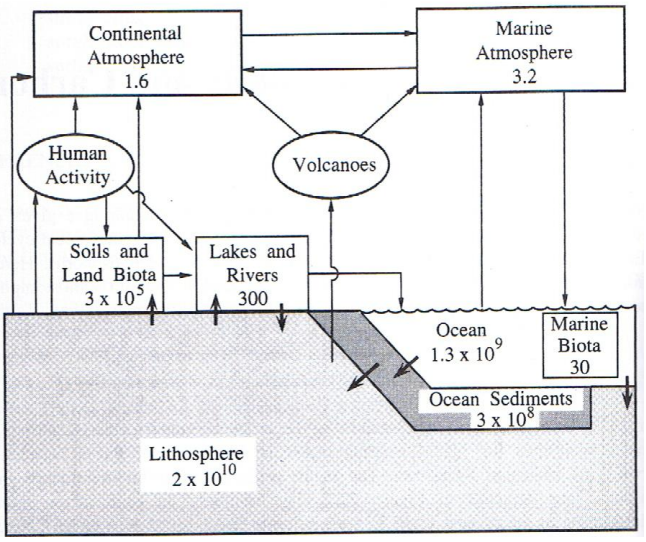

Figure 2.7: Major reservoirs and burdens of sulfur in [Tg(S)], the directions of fluxes between the reservoirs are indicated [Seinfeld and Pandis, 2006].

The anthropogenic sources are dominated by fossil fuel combustion, where SO_2 is the predominant sulphur-containing air pollutant. The natural sources are dominated by biogenic reactions in soils, marshland, plants and ocean.
In figure 2.7 are the major reservoirs in the sulphur cycle shown and the estimated amount of sulphur in [Tg(S)] for each reservoir is noted. It is seen that the largest amount of sulphur in the atmosphere is found above the ocean. This is related to biogenic reactions in the oceans due to marine phytoplankton, which produce *Dimethyl Sulfide* (DMS), *carbonyl sulfide* (OCS) and *Carbon disulfide* (CS_2) [Seinfeld and Pandis, 2006; Wallace and Hobbs, 2006].
The DMS (CH_3SCH_3) dominates the emissions of sulphur from the oceans and react with OH or NO_3 radicals to form SO_2 (Figure 2.8). Then OH can react with SO_2 to form *sulphate* (SO_4^{2-}). In general, the OH radical is restricted in the Arctic troposphere due to lack of sunlight in the Arctic winter, which makes the reaction with NO_3 more favorable:

$$CH_3SCH_3 + NO_3 \longrightarrow CH_3SCH_2 \cdot + HNO_3 \tag{2.1}$$

which leads to formation of CH_3S into OCS. OCS can then transform into SO_2 in order to form SO_4^{2-}. This is most abundant in the stratosphere as illustrated in figure 2.8 [Seinfeld and Pandis, 2006].

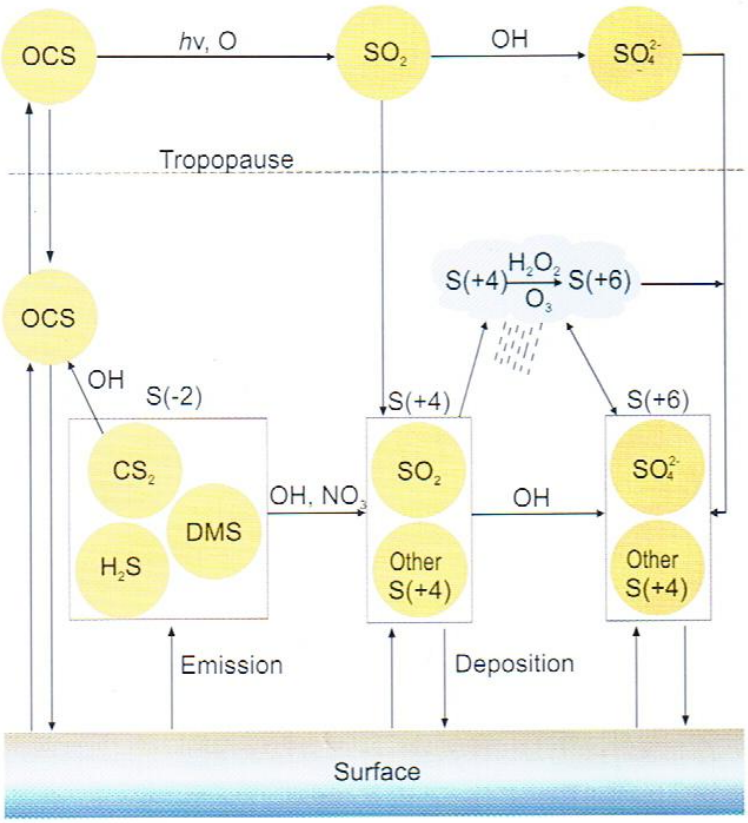

Figure 2.8: The atmospheric cycle for sulphur compounds [AMAP 2006].

In figure 2.8 the atmospheric sulphur cycle is shown. This cycle is dominated by OH radical reactions, which reacts with e.g. sulphur dioxide and lead to production of the gas aqueous/aerosol *Sulfuric acid* (H_2SO_4). Under normally atmospheric conditions in the troposphere sulphur dioxide can react in both the gas and aqueous phase and be removed by dry or wet deposition. Here with respect to the gas-phase the following reaction occur:

$$SO_2 + OH\cdot + M \longrightarrow HOSO_2 \cdot + M \tag{2.2}$$

followed by the generation of HO_2 radical:

$$HOSO_2 \cdot + O_2 \longrightarrow HO_2 \cdot + SO_3 \tag{2.3}$$

when sulphur trioxide can be converted to sulfuric acid in the presence of water vapour:

$$SO_3 + H_2O + M \longrightarrow H_2SO_4 + M \tag{2.4}$$

With respect to the aqueous-phase the following reaction occur:

$$SO_2(aq) + H_2O_2 \longrightarrow H_2SO_4 \tag{2.5}$$

Most of the sulfides in the troposphere are oxidized rapidly by the OH radicals, therefore are the lifetimes in the atmosphere of those compounds only typically days to a week, but one exception is OCS [Wallace and Hobbs, 2006]. OCS is very

stable in the troposphere and therefore has a relatively long residence time ($\approx$ 2 years). The long residence time of OCS enables it to be mixed into the stratosphere, where it can photolyse ($h\nu$) or react with elemental oxygen (O) in order to form SO_2. Then it is subsequently converted to H_2SO_4 aerosols, as shown is figure 2.8 [Seinfeld and Pandis, 2006; Wallace and Hobbs, 2006].

2.4.1 Direct and indirect effects of aerosols

Atmospheric aerosol particles affect the climate system by 3 different physical mechanisms. Firstly, they scatter and absorb solar radiation. Secondly, they scatter, absorb and emit longwave radiation. Thirdly, they act as *cloud condensation nuclei* (CCN) and *ice nuclei* (IN). The two first mechanisms are the direct effects and the last one is referred to as the indirect effect.
The *direct effect* depends on size, abundance, optical properties of the particles and to some extent the underlying surface layer. In general, most aerosol species, such as sulphate, nitrate, sea-salt, dust[1] backscatter the solar radiation, whereas black carbon aerosols absorb the radiation. The scattering and absorption of radiation due to direct effect is illustrated in figure 2.9.
Scattering aerosols exert a net negative direct *radiative forcing* (RF), while partially absorbing aerosols exert a negative *Top Of the Atmosphere* (TOA) direct RF over dark surfaces, such as oceans or dark forest surfaces, and a positive TOA RF over bright surfaces such as deserts, snow and ice or above clouds.
Both positive and negative TOA direct RF mechanisms reduce the shortwave irradiance at the surface. The longwave direct RF is only substantial if the aerosol particles are large and occur in large concentrations at higher altitudes [IPCC 2007]. In addition, absorption of solar radiation by aerosols leads to heating of the ambient air, which can result in evaporation of cloud droplets. This process is referred to as *semi-direct effect*.
The *indirect effect* is defined as the overall process by which aerosols perturb the earth-atmosphere radiation balance by modulation of cloud albedo and lifetimes of clouds. Aerosol particles acting as CCN depends on the presence of supersaturation in the ambient environment as well as the micro-physical properties which are a function of size, chemical composition and mixing state.

[1] dust is a partly absorbing aerosol

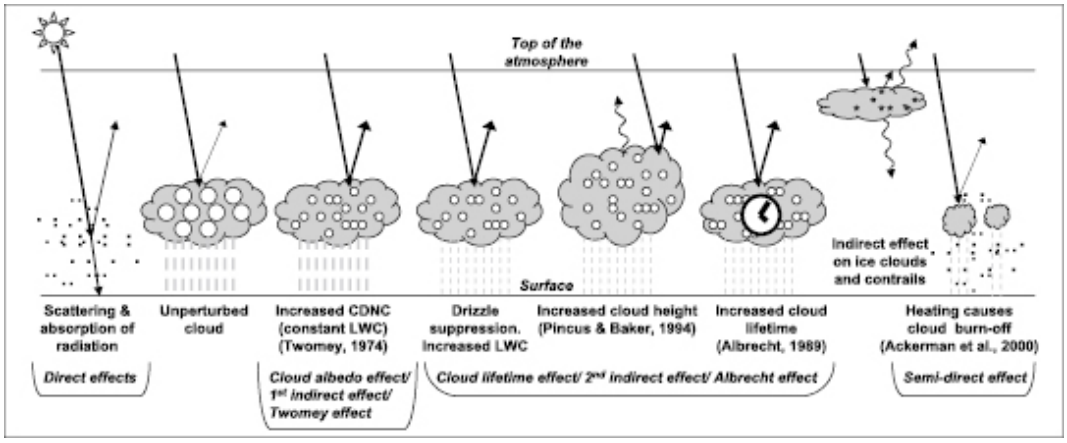

Figure 2.9: The different mechanisms associated with aerosols as CCN and the associated effect on clouds [IPCC 2007]. Here small black dots represent aerosols and circles cloud droplets. CDNC stands for *Clouds Droplet Number Concentrations*.

Figure 2.9 show the mechanisms associated with the indirect effect of aerosols as CCN. The small black dots are the aerosols and the circles are cloud droplets. The straight lines represent the outgoing or ingoing shortwave radiation, where wavy lines are associated with longwave radiation.
If the aerosol number concentrations are high then this will increase the concentration of CCN and thereby increase the number of droplets. This type of cloud has a high concentration of droplet with smaller radius which contributes to a higher cloud albedo. If the opposite is the case (low concentration of CCN) a low concentration of droplets with larger radius will make the cloud albedo lower. This again affects the lifetime of the cloud. A larger radius of the droplets inside the cloud will lead to a decrease in lifetime due to the gravitational force affecting the droplets. Furthermore, the change in concentration and size of cloud droplets is also expected to change the areal extent of the cloud [IPCC 2007].

2.4.2 Effects of aerosols on the climate system in the Arctic

The Arctic is thought to be very sensitive to changes in radiative fluxes imposed by aerosols and other short-lived climate forcers [AMAP 2006; IPCC 2007]. Especially aerosols that impose a surface forcing which may trigger regional climate feedback and lead to a melting of the ice in the Arctic. In addition, an elaboration of the consequences due to Arctic warming is described in chapter 3.1.
In figure 2.10 the forcing mechanisms on the Arctic radiation budget is shown for both the direct and the indirect effect, which is explained in the following.

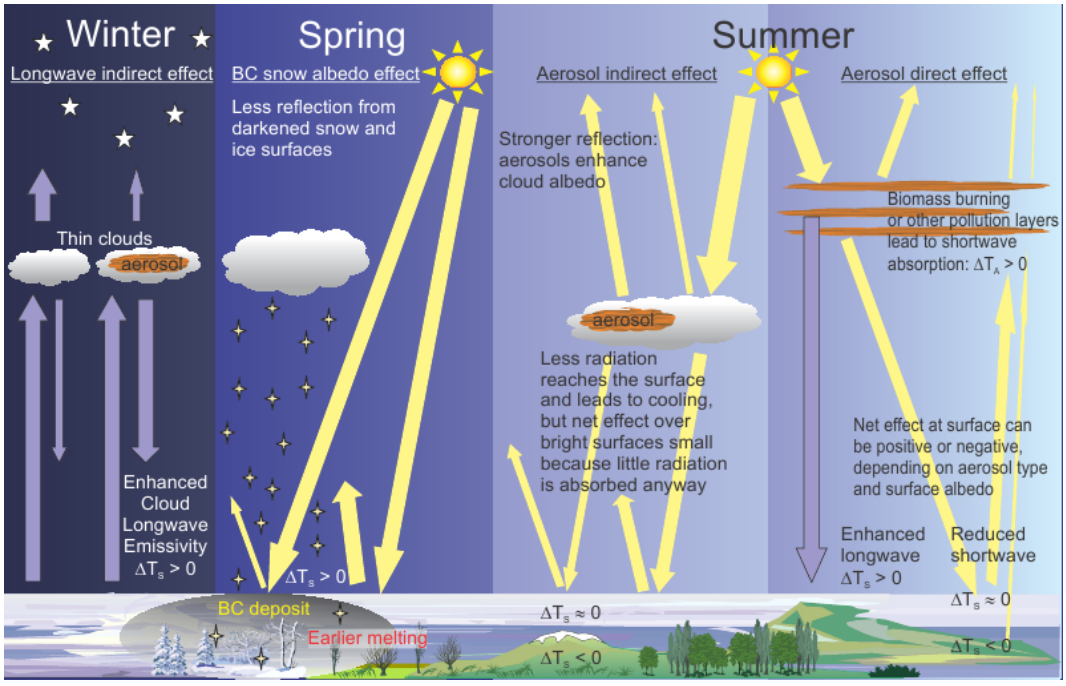

Figure 2.10: The forcing mechanisms in the Arctic as a result of pole ward transport of middle latitude gasses and particulate pollutants. The wintertime is represented in the left, spring in the middle and the summertime to the right. ΔT indicates the surface temperature response [Quinn et al., 2011, 2008].

Direct effects

The direct effects of Arctic aerosols layer on the radiation balance is due to the absorption and scattering of radiation by aerosols. The absorption and scattering depends on the particles composition, which is affected by the particles source and transport path wave.
In the summer time an absorbing aerosol over a highly reflective surface will result in a warming at altitudes above and within the polluted layer and instantaneously reduce the amount of solar energy received at the surface. This leads in general to a cooling ($\Delta T_s < 0$), but the net effect over a snow or ice covered surface is small, because a limited amount of radiation is absorbed anyway ($\Delta T_s \approx 0$). However, the added atmospheric heating, generated by the absorbing Arctic aerosol layer, will subsequently increase the downward long-wave radiation to the surface and warm the surface ($\Delta T_s > 0$) [Quinn et al., 2008]. Thus, the estimated cooling of the surface due to absorption of solar radiation by the aerosol layer is compensated by long-wave emission from the atmosphere to the surface, therefore the net effect at the surface is either positive or negative and largely determined by the properties of the aerosol and the underlying surface layer.

In the Arctic winter the longwave radiation dominates and thereby controls the energy budget. Furthermore, the aerosol concentrations is in general high this time of year. This is a combination of long range transported aerosols and weak removal processes, because of a strong surface based temperature inversion which inhibits

turbulent transfer. In such conditions it leads to growth of hygroscopic aerosols into cloud droplets or ice crystals, which will enhance the long-wave radiation ($\Delta T_s > 0$).

Indirect effects

An increase in the number of aerosol particle pollutants that act as CCN will affect Arctic stratus and stratus cumulus by increasing the cloud droplet number concentration. This will in the summer time result in an increase in radiation being reflected back to space (Figure 2.10). However, in winter a large amount of long-wave radiation will be re-emitted due to the clouds being efficient at trapping and re-emitting (Figure 2.10).

The indirect effect is assumed to be the most significant effect due to Arctic haze [Quinn et al., 2008]. A decrease in droplet effective radius in these optically thin clouds will increase the infrared optical depth and thus the infrared emission. The final result is expected to be an increase in the re-emitted longwave radiation from the cloud. In addition, the decreasing in cloud drop size distribution has additional effects. It will lead to a decrease in precipitation and therefore also increase the lifetime of the cloud, which to some extent will increase the cloud emissivity [Quinn et al., 2008].

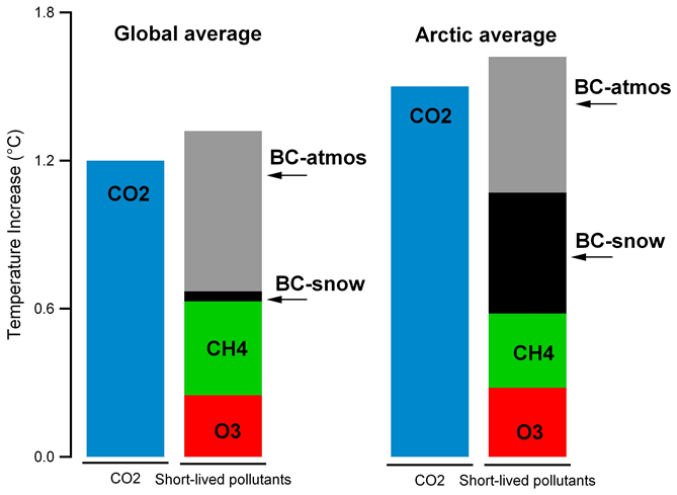

Figure 2.11: The best estimate of climate forcing from short lived forcers. It shows annual mean temperature increase caused by CO_2 and short-lived pollutants compared to the industrialization. The global values are based on [Intergovernmental Panel on Climate Change (IPCC), 2007a] and the Arctic value is based on [Quinn et al., 2008].

Surface albedo

Aerosol particles such as black carbon contribute to another forcing mechanism, which is related to the deposition of black carbon particles on snow and ice covered surfaces (Spring Figure 2.10). Absorbing particles deposited onto the surface via

wet or dry deposition affect the surface radiation budget by enhancing absorption of solar radiation at the ground and thereby reduce the surface albedo. Such absorption of solar radiation at the surface can warm the lower atmosphere ($\Delta T_s > 0$). The Arctic winter atmosphere is very stable and therefore a rapid heat exchange with the upper troposphere is prevented.

In figure 2.11 the contribution of short-lived pollutants in warming in the Arctic and on a global scale shown. The black carbon particles deposited on a snow- or ice-covered surface in the Arctic has a much greater warming potential compared to the global estimate. The BC particles found in the atmosphere in the Arctic and globally are here estimated to have almost equal warming potential.
The radiative impact from the Arctic aerosol layer is complex. It depends on feedback between particles, clouds, radiation, surface cover, and vertical and horizontal heat exchange, that complicate and determine the total effects of direct-, indirect-forcing and thereby the amount of warming in the Arctic.

2.5 Spectral properties of atmospheric aerosols

In order to determine the aerosol particles radiative effects the ratio of scattering to extinction (absorption plus scattering) has to be known. The aerosol particles ability to scatter or absorb depend on the chemical composition of the particles. The theory behind the scattering and absorption of radiation by aerosols is based on linearity between aerosol particles and:

- the intensity of the radiation
- the local concentration that is responsible for the absorption and scattering
- the effectiveness of the absorbers or scatterers, equation 4.1.

The full theory is described in section 4.3.2 and according to the theory the aerosol particles are assumed to be spherical. Nevertheless, it is important to know the effects of spherical particles of radius r for which the scattering and absorption efficiency can be prescribed as a function of the *size parameter* x:

$$x = \frac{2\pi r}{\lambda}$$

here λ denotes the wavelength of the light. In the *Rayleigh scattering* regime the expression for the scattering efficiency K_λ is defined as:

$$K_\lambda \propto \lambda^{-4} \tag{2.6}$$

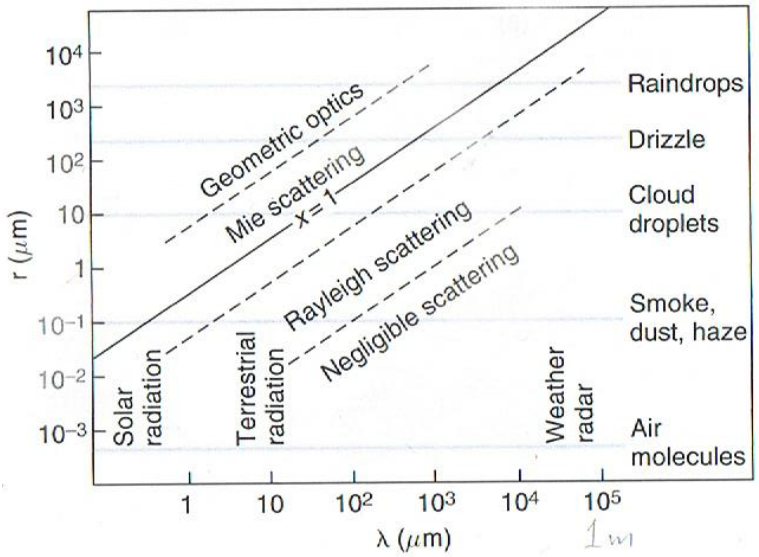

Figure 2.12: Size parameter x as a function of wavelength (λ) of the incident radiation and particle radius r [Wallace and Hobbs, 2006].

Figure 2.12 show the range of size parameters for various kinds of particles and radiation by various wavelength (λ). For scattering of radiation in the visible part of the spectrum, x ranges from much less than 1 for air-molecules to $\approx$ 1 for haze and smoke particles to $\gg$ 1 for raindrops [Wallace and Hobbs, 2006]. Thus, not only the composition of the aerosol particles affect the particles ability to absorb or scatter light, but also the wavelength of the incoming light plays a major role.

2.6 Chemical compounds within the Arctic

In the Arctic troposphere emission from both anthropogenic activity and natural sources are found. Emissions from anthropogenic activity are limited in the Arctic, because of the few industrial areas that exist in the Arctic region. Therefore are anthropogenic emitted gaseous and particulate pollutants highly associated with long-range transport from the mid-latitudes and high latitudes [Law and Stohl, 2007].

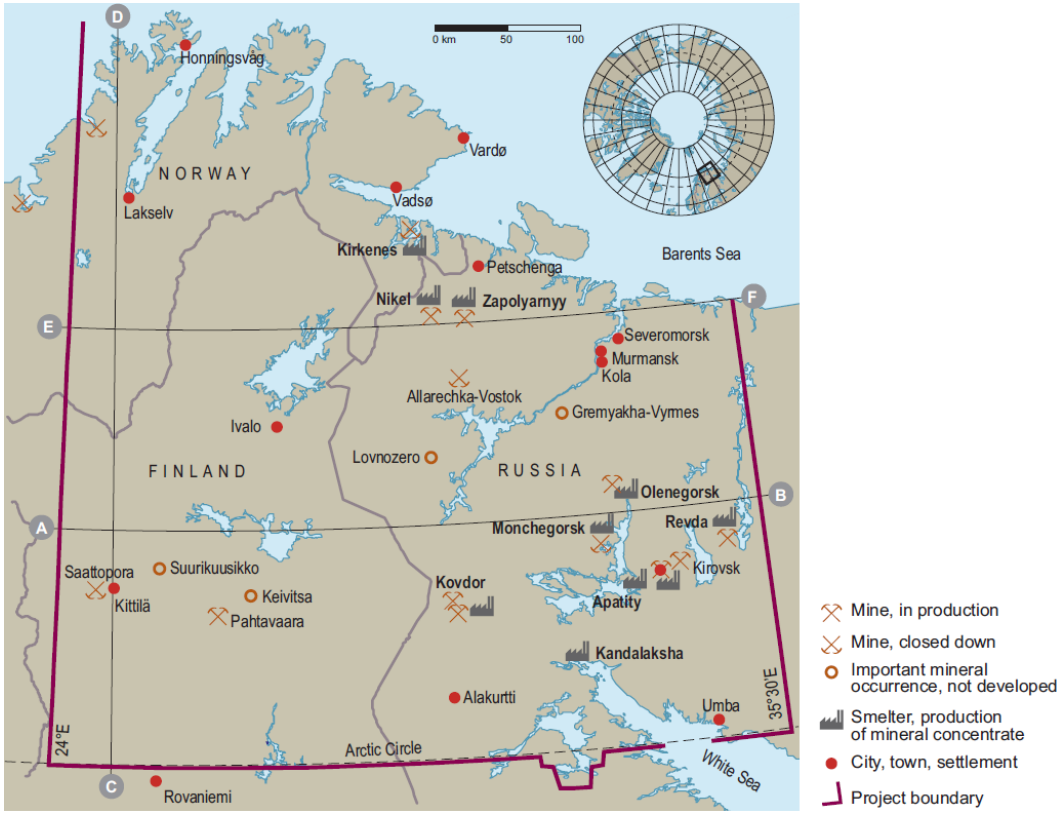

Figure 2.13: The major industrial activities in northern Russia due to processing of mineral concentrate and mining [AMAP 2006].

Emissions from the few industrial areas in the Arctic and sub-Arctic region is mainly from North Russia, Siberia [AMAP 2006]. Those emissions are associated with local pollution according to energy production and transport in and around the Arctic. The energy productions originate from oil, gas and coal-fire related activities which mainly are located in northern Russia. At least nine coal-fired power plants due to smelter and production of mineral concentrate are located at this side of the Arctic (Figure 2.13). In addition, one of the world's biggest production of nickel, as well as a major production of cupper (Cu), platinum (Pt) and palladium (Pd), is located above the Arctic circle in Russia at Norilsk (Figure 2.14). Here shipping traffic is one of the main transports to Murmansk, where processing facilities are located [Norilsk Nickel, 2011].

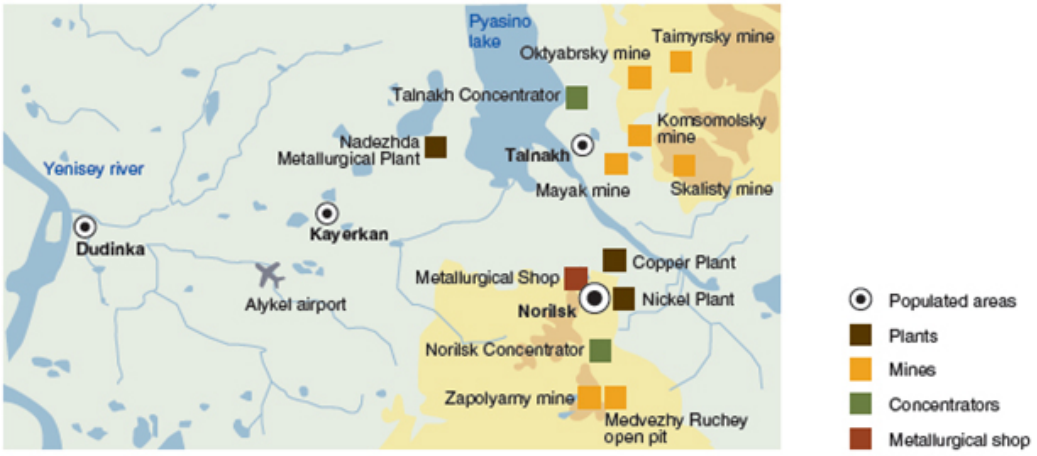

Figure 2.14: The mines and plants located in the area around Norilsk. Seven mines produce copper-nickel sulfide ores, where the ores mined have different contents of nickel, copper, platinum, gold and other components [Norilsk Nickel, 2011].

Emissions from shipping traffic contribute to local Arctic pollution. In general, the most extensive shipping activities in the Arctic Ocean take place on the Russian side, where the Northern Sea Route (NSR) carries the largest volume of traffic of any Arctic seaway [AMAP 2006]. The NSR is open for shipping traffic between two and half months a year, which limits the contribution to Arctic air-pollution from shipping traffic to thses months.
The shipping traffic in Arctic Monitoring and Assesment Programme (AMAP) Working Group 2006 is projected to increase over the next 10 to 15 years, where the main part is due to transport of oil from northern Russia to markets in Europe and Asia [AMAP 2006]. Besides that, the shipping traffic in the Northwest Passage and Beaufort Sea is also expected to increase, due to decreased ice-extent, which can enhance the emission from shipping traffic at this side of the Arctic.

2.6.1 Metal and combustion elements in the Arctic

Heavy metals, such as mercury (Hg), lead (Pb), zinc (Zn), copper (Cu) and nickel (Ni) are emitted from anthropogenic sources (metal industrial activity) into the Arctic atmosphere [Heidam et al., 1999]. These metals are soluble in water and bound to different solids, but they cannot degrade. Therefore are they redistributed into the environment from natural and anthropogenic processes. The main causes of anthropogenic metallic pollution in the Arctic are caused by extraction, used and disposal of metals, but they are also naturally released from rock degradation and volcanic activity [Johansen et al., 2007].
Mercury is mainly found as inorganic mercury in the atmosphere and has a residence time of one year, which allows it to be globally transported and reach the Arctic region [Goodsite et al., 2004; Skov et al., 2004]. This is quite a long residence time compared to non-volatile metals, such as lead, which has a residence time of about one week.
Most of the sources for heavy metals derive from sources outside the Arctic region

and the largest contributor to mercury emissions in 2005 were China [AMAP 2011]. In addition, Mercury has the last two decades been decreasing, but in general Mercury have been enhanced over the past roughly 150 years [AMAP 2011]. This increase has occurred despite a reduction in source regions such as North American emissions and northern Europe. This is highly associated with change in source region, where the last decades current trends in heavy metals perhaps can be assigned to sources in East Asia.
Another prominent anthropogenic source in the Arctic is associated with combustion processes. Elements associated with this sources is iron (Fe), Manganese (Mn), Gallium (Ga), Vanadium (V), Arsenic (As), Lead (Pb) as well as Black carbon and Sulphate [Heidam et al., 2004; Quinn et al., 2011]. In addition, the ratio between the elemental and organic carbon depend on the combustion processes. In general, diesel or fuel engines are emitting more elemental than organic carbon, which result in a high EC to OC ratio. Biomass burning, in general, emit more OC than EC and result in a low EC to OC ratio. Besides that, OC has a significant variation in volatility and therefore can OC be present both in the gas and particulate phases. The presence of OC in the gas phases into the atmosphere can lead to chemical transformation to *secondary organic aerosols* (SOA).

2.6.2 Natural compounds in the Arctic

Natural emission divides from different local sources within the Arctic, but also long-range transport from outside the Arctic region. Natural emission covers a variety of different sources from the frequency of volcanic eruption to aerosols created by sea spray. Different chemical elements can be associated with different natural sources.
Elements such as *aluminium* (Al), *Silicium* (Si), *Titanium* (Ti) and *iron* (Fe) are typically associated with crustal elements emitted to the atmosphere as windblown soil and dust particles [Heidam et al., 1999]. However, elements such as *Calcium* (Ca), *Potassium* (K) and *Strontium* (Sr) are associated with marine sources. They are present in seawater and are released to the atmosphere by sea spray and transformed into aerosols [Heidam et al., 2004]. Natural emission from combustion processes is highly associated with forest fires and general biomass burning, which contributes to elements such as black carbon, sulphate and *volatile organic compounds* (VOCs). Biogenic VOCs, such as isoprene and terpenes are respectively associated with photosynthetic activity of plants and in the leaf oils of plants [Kourtchev et al., 2006; Seinfeld and Pandis, 2006]. Those elements are photo-oxidized in the atmosphere to non-volatile species and transformed into SOA [Kourtchev et al., 2006, 2008].

Chapter 3

The Arctic atmosphere and climate

This chapter introduce the Arctic climate and its multiple interactions with the global climate system. The first section is mainly concerning the characteristics for the Arctic troposphere, which deviate from mid and low latitudes. The second section focuses on the cryosphere, where the behaviour of the sea ice extent and the ocean current within the Arctic is considered. The following section is concerning the Arctic climate sensitivity. The fourth section describes the general circulation pattern in the Northern Hemisphere whit special attention added to the different modes of Northern hemispheric indices, the *North Atlantic Oscillation* (NAO) and the *Pacific - North American Oscillation* (P-NAO). This section is also discussing the *Arctic Oscillation* (AO) and the related *Polar Vortex* (PV), which is predominating the Arctic winter atmosphere. The final section is regarding the general transport pathway to the Arctic.

3.1 The Arctic atmosphere

The atmospheric motion is generated by the inhomogeneous radiative energy received at the Earth surface *(Insolation)*. The insolation for different months is illustrated in figure 3.1, where 90°N is representing the Arctic region.

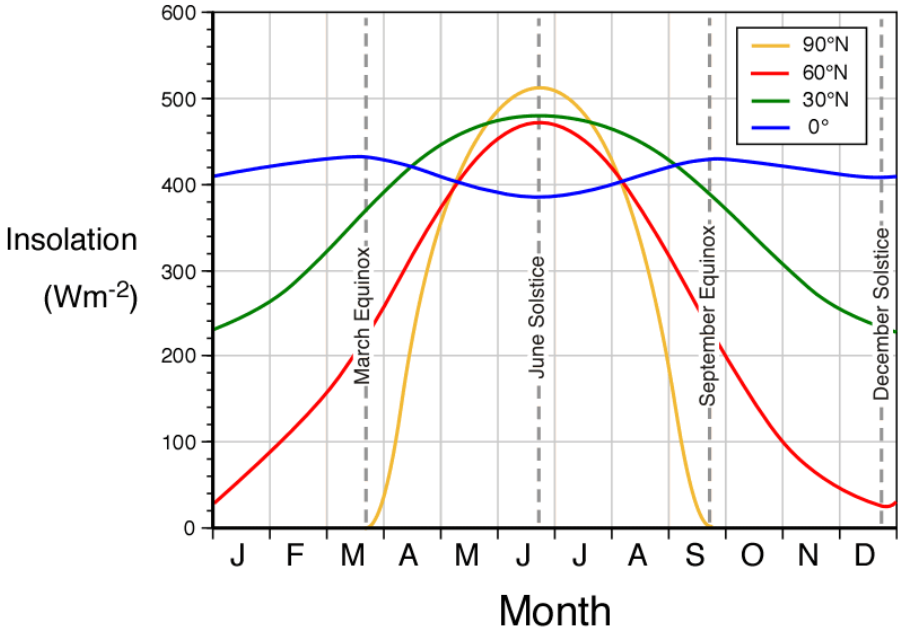

Figure 3.1: Insolation [$\mathrm{W\,m^{-2}}$] for different latitude, where 90°N represent the Arctic. A high variability in the insolation is dominating the Arctic region. [PhysicalGeography.net, 2011].

The long period of daylight in the Arctic summer result in a high radiation received at the surface, compare to winter where a low amount to non-existent radiation is received at the surface. This is also reflected in the seasonal mean temperature. The mean winter temperature falls well below $-20\,$°C and together with longwave radiation loss it result in perfect conditions for temperature inversion, which dominates the Arctic winter atmosphere.

Inversion is an atmospheric situation where the temperature increases with altitude rather than the normal pattern of temperature decrease. In figure 3.2 a typical characteristic inversion is shown in a skew-T Log-P diagram from a weather balloon placed at Point Barrow in Alaska [Rasmussen and Turner, 2003].
A *skew T Log-P diagram* is also known as a thermodynamic diagram which is a graphic representation of pressure, density, temperature, and moisture in a way that the basic atmospheric energy transformations are visually depicted. This diagram presents a vertical picture of the atmospheric conditions and make it possible to identify various air masses, the stability of a layer, identify clouds or understand the processes occurring.

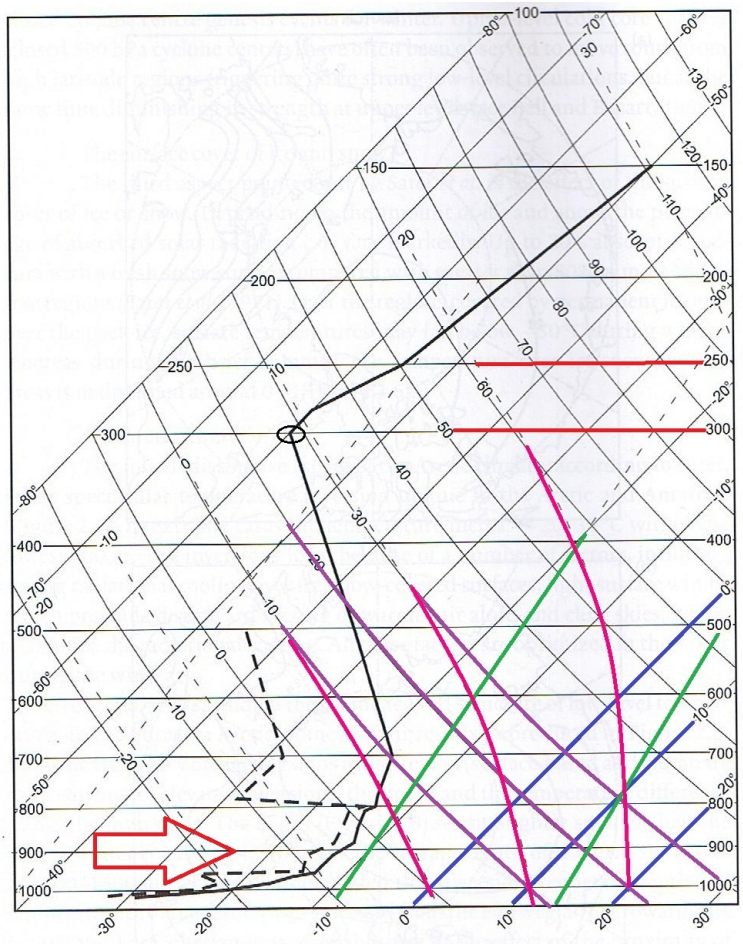

Figure 3.2: A typical skew-T Log-P diagram which shows an inversion in the Arctic. Here, the black dashed line is the dewpoint temperature, the black line the temperature, the red arrow indicates the *inversion layer* found from the surface to about 800 mb, the red line denotes the isobars (Lines of constant pressure), the blue line denotes isoterms (Lines of constant temperature), the green line denotes the mixing ratio, the purple line denotes dry adiabates, the pink line denotes the moist adibates and the black circle denotes where the tropospause is found [Rasmussen and Turner, 2003].

An example of a skew T Log-P digram is shown in figure 3.2 where the black dashed line is the dewpoint temperature and the black line is the temperature. Here, the *inversion layer* (marked with a red arrow in figure 3.2) is found from the surface to about 800 mb. The inversion layer give rise to a very stable stratification in the lower troposphere, that reduce turbulent exchange and hence deposition of aerosol particles. Turbulence can be enhance over open water, but this is not very likely in the Arctic winter, because of the present of sea ice.

The most common types of inversions are advective and radiation inversions. An advective inversion is formed when warm air moves over a colder surface and a radiative inversion is formed when the surface has become cooler by loss of heat by radiation. The ground cools more rapidly that the ambient air, because the

ground is a much better emitter of longwave radiation that the air. In general, the Arctic winter is dominated of strong radiation cooling over the ice or snow covered surface, which leads to formation of air masses which are specific for the region as illustrated in figure 3.3. Arctic air masses are extremely dry which also minimize the wet deposition and lead to a long lifetime of aerosol particles in the Arctic winter troposphere.

Figure 3.3: Air-masses in the winter, where *m* denotes maritime air masses (more moist) and *c* denotes continental air masses (more dry). A, P and T denotes Arctic, Polar and Tropical, respectively [Rasmussen and Turner, 2003].

The age of the Arctic air masses[1] is shown in figure 3.4. The figure represent the average Arctic age of air from the surface to 100 m above, for January (Figure 3.4a) and July (Figure 3.4b). The figures are from a model study by Stohl [2006]. In January the most aged air masses are found over North American compare to the least aged air, which resides north of Eurasia. This is consistent with the average wind pattern [Stohl, 2006]. In July, the distribution of aged air is more symmetric located above the Arctic Ocean and the Atlantic sector has a less aged air mass, which indicated a major entry route to the Arctic in summer. In addition, during both months the air above the high topography of Greenland is the least aged, which reflect the high wind speed, but also strong meridional motion west of Greenland due to the frequent northward-traveling cyclones over Baffin Bay [Stohl, 2006].

[1]The age of air masses can also be seen as a measure for the isolation of air masses

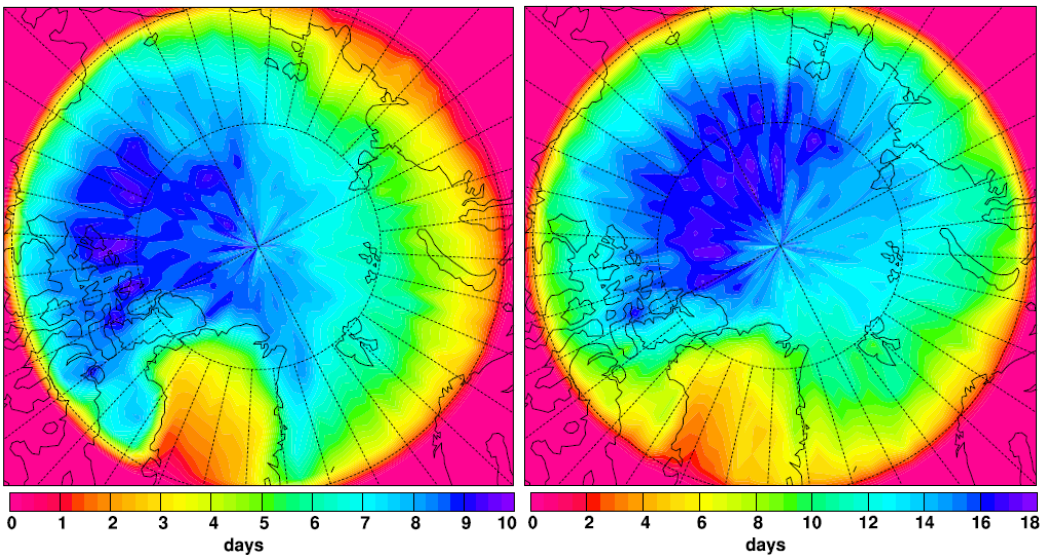

(a) January **(b)** July

Figure 3.4: a) January and b) July mean Arctic age of air in the lowest 100 m of the atmosphere [Stohl, 2006]. Here the mean Arctic age of the air masses at Station Nord is found about 7 days in winter.

3.2 The Arctic Ocean

The Arctic Ocean forms the core of the marine Arctic. It is characterized by two basins, the Eurasian and Canada that is more than 4000 m deep and almost completely land locked as shown in figure 3.5.
The open boundary of the Arctic Ocean is illustrated in figure 3.5 and those are found; along the Barents Shelf edge from Norway to Svalbard, across the Fram Strait; down the western margin of the Canadian Archipelago and finally across the Bering Strait. This open boundary is the exchange area between the Arctic Ocean and the Atlantic and Pacific Ocean, which can transport warm and salt water from the mid-latitudes into the Arctic region. This has the potential to influence the Arctic Ocean as well as the atmospheric exchange. Warm water inflows can melt sea ice and result in mixing processes, which move heat to the surface. The mixing is dominant for the vertical gradient of salinity and temperatures [ACIA 2004].

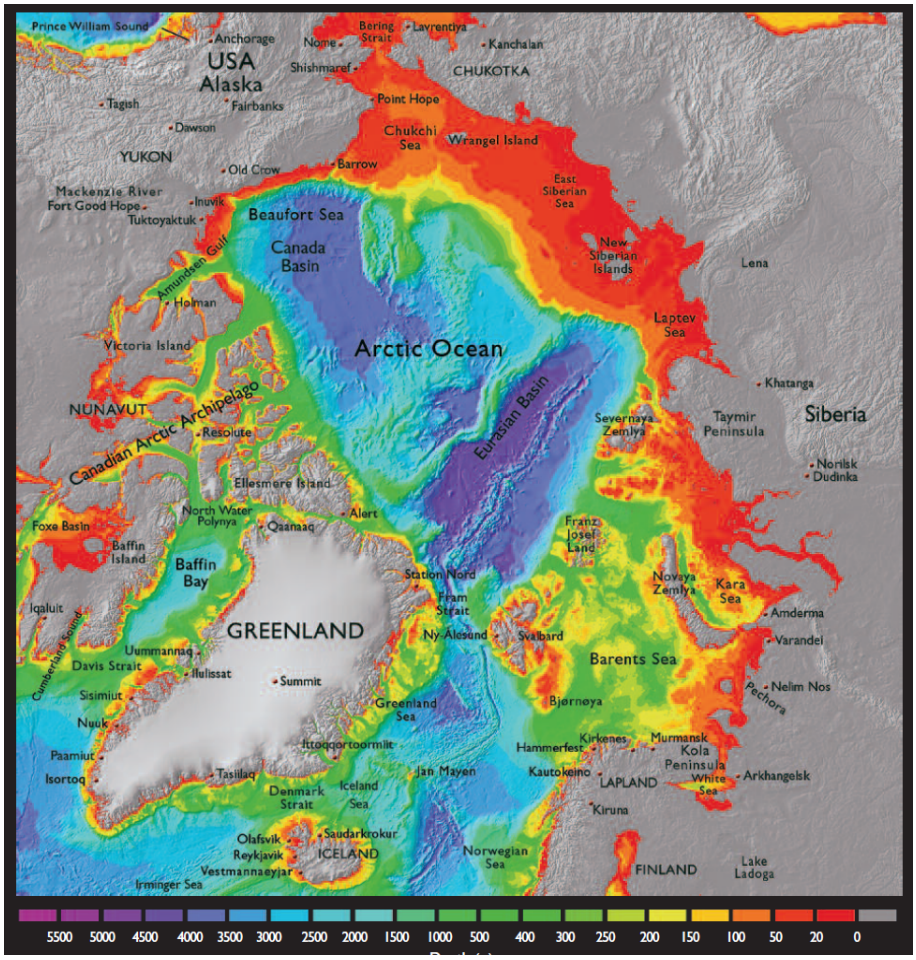

Figure 3.5: A map of the Arctic region, where it is illustrated that the Arctic region is dominated by two basins, the *Eurasian basins* and *Canda basins* [ACIA 2004].

The currents system of the Arctic Ocean is shown in figure 3.6, where the Norwegian Atlantic Current and the West Greenland Current are northbound streams. Those are carrying warm saline water into the Arctic Ocean, but limit the flow of low-salinity water towards the Atlantic. The Norwegian Atlantic Current branches into the West Spizbergen Current and the Barents Sea flow and as it passes through the Fram Strait it has obtained a temperature near 3 °C. Afterwards it follows the continental slope eastward at a depth of 200 m to 800 m. When the current enters the Arctic Ocean at depths of 800 m to 1500 m in the eastern Barents Sea, it has cooled to less than 0 °C.

The West Greenland Current carries 3 °C seawater to the northern Baffin Bay, where it mixes with outflow from the Arctic Ocean and joins the south-flowing Baffin Current [ACIA 2004].

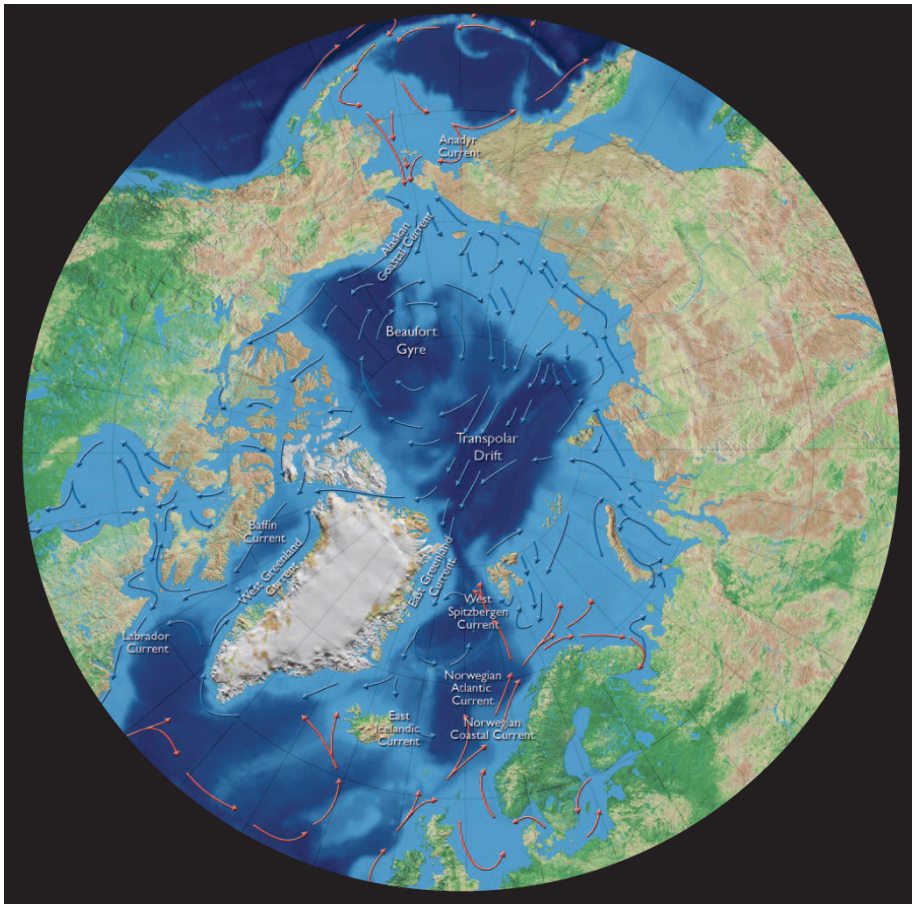

Figure 3.6: The current system of the Arctic Ocean [ACIA 2004].

The Anadyr Current inflow from the North Pacific is less saline and circulates at a shallow depth (depth less than 100 meters) compared to the Atlantic inflow. This inflow from the Bering Strait dominates the upper ocean of the western Arctic (the Chukchi and Beaufort Seas, Canada Basin and the Canadian Archipelago) and influences the thickness of sea ice. The Anadyr current is less saline, which is highly reflected in the presence of sea ice [ACIA 2004].

3.2.1 Ice coverage

The Arctic Ocean is dominated by a large amount of sea ice which can be divided into *first-year* and *multi-year ice*. First-year ice is in its first winter of growth or first summer of melt. Its thickness are a few tenths of meter to 2.5 meters. Some first-year ice survives the summer and then becomes multi-year ice. This ice becomes harder and almost salt free over several years. The average thickness of sea ice in the Arctic Ocean is about 3 m and the thickest ice (ca. 6 m) is found along the shores of Northern Canada and Greenland [ACIA 2004].
The ice extent[2] in the Arctic Ocean is affected by the surface current and by the wind, especially first-year ice flows easily under the forces generated by storm winds.

[2]Ice extent is defined as the area of the ocean with a fractional ice cover of at least 15% [Serreze et al., 2007].

In the Arctic Ocean there are two major ice circulation systems; the east to west *Transpolar Drift* in the Eurasian basins; the clockwise *Beaufort Gyre* in the Canada basins, where both of them are illustrated in figure 3.6. The Beaufort Gyre turns the Polar Ice Cap along with it and the Transpolar Drift carries water and ice from Siberia across the Pole and down to the east coast of Greenland. Here it mixes with the East Greenland current which is caused by the inflow from Siberian rivers and a westerly wind, that push Arctic surfaces water eastward into the Atlantic [Dydkjær et al., 2008; Serreze et al., 2007].

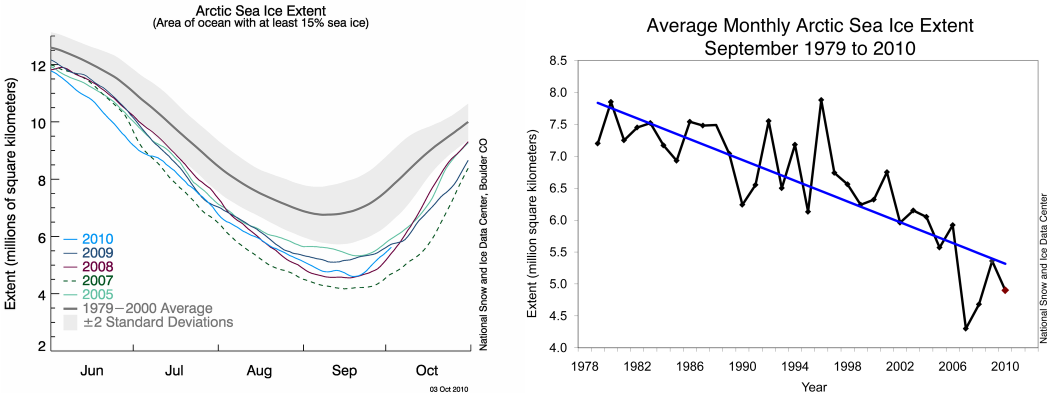

(a) Summer Sea Ice extent **(b)** Sea Ice Extent September

Figure 3.7: a) Arctic summer sea ice extent for the last few years which is found at the same range. Here, the solid blue line denotes data from 2010 and the solid gray indicates the average extent from 1979 to 2000. b) Average monthly Arctic sea ice extent in September from 1979 to 2010, which show a continual decline [NSIDC 2011a].

The Arctic sea ice extent follows an annual cycle of melting and refreezing due to the change in seasons (Figure 3.7a). It has a maximum extent in March and a minimum extent in the end of the summer melt season (September). Arctic sea ice extent vary from year to year as shown in figure 3.7b. While September ice extent has declined at a rate of 11.5 % per decade (relative to the 1979 to 2000 average) and about 3 % per decade in the winter months (Figure 3.7b) [NSIDC 2011a]. In the melt season of 2007, the Arctic sea ice extent was at the lowest level ever since satellite measurements began in 1979. This minimum resulted in an opening of the Northwest Passage, which is the first time ever recorded. In general, not only the sea ice extent decline also the amount of old thick ice continues to disappear. While in 2010 there was an increase in second and third year ice, but the oldest ice (more than five year) had almost disappeared in the Arctic. In September 2010 less than $60\,000\,\text{km}^2$ five-year old ice remaine in the Arctic Ocean compared to $2\,000\,000\,\text{km}^2$ old ice remained at the end of the summer in 1980s [NSIDC 2011b].

3.3 Arctic Climate sensitivity

In the Arctic the temperature has been increasing almost twice as much as the global average over the past 100 years [Summary IPCC 2007]. The average annual

temperature have been risen by 2 °C to 3 °C since the 1950s and in winter by up to 4 °C, but the overall warming in the recent decades are addressed to the regions within the Arctic [ACIA 2004]. The warming has been largest over the land areas, but there are also regions in southern Greenland, which have experience a cooling. The warming has been accompanied with an earlier and also longer melt season which results in melting of glaciers and a reduction in sea ice extent which is one of the most important factors for global climate changes. The Arctic environment and vegetation are already showing signals of significant and rapid response to these changes. For example, the tree coverage expands and due to the earlier snowmelt on land an early plant primary production takes place [AMAP Conference].
There is no longer any doubt that the Arctic is warming and the warming will not only affect the Arctic region but also impact the planet as a whole [ACIA 2004]. A melting of Arctic glaciers and sea ice contributes to global sea-level rise and weakens the thermohaline circulation. Some indications by Overland and Wang 2010 suggesting that the low sea ice extent in the Arctic Ocean also increase modification of atmospheric circulation patterns over parts of the Northern Hemisphere.

3.4 The Northern Hemisphere annular indices

The Arctic atmospheric circulation pattern is highly influenced by the overall Northern Hemispheric circulation, which variability can be descried with the modes of the *North Atlantic Oscillation* (NAO), the *Pacific - North American Oscillation* (P-NAO) and the *Arctic Oscillation* (AO).

The *North Atlantic Oscillation* (NAO) mode is a measure of the prevailing flow pattern near the surface in the North Atlantic area. The mode is based on *sea level pressure (SLP)* - anomalies of opposite sign over the Azores and Iceland; a flow pattern, where both the Icelandic low-pressure and the Azores high-pressure are more intense than usual, have a positive NAO index; a flow pattern, where both pressure systems are weaker than normal, has a negative NAO index.
During the *positive NAO mode* a stronger pressure gradient between the Icelandic low-pressure and the Azores high pressure will occur and control the strength and direction of the prevailing westerly winds (westerlies) and storm tracks across the North Atlantic as shown in figure 3.8.

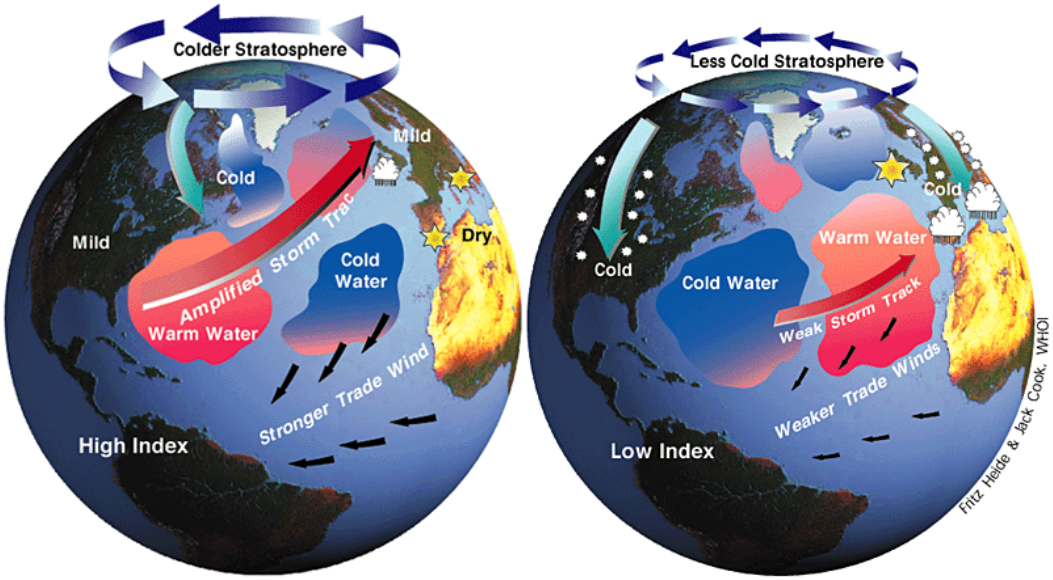

(a) Positive mode **(b)** Negative mode

Figure 3.8: The two modes of the *North Atlantic Oscillation* (NAO). a) The positive mode where a high pressure is found over the Azores and a intense low is found over Iceland. b) The negative mode with opposite behaviour. (Illustration by Fritz Heide & Jack Cook, Woods Hole Oceanographic Institution)

During the positive NAO mode the westerlies are shifting toward a more meridional orientation (southwest - northeast) and are found further to the north. The wind transport into the Arctic from all three Northern continents (Europe, North America and Asia) is enhance generally during this mode and result in high pollution levels [Stohl, 2006]. However, in the positive NAO mode the middle latitude jet stream is more northern, which is related to wet and warm winter climate in Scandinavia, while cool and dry conditions predominate in southern Europe. The Arctic region (Greenland, Newfoundland and North Canada) are in general experiences colder conditions. In the *negative NAO mode* a weak pressure gradient occur between the Azore high-pressure and Iceland low-pressure, which generated weaker westerlies there lie further to the south with a more zonal air flow. In general, for this mode the Arctic region does not experience the same cold conditions. Normally the Southern Greenland has warmer and wetter conditions than normal, while Scandinavia has colder weather conditions.

The influence from the NAO mode does not extend to the Pacific site of the Arctic. North America and Eurasia are more affected of the face of *El Nino/La Nina-Southern Oscillation* (ENSO), which are reflected in the mode of *the Pacific- North American teleconnection pattern* (P-NOA). In general, the positive P-NAO mode is associated with Pacific warm episodes (El Nino) and the negative P-NAO mode is associated with Pacific cold episodes (La Nina).

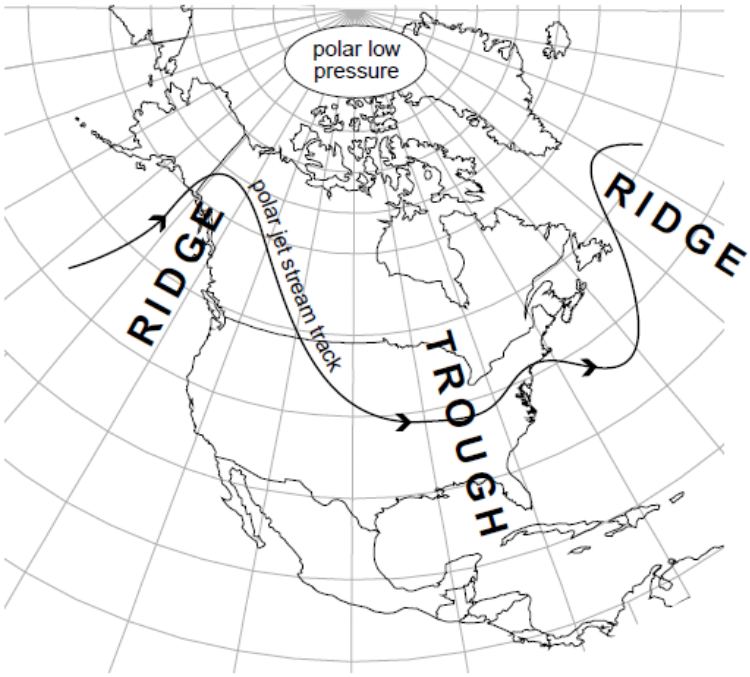

Figure 3.9: The positive *Pacific-North American oscillations* (P-NAO) pattern. Here the ridge is found over the western U.S. and the trough over eastern U.S. [Schmidt, 2003].

The P-NAO mode describe the anomalies in the geopotential 500 mb height fields over the western and eastern U.S. (Figure 3.9). *The positive mode* consist of high geopotential height fields over the western U.S. and low geopotential height fields over the eastern U.S., which are correlating with a ridging over the western U.S. and a deep troughing over the eastern U.S. This result in a height field pattern that forces cold air residing in Canada to move in south-east-direction, which gives low temperatures over the eastern U.S. and high temperatures over the western U.S.
The *negative P-NAO mode* consist of low geopotential heights over the western U.S. and high geopotential heights over the eastern U.S. This result in a deep troughing over the western U.S., which allow cold air from western Canada to move to southern directions. Over eastern Canada it lead to warm moist air masses from the Gulf of Mexico and the Atlantic Ocean to travel northward and results in higher temperatures and more humid conditions [AASC].

3.4.1 The Arctic oscillation and the Polar Vortex

The NAO mode is highly related to the *Arctic Oscillation* (AO) mode (Figure 3.10). The AO mode is characterized by non-seasonal surface atmospheric pressure patterns in the polar region. It is defined as SLP-anomalies in the Arctic and SLP-anomalies of opposite sign centred around 37° to 45°N.
When the AO mode is positive, which mostly occur in winter, the surface pressure is low in the polar region and the upper-level circulation form an intense vortex. In this situation, the middle latitude jet stream blows strongly and consistently from west to east. The North-eastern Canada site of the Arctic do then experience

colder conditions than normal.
When the AO mode is negative there tend to be a high pressure in the polar region, which lead to a weak vortex. The wind is then more meridional and allow greater movement of cold polar air into the mid-latitudes, e.g. North America, Europe and Asia.

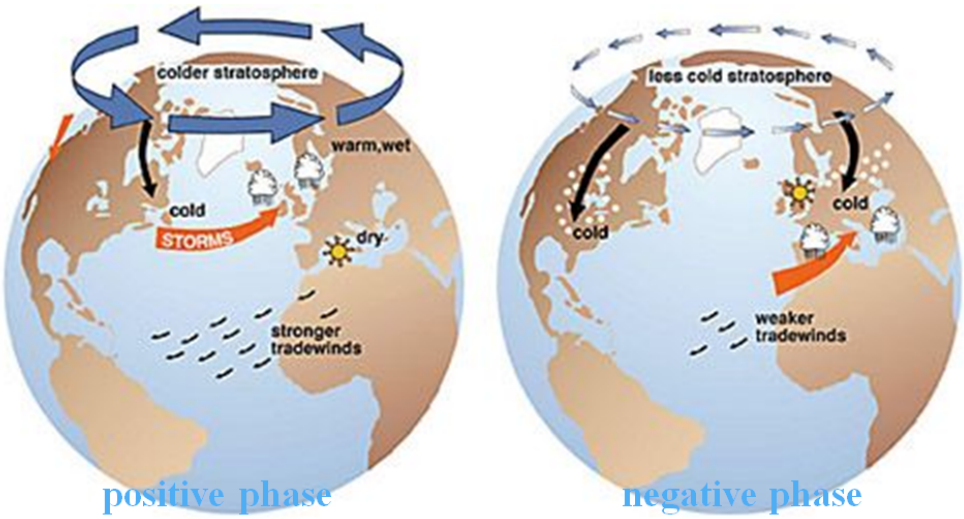

Figure 3.10: The *Arctic Oscillation* (AO), where a intense vortex is associated with the positive AO mode and a weak vortex with a negative AO mode (Image from NSIDC: artwork by J. Wallace, University of Washington).

The intense vortex formed under a positive AO-mode is a quasi-horizontal circulation in the stratosphere which is penetrating down to the lower troposphere in the Arctic region. It is known as the *Polar Vortex* (PV), but also called *polar cyclone* and *North Circumpolar Vortex*. It persists of counter-clock-wise circulating winds, which surround the North Pole and thereby trap the cold and dry Arctic air mass at high latitudes. These result in a cold and dense core over the pole (the centre of the PV) which form itself into a cyclonic vortex as illustrated in figure 3.11. The vortex is for some years quit persistent and can therefore be found close to the surface or seen at the 850 mb geopotential height-contours in Appendix A (Figure A.3d). It is often a permanent feature of the winter hemisphere, but in the summer a shallow vortex [Angell, 2006].

The strength of the PV is associated with the north-south temperature gradient, which appears to be strongest during the winter at mid-latitudes. Where the north-south temperature gradient is most pronounced the polar jet stream is present. The jet controls the large-scale synoptic cyclones and anticyclones in mid-latitudes and is associated with the formation and dissipation of these systems. This cyclones or anticyclones are nevertheless sometimes impacting the PV by wave activity from below (interaction of troposphere dynamics). This occurs when the wave activity is strong and the mean wave activity is directly poleward. The PV tends to break down or to split into smaller vortices, that allows warm mid-latitude air to reach polar latitudes. During winters, when the PV splits into two smaller vortices,

these can be found as troughs, which "normally" appear roughly over Baffin Island in Canada and over the North-east Siberia. During spring and summer the PV contracts and weakens to a single centre in the upper troposphere or in the stratosphere approximately over the pole. Furthermore, a more zonal air flow replaces the meridional air flow of the winter. In autumn, the Pole to Equator temperature gradient builds up again and then the vortex expands and strengthens and the air flow becomes more meridional.

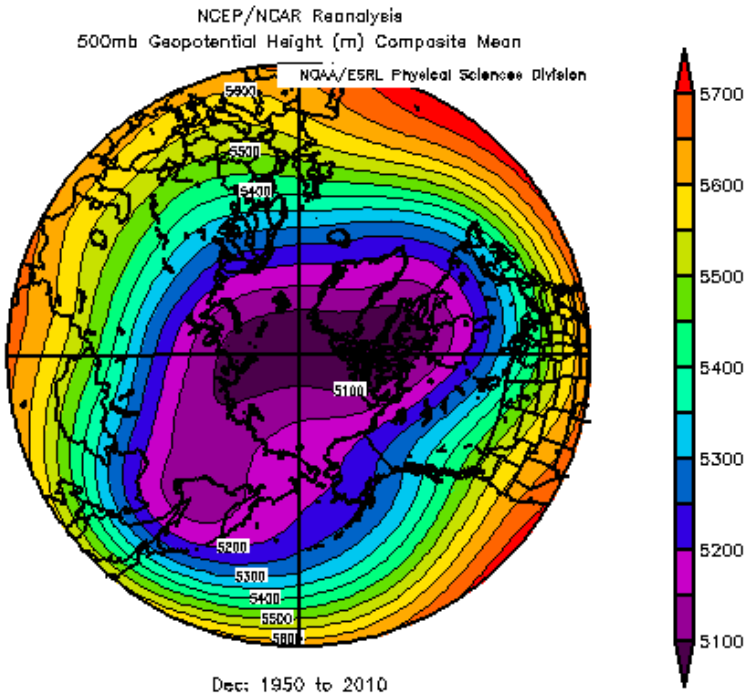

Figure 3.11: Arctic atmospheric pressure normal $500\,\mathrm{mb}$ geopotential height contours which were observed for December from 1950-2010. It is indicating the strength of a "normal" PV at the $500\,\mathrm{mb}$ geopotential height which trap the cold and dry Arctic air mass.

3.5 Transport pattern of BC to the Arctic

The schematic processes relevant for BC transport into the Arctic are illustrated in figure 3.12. Here the Polar Dome is an expression of surfaces with constant potential temperature over the Arctic, which has a minimum value in the Arctic boundary layer.
It has been realized by meteorologists that the polluted air masses from sources at a given location (*receptor site*) must have the same low potential temperature as the Arctic haze layer itself in order to be isentropic transported into the Arctic region on longer time scales [Stohl, 2006]. This applies that in the Arctic winter the polluted air masses from mid-latitudes or lower latitude are too warm and thereby leaves the high and sub mid latitude as the main source region. For winter situations where the boundaries of the Polar Dome (Arctic front) are located further to the south than normally, the polluted air masses influencing the Arctic become larger. In addition, it can be located as far south as 40°N in January/February.

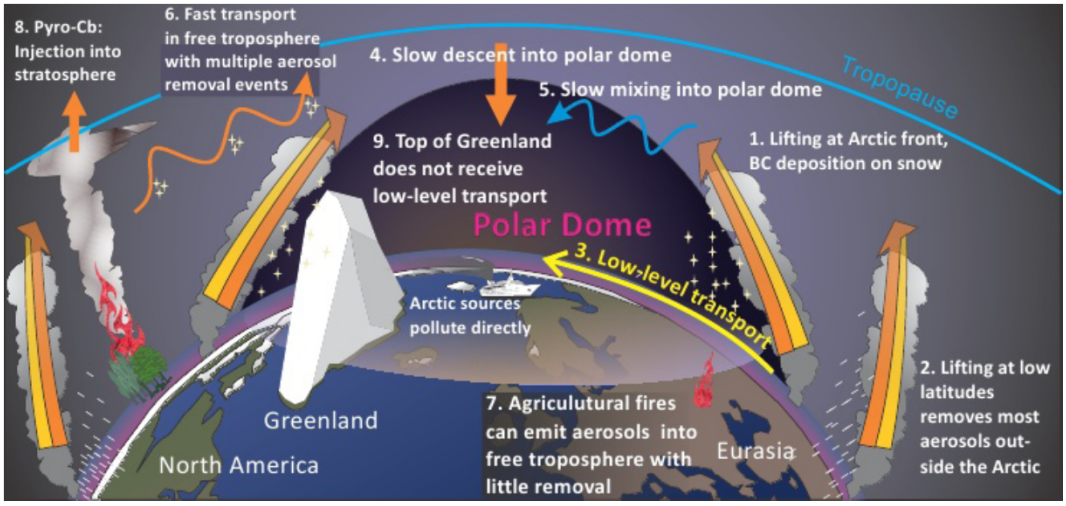

Figure 3.12: The schematic processes relevant for BC transport into the Arctic. Here the Polar Dome denotes surfaces with constant potential temperature [Quinn et al., 2011].

Polluted air masses from the south of the Polar Dome have potential to reach the Arctic region on short time scales, because on short time scales the potential temperature is approximately conserved. For this relatively warm polluted air masses south of the polar dome the isentropes transport into the Arctic middle or upper troposphere (above the dome) by pathways 1 and 2 in figure 3.12.
In general, polluted air masses can be transported into the Arctic region along three main pathways [Stohl, 2006]:

- *low-level transport* (LLT) followed by ascent in Arctic (Pathway 1)
- LLT alone (Pathway 3)
- uplift outside the Arctic, followed by descent in the Arctic (Pathway 2)

In addition, latent heat release by condensation of water vapour will further enhance the ascent. As a result, the lifting is typically associated with cloud formation and precipitation by which BC can be leaching out from the atmosphere and deposited at the surface with the precipitation [Quinn et al., 2011].

Emissions from north and mid Eurasia in winter and early spring has a higher probability to reach the lower Arctic troposphere by low level transport (Pathway 3). This receptor site is sufficiently colder in winter and together with the strong diabatic cooling of the polluted air masses in winter it helps to meet the requirement that the polluted air masses have the same potential temperature as the Arctic in order to be transported into the Arctic region.
BC emissions from the eastern North America and South-eastern Asia are almost only transported into the Arctic by pathway 1 and 2 in figure 3.12. If the lifting of those associated polluted air masses occur over the North Atlantic or North Pacific where storm track dominates, the BC aerosol will be deposited south of the Arctic region (Pathway 2) [Quinn et al., 2011]. Furthermore, receptor site located further north has a higher potential to contributed to deposition of BC on snow and ice covered surfaces, because the lifting occurs in relation with the Arctic front (Pathway 1).
In the Arctic the air masses are characterized by high stability as descried in section 3.1, which limits both vertical exchange between the boundary layer and the free troposphere. In addition, transport from the stratosphere to the lower troposphere is much slower in the Arctic compared to mid-latitudes. This is due to radiative cooling which is a much slower process (ca. $1\,\mathrm{K\,day^{-1}}$) and the associated descent from the upper troposphere will take several weeks as illustrated in figure 3.12 in pathways 4 and 5 [Quinn et al., 2011].

The BC haze layer is in general found high above the surface (free troposphere) rather than near the surface. This is due to the fact, that the Arctic troposphere is connected to the middle latitudes on synoptic time scales of a few days. The polluted air masses from those middle latitudes (Pathway 6) consists of a mixture of relatively clean background air as well as anthropogenic and biomass burning pollution plumes from various mid latitude source regions. The exact transport pathway of biomass burning plumes depends on the injection height of the plume. Fire-driven convection can inject aerosols into the free troposphere (Pathway 7), which reduce the efficiency of dry and wet deposition. Besides that, convection over boreal fires can be so strong that they penetrate the tropospause and thus, can inject aerosols directly into the stratosphere, where their residence time is particularly long (Pathway 8).

The transport pathways described above are mainly related to the Arctic winter situations where high pollution event are more common. This results in a seasonal transport pattern, reflected in the strengths of the Polar Vortex and the location of the Arctic front. In general, the Arctic front is locate much further to the south in winter with enhance the transport of pollutants to enter Arctic. In contrast, in summer the Polar Vortex is shallow and the Arctic front is located more to the north. This limits the low-level transport and, together with increased efficiency

of wet scavenging, it is the main reason for lower BC concentrations in summer compared to winter.

Chapter 4

Instrumental and modelling methods

In this chapter the field station Station Nord and the measuring instrument at the field station is described. In addition, the different sampling techniques and the theory behind these techniques are presented. The final section is concerning the model used for analysing the different element source apportionment.

4.1 Field station at Station Nord

The measurement site is located at Station Nord, which is a military station and airfield powered by the Danish military. The station is located at 20 m *above sea-level* (asl) at 81°36′N and 16°40′W and thus is an Arctic field station (Figure 4.1). Station Nord is found in the north-eastern Greenland, on Prinsesse Ingeborg Halvø (Princess Ingeborg Peninsula) in northern Kronprins Christian Land. This is in a distance of 933 km from the North Pole and place the station in one of the most desolate and impassable areas of the world. Here the fjords and inlets are frozen most of the time, but open water occur at irregular intervals. The climate is Arctic desert and the average temperature is about −15 °C, but in the short summer, the temperature can reach 14 °C, where the temperature in winter can reach −50 °C [Weatherbase, 2011].

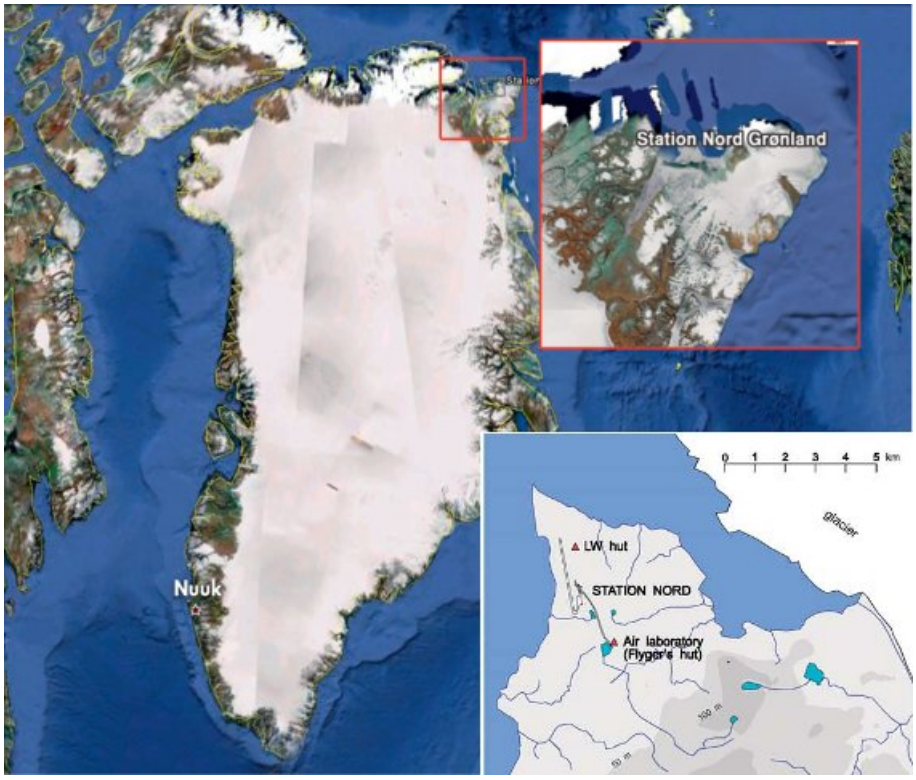

Figure 4.1: Map of Greenland and Kronprins Christian Land, where Station Nord is located close to ice cab Flade Isblink [Heidam et al., 2004].

The station was built for the U.S. in 1952 to 1953 for Greenland Telecommunications Administration by Danish contractors and paid by the Danish government [Nielsen and Hansen, 2011]. In 1989 the Danish atmospheric monitoring programe was initiated and carried out by the *Department of Atmospheric Environment* (ATMI) at the *National Environmental Research Institute* (NERI) and now the Department of Environmental Science, Aarhus University. The Danish monitoring programe at Station Nord has since 1994 been an official part of the *Arctic Monitoring and Assessment Programme* (AMAP).

The AMAP, has several monitoring stations distributed throughout the Arctic as shown in figure A.1, appendix A. The two measuring stations, which is found near Station Nord are Alert in Canada and Zeppelin on Svalbard, Norway. The measuring station of Alert is located on the north-eastern tip of Ellesmere Island, approximately 210 m asl at 82.5°N and 62.3°W. Here the surroundings are both land and ocean, which mainly are found with an ice or snow covering about 10 months of the year. The measuring station of Zeppelin is situated on a mountain ridge about 474 m asl, at 78°54′N and 11°53′E, on the western coast of Spitsbergen, Svalbard [Hirdman et al., 2010].

Table 4.1: The different instruments for measuring chemical compounds placed at Station Nord, their time resolution and their air flow sucked in though the instrument. Here PSAP denotes *Particle Soot Absorption Photometer*, POP's denotes *Persistent organic pollutants* and HVS denotes *High Volume Sampler*.

Chemical species	**Instrument**	**Time resolution**	**Air flow**
Black Carbon	PSAP	1 day	$20\,\mathrm{ml\,min^{-1}}$
Particle number size distribution	SMPS	1 hour	
POP, EC, OC, Levoglucosan	HVS	1 week	$500\,\mathrm{L\,min^{-1}}$
Heavy Metals (Al$\gg$)	Filter Pack Sampler	1 week	$40\,\mathrm{L\,min^{-1}}$
NO_3^-,SO_4^{2-},NH_4^+,SO_2	Filter Pack Sampler	1 week	$40\,\mathrm{L\,min^{-1}}$
GEM	Tekran	30min	
Ozone	Gas monitor	30min	
NO_x	Gas monitor	30min	
CO	Gas monitor	30min	

4.2 Measuring sites

Two cabins at Station Nord, Flygers Hut (Figure 4.2a) and the old DMI hut (Figure 4.2b), are used for monitoring and measuring long-range transported pollution.

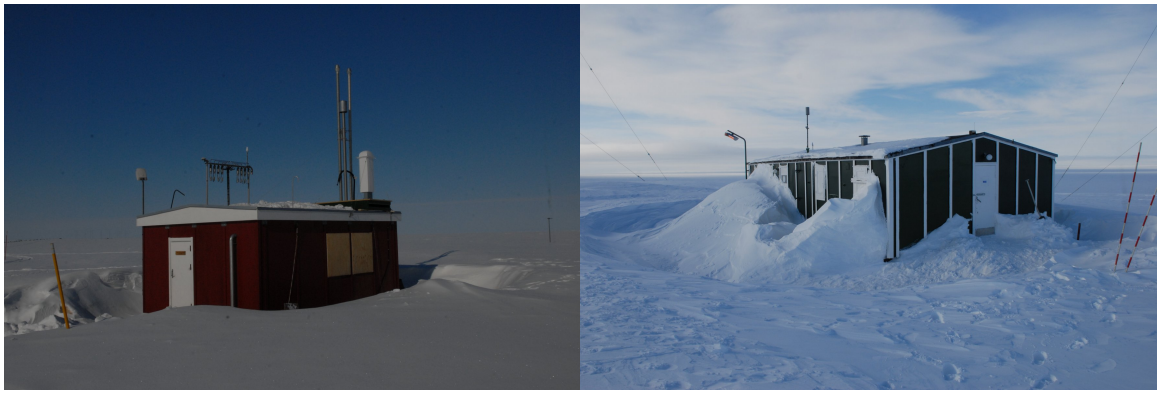

(a) Flygers hut **(b)** The old DMI hut

Figure 4.2: The two cabins at Station Nord equipped with inlets for measuring gasses and particles. In (a), on the roof the *Filter Pack Sampler* is seen and in (b) the inlet for the HVS is seen. (Photo:Bjarne Jensen, Institute of Environmental Science, Aarhus University.)

The old DMI hut is located inside the camp, where Flygers hut is located approximately 2.5 km south of the field station, in order to minimise the influences from local air pollution. The cabins are equipped with inlets for measuring gasses and particles (Listed in table 4.1) and supplied with electricity and heat from Station Nord's local diesel generator.

(a) The High Volume Sampler **(b)** Inside the HVS

Figure 4.3: (a) The *High Volume Sampler* (HVS) with a particle size classifier (PM_{10} head) above. (b) The HVS inside, where the filter is located between the two horizontal "sheets" and above the sequence of *Poly urethane foam* (PUF), the resign XAD and another PUF, which is found as a white cylinder at the bottom of the HVS and on the top of the HVS. (Photo:Bjarne Jensen, Institute of Environmental Science, Aarhus University.)

In the old DMI hut a *High Volume Sampler* (HVS) is operating (Figure 4.3a). It is a Digital High volume Sampler produced by Enviro Technology Services plc. It consisted of an inlet connected to a particle size classifier (PM_{10}[1] Head), which is seen on the top of the instrument in figure 4.3a. The system is connected to a pump to suck in the ambient air and generate an air flow where the particle size classifier separates particles larger than 10 µm in diameter from the air flow.
In figure 4.3b the HVS is shown inside. Here the sample filter is located between the two horizontal "sheets", and followed by a sequence of *Poly urethane foam* (PUF), a resign XAD and another PUF, which is found as a white cylinder at the bottom of the HVS. In addition, the PUF is used in order to measure *Persistent Organic Pollutants* (POP's), but these are not used in this study.
The generated air flow though the HVS has a rate of $0.5\,\mathrm{m^3\,min^{-1}}$ which result in a total sampling volume of $5040\,\mathrm{m^3}$ pr. week. This air flow was measured and noted during filter and PUF's change, but for weeks with missing notes, a standard volume flux of $V_{standard} = 5000\frac{m^3}{Week}$ were used instead in the calculations.

[1]The diameter for PM_{10} refers to the aerodynamic diameter of a spherical particle with a density of $1\,\mathrm{g\,cm^{-3}}$

Figure 4.4: The *filter pack sampler* located on the roof of Flygers hut, which consisted of nine arms, where one is used as reference and another as an extra. Underneath each arm is a light source to avoid frost and snow affecting the filter samples. (Photo: Bjarne Jensen, Institute of Environmental Science, Aarhus University.)

The *Filter Pack Sampler* (FPS) on the roof of Flygers hut (figure 4.4) is produced by NERI and consisted of 8 arms connected to a pump, which generated the air flow though, the filter samples. The FPS can operate in 7 weeks before it needs maintenance, because the eight arm is used as reference filters. The FPS operates on a weekly basis and the air flow sucked though the filter is $40\,\mathrm{L\,min^{-1}}$, which result in a total sampling volume about $400\,\mathrm{m^3}$ pr. week.
Underneath each arm is a light source in order to avoid hoar frost and snow to affect the filter samples. In each arm, a sequence of 3 filters are located inside, which have an internal diameter of 40 mm. The first filter collect particulate matter (*Heavy Metals* (HM), SO_4^{2-}, NH_4^+, SO_3^{2-} and NO_3^-). The subsequent filters is impregnate with sodium hydroxide that collect SO_2 and HNO_3. The third filter is impregnate with oxalic acid for collection of NH_3 [Heidam et al., 2004; Skov et al., 2006].

Sample technique

The HVS and the FPS use a pump to suck in the ambient air and generate an air flow through the instrument. The general mechanisms for deposition of particles on or inside a filter are listed below:

- Impaction: when a particle cannot follow the streamline, too big
- Interception: when a particle is too big to go through filter "holes"
- Diffusion or Brownian motion: can prohibit small particles to go through filter
- External forces: e.g. electrical forces

These deposition mechanisms depend on the flow situation in the nearby surroundings or inside the filter. A decreasing flow rate contribute to collecting larger particles and an increasing flow rate contribute to collecting smaller particles. However, particle deposition in filters are also a function of particle size and shape, but for the actual flow situation a good approximation is that the particle is spherical.

4.3 Instrumental methods

4.3.1 The Particle Soot Absorption Photometer

The *Particle Soot Absorption Photometer* (PSAP) located at Flygers hut at Station Nord (Figure 4.5b) is produced by Stockholm University.

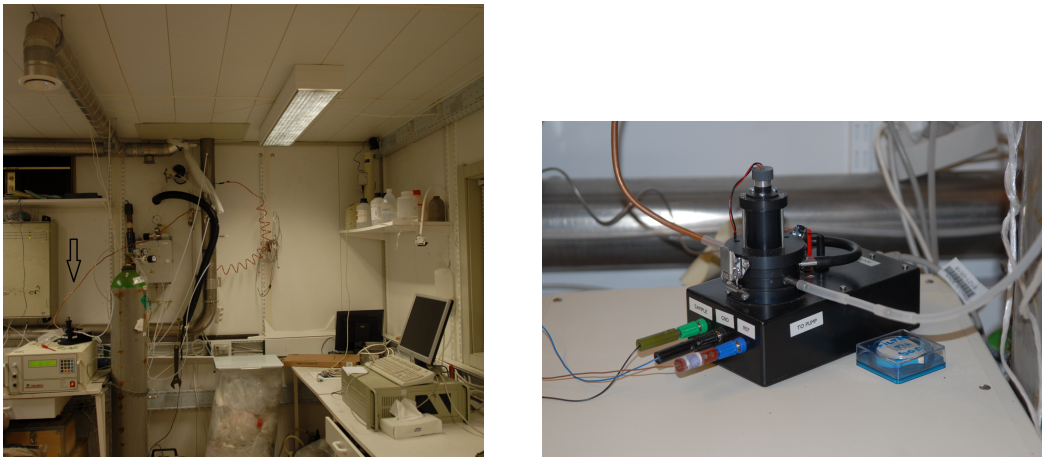

(a) Inside Flygers hut **(b)** The PSAP

Figure 4.5: (a) The *Particle Soot Absorption Photometer* (PSAP) inside Flygers hut, marked with a black arrow. (b) The PSAP at Flygers hut produced by Stockholm University. (Photo:Bjarne Jensen, Institute of Environmental Science, Aarhus University.)

It is one of a group of instruments which use the optical properties of particles to estimate the black carbon concentration. The PSAP located in Flygers hut is a filter-based instrument and actually most of the existent data are from these types of instruments. It is a favourable instrument, mainly because it is very stable over time, but also because it is cheaper compared with other instruments; it is easy to operate and transport; it does not need calibration and only a little maintenance.

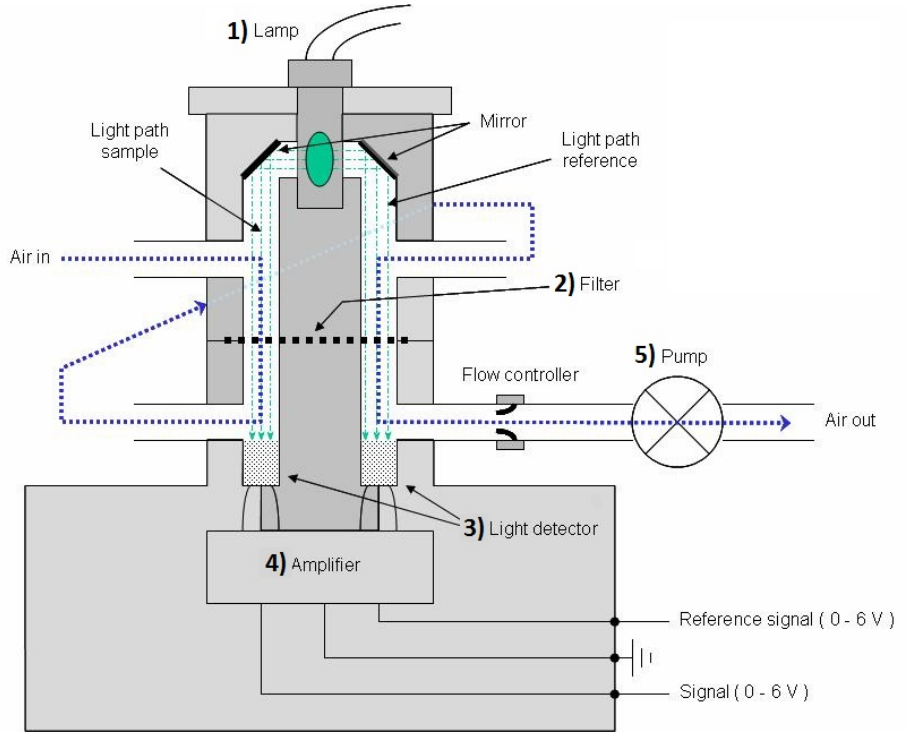

Figure 4.6: Sketch of the *Particle Soot Absorption Photometer* (PSAP), which consisted of a light source (**1**), a sample filter (**2**), two detectors (**3**), an amplifier (**4**) and a pump/blower (**5**) [Andersen, 2006].

The PSAP consist basically of 5 different parts as illustrated in figure 4.6. The light source (**1**), a light emitting diode operating at 550 nm and by a mirror divided in to two light beams. One of the light beams (Light path sample) strikes the collected particles on the filter (**2**), the *signal*, and the other light beams (Light path reference) strikes a clean filter, the *reference signal*, as shown in figure 4.6. The light source is divided into two light beams in order to correct for variations in incident light intensity and variations in the electronic drift [Weingartner et al., 2003]. Afterwards the two light beams are detected by the detectors (**3**) and converted to a voltage signal, which is increased by the amplifier (**4**). Then an analog digital converter change the signal from the amplifier to a digital signal than can be read by a computer.
The PSAP generates a signal every second continuously, which is averaged into fifteen minute intervals and loaded on a computer connected to a server at the Institute of Environmental Science, Aarhus University. The lower limit for the voltage signal from the PSAP is 3.5 V, which is the lowest quantity of voltage that can be distinguished from the noise level.
The pump (**5**) is generating an air flow though the PSAP (about $20\,\mathrm{ml\,min^{-1}}$), where particles from the ambient air are sucked in and collected on the filter. In order to avoid errors from top-laying of particles collected on the filter, a small flow rate is chosen. A large concentration of particles build up on the filter will result in a top-laying of particles, which will result in a misleading absorption coefficient, due to a non-linearity and collapsing of Beer-Lambert's law described in the following section 4.3.2. In order to avoid the above mentioned errors the filter has to be changed once in a while.

4.3.2 The measurements and calculations principle of PSAP

The measuring principle of PSAP is based on the change in optical transmission of a filter caused by particle deposition on a filter (Figure 4.7).

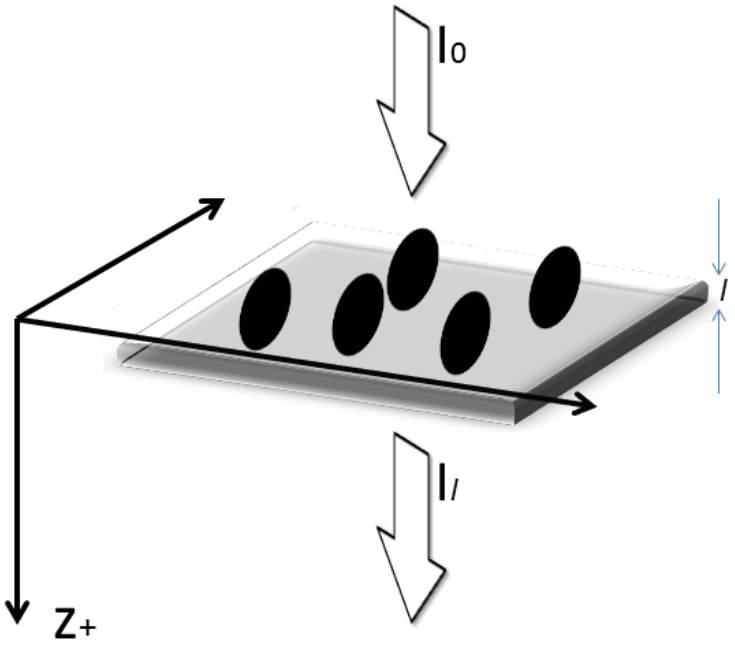

Figure 4.7: Light transmission through a filter loaded with particle. The particle is indicated with black circle and the light beam is indicated with white arrow.

Here the light source is placed perpendicular to the filter such that a photon is absorbed if it strikes the particle on the filter. Besides that, it is assumed that the particle has an *absorption cross section* (σ). The positive z-direction is defined as parallel to the direction of the light source and A and l is defined as the area and thickness of the filter, respectively. From this an expression for the absorption can be obtained:

$$dI_z = -\sigma N I_z \cdot dz \tag{4.1}$$

here dI_z is the number of photons absorbed by particles on the filter, N denotes the concentration of particles and I_z is the total number of photons from the source. In some cases the dimensionless scattering or absorption efficiency K_λ, defined in equation 2.6, is added to the aforementioned expression. In this cases the products of $N\sigma K_\lambda$ are termed *volume scattering*, *absorption-*, or *extinction- coefficients* [Wallace and Hobbs, 2006].
A final solution to equation 4.1 can be obtained by integrating the equation on both sides:

$$\int_{I_0}^{I_z} \frac{1}{I_z} dI_z = \int_0^z -\sigma N dz \quad for\ z \leq\ l \tag{4.2}$$

$$\begin{aligned} ln\,(I_z) - ln\,(I_0) &= -\sigma N(z-0) \\ &= -\sigma N z \end{aligned}$$

here I_0 is the intensity of the incoming light and I_l is the remaining light intensity after passing through the filter with the thickness z. When the difference of intensity across a filter with thickness $z = l$ can be expressed as:

$$ln\left(\frac{I_l}{I_0}\right) = -\sigma N l$$

The above equation is known as Beer-Lambert's law and perhaps more familiar as:

$$I(l) = I_0 \cdot \exp\left(-\sigma N l\right) \tag{4.3}$$

From Beer-Lambert's law the total *absorption* ($\tilde{\sigma}$) can be defined as:

$$\tilde{\sigma} = ln\left(\frac{I_l}{I_0}\right) = -\sigma N l \tag{4.4}$$

The PSAP measures the particles light absorption on a filter, also termed *light attenuation*, where two detectors monitor the light transmission through the filter. Since the concentration of particles N increase with time ($N(t) = \Delta N \cdot t$) on the filter it leads to $\tilde{\sigma} = -\sigma \Delta N l \cdot t$ and make the light absorption time depending. Then an expression can be obtained for change in total absorption ($\Delta\tilde{\sigma}$) during a time interval Δt:

$$\frac{\Delta\tilde{\sigma}}{\Delta t} = -\sigma \Delta N l \tag{4.5}$$

$$\Downarrow$$

$$\sigma = -\frac{\Delta\tilde{\sigma}}{\Delta t} \cdot \frac{1}{\Delta N l} \tag{4.6}$$

here can ΔN be expressed in relation with the filter area (A) and the volume flow ($\mathrm{Q} = \frac{N}{Volume}$) by $\Delta N \approx \frac{Q}{A \cdot l}$ which result in following expression:

$$\sigma = -\frac{\Delta\tilde{\sigma}}{\Delta t} \cdot \frac{A}{Q}$$

Furthermore, the change in total absorption ($\Delta\tilde{\sigma}$) can be expressed as:

$$\begin{aligned} \Delta\tilde{\sigma} &= \tilde{\sigma}(t + \Delta t) + \tilde{\sigma}(t) \\ &= ln\left(\frac{I_l(t + \Delta t)}{I_0}\right) - ln\left(\frac{I_l(t)}{I_0}\right) \\ &= ln\left(\frac{I_l(t + \Delta t)}{I_l(t)}\right) \end{aligned} \tag{4.7}$$

Then the aerosol *absorption coefficient* (σ_{abs}) due to light absorption of particles collected on a filter is defined as:

$$\begin{aligned} \sigma_{abs} &= -\frac{A}{Q} \cdot \frac{\Delta\tilde{\sigma}}{\Delta t} \\ &= \frac{A}{Q \cdot \Delta t} \cdot ln\left(\frac{I_l(t)}{I_l(t + \Delta t)}\right) \end{aligned} \tag{4.8}$$

σ_{abs} is not exactly correct, because of multiple scattering and absorbing of the light beam within the filter, which enhances the optical path and thereby enhance the light absorption of the deposited particles [Weingartner et al., 2003]. Therefore a

calibration constant C_{filter} is introduced in order to convert the PSAP measurements to empirical absorption coefficients. The corrected absorption coefficient is then determined as:

$$\sigma_{abs} = \frac{A}{C_{filter} \cdot Q \cdot \Delta t} \cdot ln\left(\frac{I_l(t)}{I_l(t+\Delta t)}\right) \tag{4.9}$$

where σ_{abs} is the corrected absorption coefficient in $[m^{-1}]$. C_{filter} is found by Bond et al. [1999] to be 2, but in this project a filter constant of 1 is used.
Instead of using the filter transmittances $I_l(t)$ and $I_l(t+\Delta t)$ the detected signals in [V] is used to obtain the absorption coefficient from the PSAP. The finally equation is:

$$\sigma_{abs} = \frac{A}{C_{filter} \cdot Q \cdot \Delta t} \cdot ln\left(\frac{(\frac{S}{S_R})_t}{(\frac{S}{S_R})_{t+\Delta t}}\right) \tag{4.10}$$

where S is the detected signal in [V], S_R is the detected reference signal in [V], Q is the air flow through the filter in $[L\,min^{-1}]$ and Δt is the time between the measuring points in [min]. The theoretical behaviour of the detected signals and a constant absorption coefficient is shown in figure 4.8. The reference signal S_R

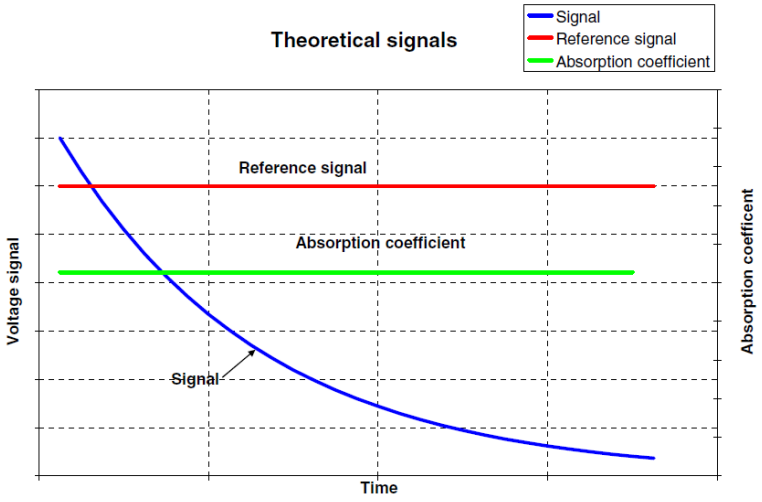

Figure 4.8: Theoretical signals in case of constant absorption coefficient [Andersen, 2006].

should theoretical be a constant and if the absorption coefficient is assumed to be constant, the detected signal S will behave as a decreasing function as illustrated in figure 4.8.
It is found by Petzold et al. [1997] and several authors that the absorption coefficient is linearly related to specific black carbon mass loading on the filter by the following relation:

$$C_{Black\ Carbon} = \frac{\sigma_{abs}}{\sigma_{specific}} \qquad \left[\frac{\mu g}{m^3}\right] \tag{4.11}$$

From this equation the data is converted to concentration of black carbon, by using the *specific absorption coefficient* ($\sigma_{specific}$). The specific absorption coefficient is found by Horvath [1993] for airborne black carbon particles of $8\,m^2\,g^{-1}$ to $10\,m^2\,g^{-1}$

in the visible spectral region, but Petzold et al. [1997] reports a variability in this coefficient, which seems to depend on regional variations of the predominant aerosol type. The observed variability ranges from $5\,m^2\,g^{-1}$ in remote areas to $14\,m^2\,g^{-1}$ at urban locations and to $20\,m^2\,g^{-1}$ at near-street measuring sites.

Uncertainty in the PSAP measurements

The uncertainty related to the BC concentrations reported from the PSAP has to be estimated in order to use the BC concentrations in COPREM, see section 4.5. In order to estimate the uncertainty a similar PSAP instrument was set up in the basement at the Department of Environmental Science, Aarhus university, as shown in figure 4.9a. A pump was connected to the PSAP to generate an airflow through the instrument and a PM_{10} capsule particle filter was also connected to the instrument to avoid particles from the ambient air to affect the detected voltage signal.

(a) The set up at NERI

(b) The Bubble Flow Meter

Figure 4.9: a) Setup of the PSAP in the basement at NERI with airflow generated by the blue pump and a white cylindrical PM_{10} capsule filter. b) the Bubble Flow Meter made by Gilibrato to measure the flow rate.

To ensure that the airflow corresponds to the PSAP at Flygers Hut the airflow was calibrated. This was done with a *Bubble Flow Meter* which is an instrument produced by Gilibrato (Figure 4.9b). The Bubble Flow Meter generates a bubble in a cylindrical tube and an infrared sensor reads the flow rate of the bubble as it propagates up through the cylindrical tube. The final airflow for the similar PSAP instrument was measured by the Bubble Flow Meter as $20.07\,ml\,min^{-1}$. The final uncertainty obtained in this investigation is found in chapter 5 in section 5.2.1

4.3.3 Analysis of organic and elemental carbon in aerosols

The weekly filter samples from the HVS with a volume flow of $500\,\mathrm{L\,min^{-1}}$, were analysed for *organic and elemental carbon by a carbon analyser* (OC EC analyser) from Sunset Laboratory, which analyse organic and elemental carbon in aerosol filter samples.

A standard sized punch of $2.5\,\mathrm{cm^2}$ or $1.5\,\mathrm{cm^2}$ were made of the weekly sample filters from the HVS in the time periods from July 2008 to February 2011 as shown in figure 4.10. Then the standard sized filter was placed on the support tray, and when the OC EC analyser (*the oven*) was closed, the oven were purged with *helium* (He) and the temperature started to increase as illustrated in figure 4.11. First, the temperature is ramped in an inert He atmosphere. During the temperature ramps, in the first step, the OC is greatly released from the filter punch and subsequently reduced by *Manganese dioxide* (MnO_2) catalyst which converts OC species to *methane* (CH_4). The methane is then continuously measured by a *flame ionization detector* (FID).

Figure 4.10: Sample filter from a HVS, where a standard sized punch of $2.5\,\mathrm{cm^2}$ is punched out.

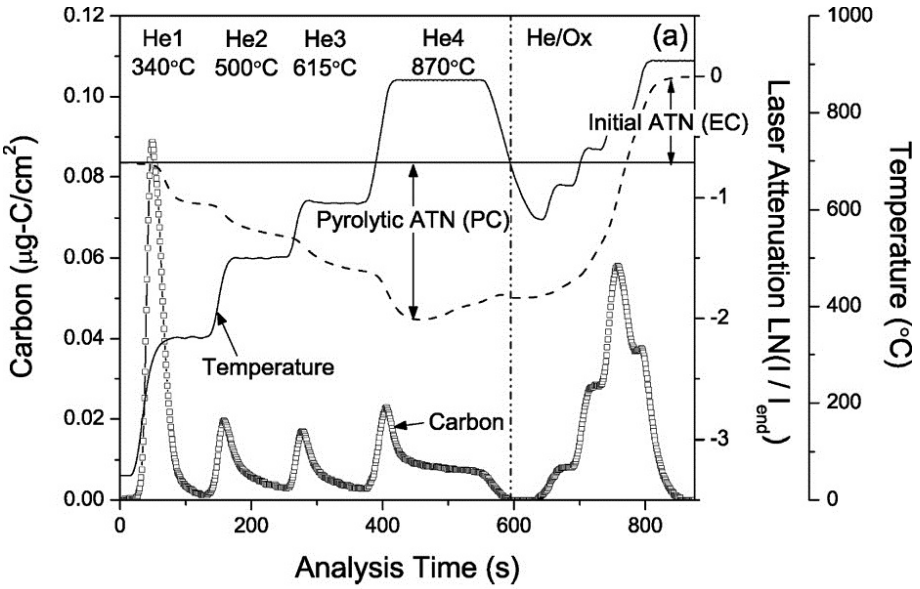

Figure 4.11: Analysis of organic carbon and elemental carbon performed by a *carbon analyser* (OC EC analyser). The process is divided into two steps which has different temperature ramp indicated in the top of the figure. Here the splitting point of the two steps is found just below $800\,^{\circ}\mathrm{C}$.

Afterwards, the second step occur when the OC EC analyser is cooled to 550 °C and oxygen is introduced into the He flow. EC is then oxidized and released from the filter, and the following detection in the same manner as the OC. In the first step elemental carbon can be formed by charring (carbonization) of OC as it pyrolyzes which results in an overestimation of EC. To avoid this a red light laser which use the high absorbance of EC is placed in the instrument. When the elemental carbon, which resulted from charring during the first step is oxidized and released in the second step it decreases the absorbance of the filter sample, and when the transmittance meets the initial value before the first step, the split point is reached. Any elemental carbon detected before this point is defined to have been formed by charring of organic carbon. This carbon is subtracted from the elemental carbon and assigned as organic carbon.

The practical use of OCEC analyzer

Before starting to analyse the standard size filter from the HVS, the different rates of gas flow into the OC EC analyzer have to be set as listed in table 4.2. The flow rate of H_2 has at first to be settled to circa $100\,\mathrm{cc\,min^{-1}}$ to ignite the flame in the FID detector. Hereafter, the flow rate of H_2 can be set. To ensure that the OC EC analyser is functioning well a $1.5\,\mathrm{cm}^2$ standard size sample containning a sugar solution was placed on the support tray for analysis. The result of elemental carbon from the sugar solution should be $43.3\,\mu\mathrm{g}\ \pm 2\,\mu\mathrm{g}$ and then the OC EC analyser is ready for analysing the standard size filter of $2.5\,\mathrm{cm}^2$ from Station Nord.

Table 4.2: The interval of gas flow for the OC EC analyzer.

The different gasses	**Flow rate interval** $[\mathrm{cc\,min^{-1}}]$
Air	280-300
H_2	52-54
He -1	52-56
He -2	12-15
He -3	67-70
He/O_2	12-15
Cal	10-15

4.3.4 The Proton Induced X-ray Emission

The sample filters from the *filter pack sampler* at Flygers hut are analysed for chemical elements with an atomic number larger than Al by the PIXE method. *Proton Induced X-ray Emission* (PIXE) is a method used for determining the elemental composition of a sample on e.g. a filter. A sample filter is exposed to incident proton beams, which results in excitation of inner shell electrons. This leads to emissions of electromagnetic radiation of wavelengths in the X-ray part of the spectrum (Figure 4.12a). The ionization due to incident ion beams is shown in figure 4.12b, where A) illustrates a k-shell ionization and B) illustrates an X-ray photon emission.

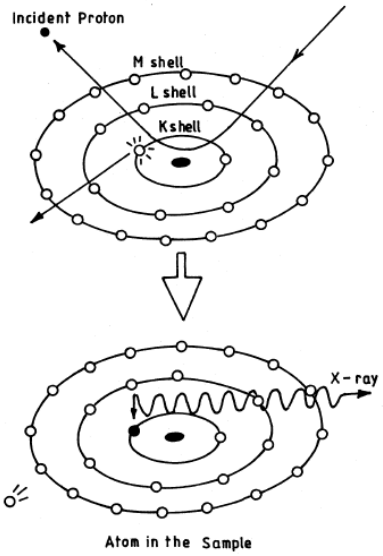

(a) The basic principle of PIXE

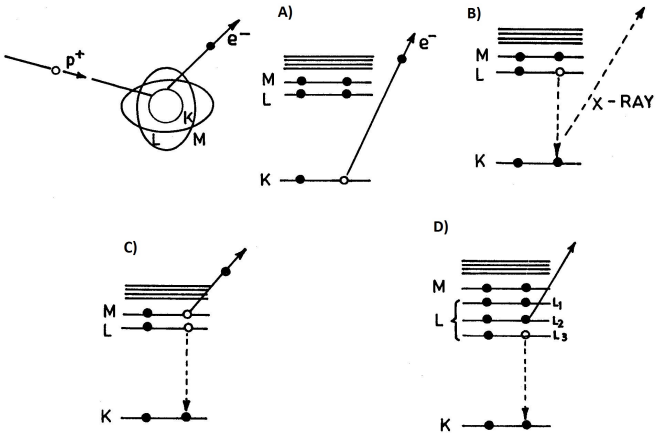

(b) Ionization

Figure 4.12: a) Illustration of a sample filter exposed to incidental ion beams, which result in emissions of electromagnetic radiation. b) Ionization due to charged particle bombardment. A) K-shell ionization, B) X-ray emission, C) Auger transitions and D) Coster-Kroning transitions [Govil, 2001].

The total X-ray from an excited target atom is affected by two different processes: the Auger and Coster-Kronig transitions. Auger transitions are a process which arise from the electrostatic interaction between two electrons in an atom that is ionized in the inner shell (Figure 4.12b C)). This can result in X-ray emissions during the electron re-ording process that takes places after the Auger electron emission. The Coster-Kronig transitions are a process which takes place between the sub-shells of the same shell (Figure 4.12b D)). Besides that, the X-ray signal from the trace elements on the filter can also be affected by an unwanted background in the spectrum. This background level can occur from bremsstrahlung[2] or from discrete peaks arising from interfering X-rays from the material [Govil, 2001]. In general, there is a high probability that a number of X-ray peaks will be overlapping or interfering each other and thereby give rise to an uncertainty of the

[2]Bremsstrahlung (German, from bremsen "to brake" and Strahlung "radiation") refer to process where electromagnetic radiation is produced, e.g. deceleration of a charged particle.

elements determined by the PIXE-method.

In figure 4.13 the analysis of an environmental sample is shown. This is obtained by taking into account an internal standard spectrum of each element, when the amount of the single elements are determined on the basis of the areas of the corresponding peaks. The final analysis is performed by the staff at the Department of Environmental Science, Aarhus University.

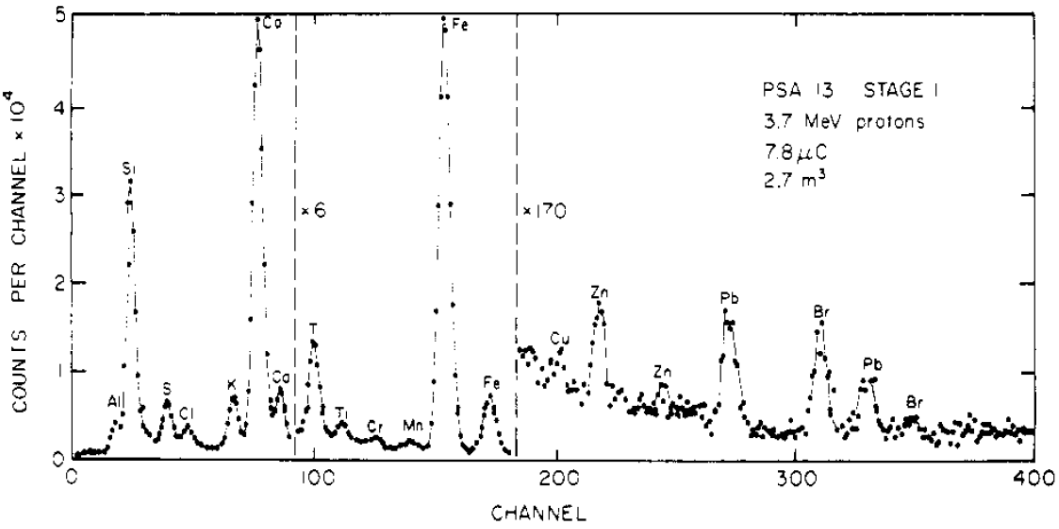

Figure 4.13: X-ray spectrum obtained by proton irradiation of an aerosol filter sample. Here the different elemental peaks are clearly seen [Johansson et al., 1975].

4.4 Modelling methods

4.5 The Constrained Physical Receptor Model

Linking emissions from sources to chemical species which is transformed into particulate matter and measured at a given site (a receptor point) is a complicated task. Source to receptor modelling is an available tool to predict the linking of the spatial observations in the Arctic with emissions from different sources from outside the Arctic.
An example of this type of model is the *Constrained Physical Receptor Model* (COPREM) developed by Waahlin [2003]. It is a receptor model, which combines qualities from *chemical mass balance* (CMB) and *positive matrix factorisation* (PMF). The CMB models are based on the knowledge of the number of sources, such as wood, combustion and traffic, but also knowledge about their chemical composition at the receptor site. In this way the model operate with sources that are constant for all samples/elements and thereby ignoring chemistry occurring along the transport way or the chemistry occurring at the site.
The PMF attempt to divide the observed concentrations at the receptor site between the different sources by using statistics. The distance between the observed concentrations and the model result is minimized by χ^2.
These methods derived the measured concentrations of the pollutant component x_{ij} of n different chemical components in N samples into a linear combination of contributions from different sources, by the following expression:

$$x_{ij} \simeq \sum_{k=1}^{p} a_{ik} f_{kj} \tag{4.12}$$

here the coefficients a_{ik} represent the source profile that is the load of component i in source k and f_{kj} represent the strengths of the source k found in the individual sample j. Again the index i refers to the n chemical variables, index j refers to the N samples and index k refers to the p sources [Heidam et al., 2004; Waahlin, 2003]. The solution for f_{ik} is obtained by minimizing the *Error* E:

$$E = \sum_{j} \sum_{i} \frac{\left(x_{ij} - \sum\limits_{k} a_{ik} f_{kj} \right)^2}{\sigma_{ij}^2} \tag{4.13}$$

here σ_{ij} represents the uncertainty of the data assuming x_{ij} to be gaussian with mean given by equation 4.12 and variance σ_{ij}^2. E is then χ^2 distributed with $n \cdot N - np$ *degrees of freedom* (dof).

The minimizing of E can be seen as measuring the total squared distance between the measurements and the model result in a vector space. This is done in units of the uncertainties of the data, but with the limitations imposed by the matrix profile [Waahlin, 2003].

The practical use of COPREM

As input for the COPREM model three matrices are needed: An $n \times p$ *profile matrix* (Right Table 4.3) which contains the initial source vector, an $n \times p$ *form matrix* (Left Table 4.3) which contains information about the n chemical variables which either is fixed $= 0$ or free $= 1$ to vary and then a $2 \times n \times N$ data matrix which contains the measured values and their uncertainties.
The initial sources contain the knowledge of the chemical elements and their individual ratio between each other for the four different sources (Right Table 4.3). This is the basis for COPREM in order to determine the elements source apportionment. Furthermore, in the form matrix (Left Table 4.3) the specific compounds are either allowed to vary or fixed (if they are well-known). These two matrices allow a better control over the final source apporionment result, but also require more input information.

Table 4.3: The $n \times p$ *form matrix* (Left) which contains information about the n chemical variables which either is fixed$= 0$ or free$= 1$ to vary. The $n \times p$ *profile matrix* (Right) which contains the initial sources vector. Here *Com.* denotes the Combustion source and the blue colour indicate change from Heidam et al. [2004] original form and source matrix. The red colour indicate the added elements.

Element	Soil	Sea	Com.	Metal	Soil	Sea	Com.	Metal
(Al)	1	0	0	0	0.0813	0.5	0	0
(Si)	0	0	0	0	0.2	0.02	0	0
(S)	0	0	1	1	0.00052	880	0	0
(cl)	0	0	0	0	0.00048	18900	0	0
(K)	0	0	1	1	0.025	378	0	0
(Ca)	1	0	0	0	0.058	800	0	0
(Ti)	0	0	1	0	0.00455	0	0	0
(V)	1	0	0	1	0.00011	0.0024	0.14	0
(Cr)	0	0	1	0	0.0002	0	0	0
(Mn)	0	0	1	0	0.0007	0.000995	0.27	0
(Fe)	0	0	0	1	0.04	0.002	0	2
(Ni)	0	0	1	1	0	0.0001	0	0
(Cu)	0	0	0	0	0.00001	0	0.1	1
(Zn)	0	0	1	1	0.00008	0.005	0	0
(Ga)	0	0	1	0	1.5E-06	0	0	0
(As)	0	0	1	0	0.00001	0.01	0	0
(Se)	0	0	1	0	9E-07	0.004	0	0
(Br)	0	0	0	0	2.5E-06	65	0	0
(Rb)	0	0	0	0	0.000031	0.12	0	0
(Sr)	0	0	1	0	0.0002	20	0	0
(Zr)	1	0	1	0	0.00022	0	0	0
(Pb)	0	0	0	0	0.000006	0.004	2	0
(SO_4^{2-})	0	0	0	1	5.20E-07	1	0.2	0.095
BC	0	0	1	1	0	0	0.08	0.012

The uncertainty is required for obtaining the final solution f_{ik} and the uncertainty used for the elements are listed in table 5.6 in section 5.6. The uncertainty is required for the limit of the vector spaces where the final solution can be found. The uncertainties are especially important for data near the detection limit, as the BC concentrations. This is taking into account by minimizing the Error E, which guarantees that concentrations with high uncertainties will have a small weight in the solutions process, and vice versa [Waahlin, 2003].

The COPREM model runs through EXCEL 2003 via a *Visual Basic for Applications* (VBA) macro, where the worksheets contains the profile-, form- and data-matrix. The COPREM repetition occurs in a Command Prompt Window which shows the running values of $\frac{E}{dof}$, number of dof and the squared standard deviation of all calculated source strengths. When those values seems constant the COPREM are stopped manually by pressing any key in the Command Prompt Window. Then the scatter plot, the series plot and the contributions plot for the different compounds can be investigated together with the suggested profile matrix from COPREM and the E-value for the total and the individual element. When some new knowledge is obtained and used as input in a new profile matrix and when COPREM is running again.

Chapter 5

Results and discussion

In this chapter the results obtained throughout this study are presented and discussed. First, the state of the Northern Hemisphere is analysed for winter periods 2007/2008, 2008/2009, 2009/2010 and 2010/2011. This is carried out by analysing the different indices together with a study of the 500 mb geopotential height-contours. Afterwards the measured concentrations from the PSAP and the OC EC analyser are presented, respectively. Subsequently, the concentrations reported from the PIXE method are presented and analysed. Here, a special attention is made on sulphate concentrations in comparison with BC concentrations. Finally, analyses of the characteristic sources are presented by considering the final source apportionment achieved from the COMPREM model.

5.1 The Arctic winter atmosphere

The transport of particular matter to the Arctic appears to be influenced by the overall Northern Hemispheric circulation, especially in winter. Therefore, the Arctic atmospheric conditions were investigated for the period from October 2007 to April 2011. This analysis of the upper-level circulation was with focused on the strength of the Polar Vortex.
In this study, the analyse of 500 mb geopotential height contours from the NCEP/NCAR reanalysis from National Oceanic and Atmospheric Administration (NOAA 2) and U.S. Department of Commerce [2011] was used. The 500 mb geopotential height-contours were chosen to represent the Polar Vortex at the middle troposphere and in accordance to the topography of Greenland. In addition, the 300 mb height surface is used in an analysis to represent the Polar Vortex by Angell [2006], because the north circumpolar vortex is best defined at this jet stream level near the top of the troposphere. If the 300 mb geopotential height were chosen in this study it would only represent the upper level circulation in the troposphere. Furthermore, in years with a persistent Polar Vortex it can be argued that the 850 mb geopotential height-contours also represent the Polar Vortex.

Winter 2007/2008

In figure 5.1 the modes of *Arctic Oscillation* (AO), *North Atlantic Oscillation* (NAO) and *Pacific-North American Oscillation* (P-NAO) are shown for the winter period 2007/2008. During autumn 2007 the AO mode and the NAO mode slowly built up towards a high positive mode with indices around one in winter 2007/2008. These positive modes exist until March 2008, where the NAO mode decreases to more neutral states, but the AO mode continues a positive mode. During the spring 2008 both indices decrease towards negative mode. The P-NAO mode increases in autumn 2007, but generally in the winter 2007/2008 it shifts between positive and negative modes. Therefore the P-NAO is assumed to be more or less in a neutral state in this winter.

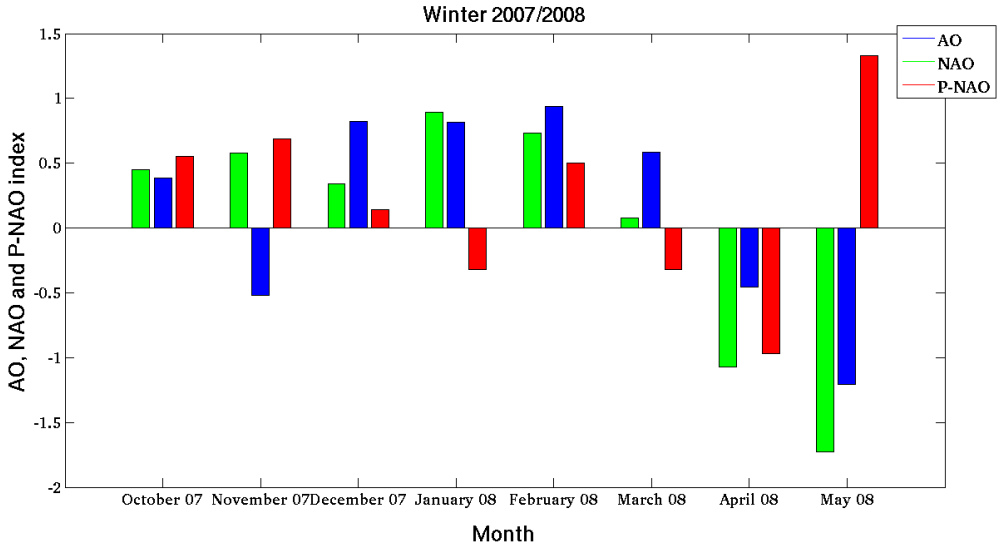

Figure 5.1: The mode of Arctic Oscillation, North Atlantic Oscillation and Pacific-North American Oscillation in the winter period 2007/2008. Here a positive mode of the indices is dominating the winter. The observed modes are from [National Oceanic and Atmospheric Adminstration (NOAA 1), 2011].

The 500 mb geopotential height-contours are shown in figure 5.2 for the winter period 2007/2008 in (a) December/January, (b) February and (c) March. These height-contours reflect the strength of the Polar Vortex[1], which for this winter is found as a very strong persistent vortex. In December 2007 to February 2008 the Polar Vortex is dominating the Arctic atmosphere and the related dry and cold air mass is located across the Arctic region. In March 2008 the boundaries of the Polar Vortex have retreated further to the North and the Polar Vortex is weakened. The retreat occurs already in February 2008 (Figure 5.2b) in the Alaska site of the Arctic region. Here the P-NAO mode shifts toward a positive mode and allows warm and humid air masses from the Gulf of Alaska, North Pacific Ocean, to move

[1]with strength of the Polar Vortex refers to the persistent and the distribution of the dry and cool air-mass in the Arctic region, which is reflected into the expansion or retreat of the Polar Vortex.

northward.
In general, the strength of the Polar Vortex is highly reflected in the persistent positive AO and NAO mode during this winter. This behaviour indicates a very stable Polar Vortex and a more zonal (west-east) wind pattern. This limits the exchange of air masses between the Arctic and the sub mid-latitude and results in more homogeneous air masses covering the Arctic region. This is also associated with enhance transport of polluted air masses from the north mid-latitudes into the Arctic. Furthermore, the homogeneous dry and cold air masses which provides better condition for accumulation of particulate matter in the Arctic winter troposphere.

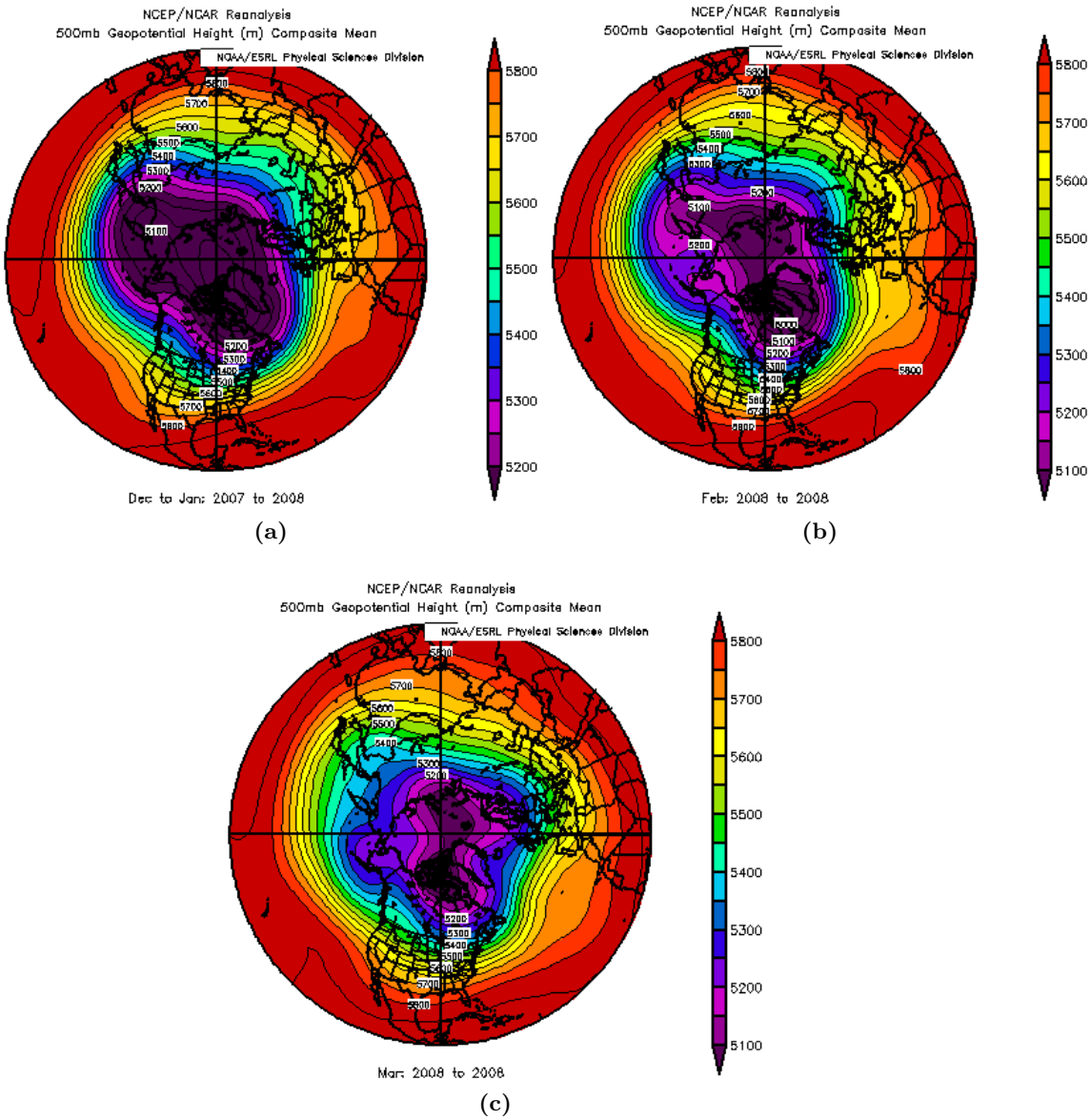

Figure 5.2: Arctic atmospheric pressure $500\,\mathrm{mb}$ geopotential height-contours observed for winter period 2007/2008 in December/January, February and March [National Oceanic and Atmospheric Administration (NOAA 2) and U.S. Department of Commerce, 2011].

Winter 2008/2009

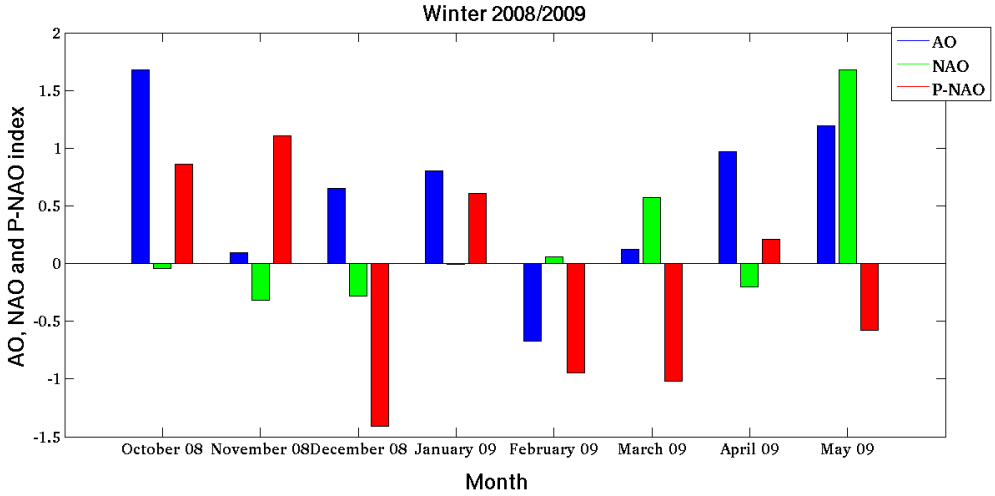

Figure 5.3: The mode of Arctic Oscillation, North Atlantic Oscillation and Pacific-North American Oscillation for the winter period 2008/2009. The observed modes are from [National Oceanic and Atmospheric Adminstration (NOAA 1), 2011].

In figure 5.3 the AO mode, the NAO mode and the P-NAO mode are shown for the winter period 2008/2009. The NAO mode is found in a neutral state in this winter and it never achieves a high positive mode in this winter. In the spring 2009 it suddenly shifts to a high positive mode, which extends into the late spring. Comparing the NAO mode with the NAO mode of winter 2007/2008, the NAO mode behaves completely opposite. Where it was expected to be positive it was found as a neutral or even negative mode. Further, in spring where it was expected to slowly decrease towards a negative mode, it shifts into a more positive mode.

The AO mode is found most presented in the high positive mode during autumn 2008 and early winter 2009. In February 2009 the AO mode shifts toward a negative mode, where afterwards it slowly increases to a more positive mode during the spring season. The P-NAO mode slowly increase towards a high positive mode during autumn 2008, but shifts to a negative mode in December 2008 which almost exists up to March 2009. This should theoretically lead to cold and dry air masses from the north-western Canada to move southward and thereby expand the Polar Vortex in this area of the Arctic. This is to some extent also reflected in figure 5.4b and 5.4c. For the rest of the spring 2009 the P-NAO mode shifts into more neutral modes.

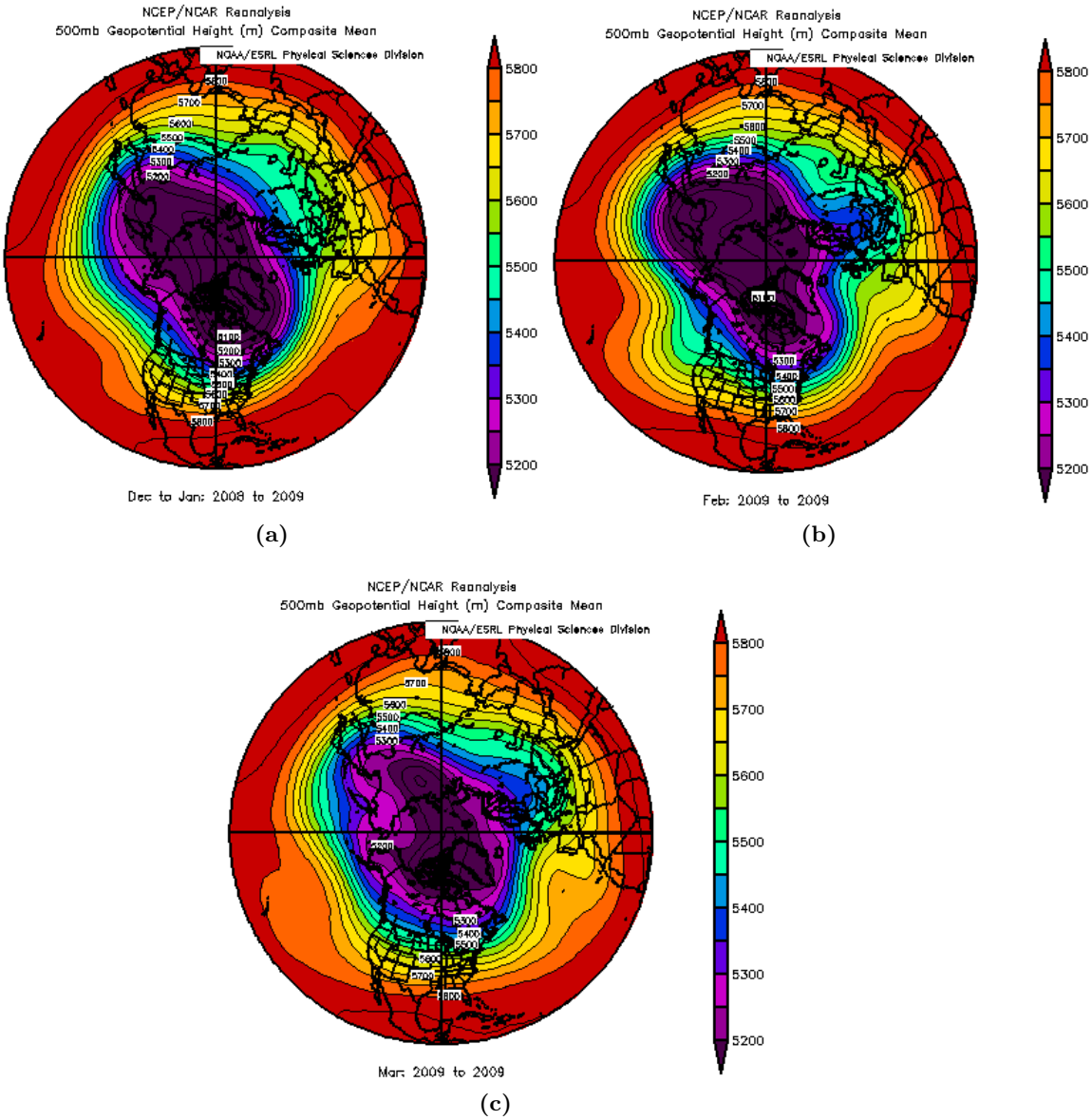

Figure 5.4: Arctic atmospheric pressure 500 mb geopotential height-contours observed for winter period 2008/2009 in December/January, February and March [National Oceanic and Atmospheric Administration (NOAA 2) and U.S. Department of Commerce, 2011].

The 500 mb geopotential height-contours are shown in figure 5.4 for the winter period 2008/2009 in (a) December/January, (b) February and (c) March. The period with the strongest Polar Vortex in winter 2008/2009 is found in December 2008 and January 2009 (Figure 5.4a). This is also reflected in the positive mode of AO.

In February 2009 the Polar Vortex is still dominating the Arctic region and the boundaries have strengthens over Europe and Western Asia, which also is indicated with a negative AO mode. In the rest of the Arctic region the Polar Vortex has retreated further to the North. In March 2009 an additional weakening of the Polar Vortex occurs, especially over the Siberian side of the Arctic region. This is also

reflected in the neutral state of the indices of AO and NAO. Besides the weakening on the Siberian side, the Polar Vortex expands a bit on the North-western Canada side of the Arctic, which is reflected in the negative state of the P-NAO mode (Figure 5.4c).
In general, this winter period is dominated of different modes of the indices. This should theoretically lead to more meridional winds and a greater exchange of air masses between the Arctic and the sub mid-latitude. This results in more humid air masses within the Arctic which enhance the wet deposition of particulate matter. Furthermore, the Polar Vortex this winter period strengthens over Europe and Western Asia which theoretically would enhance polluted air masses from this site (receptor site) to be transported into the Arctic.

Winter 2009/2010

In figure 5.5 the AO mode, the NAO mode and the P-NAO mode is shown for the winter period 2009/2010. This autumn, winter and spring is dominated of neutral or negative indices of AO and NAO.

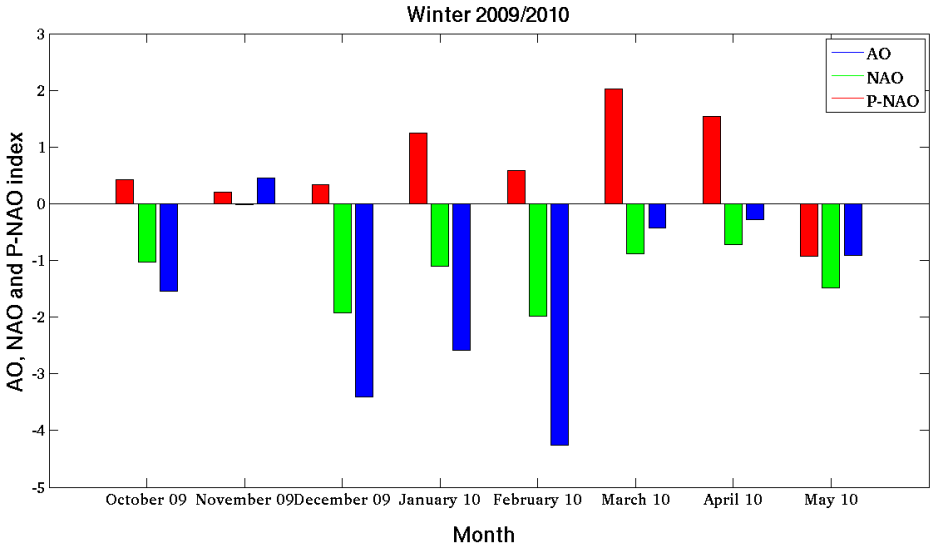

Figure 5.5: The mode of Arctic Oscillation, North Atlantic Oscillation and Pacific-North American Oscillation for the winter period 2009/2010. The observed modes are from [National Oceanic and Atmospheric Adminstration (NOAA 1), 2011].

The AO mode obtains the lowest index value in December 2009 and February 2010, where the NAO mode follows the same tendency, but not with the same magnitude as the AO mode. In early spring both indices shifts from very negative indices towards more neutral modes, which persist into the late spring 2010. The P-NAO mode in autumn and early winter is in the neutral mode, but increases during January 2010. Then in early spring 2010 the P-NAO mode shifts to high positive modes.

The 500 mb geopotential height-contours are shown in figure 5.6 for the winter 2008/2009 in (a) December/January, (b) February and (c) March. The strength of

the Polar Vortex is not that persistent during this winter atmosphere compared to the winter period of 2007/2008. In general, the Polar Vortex is divided into two smaller vortices, roughly found over Baffin Island in Canada and in the area of the Bering Strait (Figure 5.6b). This increase the north-south (meridional) winds and allows cold air masses to move southward and to be replaced with warm air masses moving northwards.

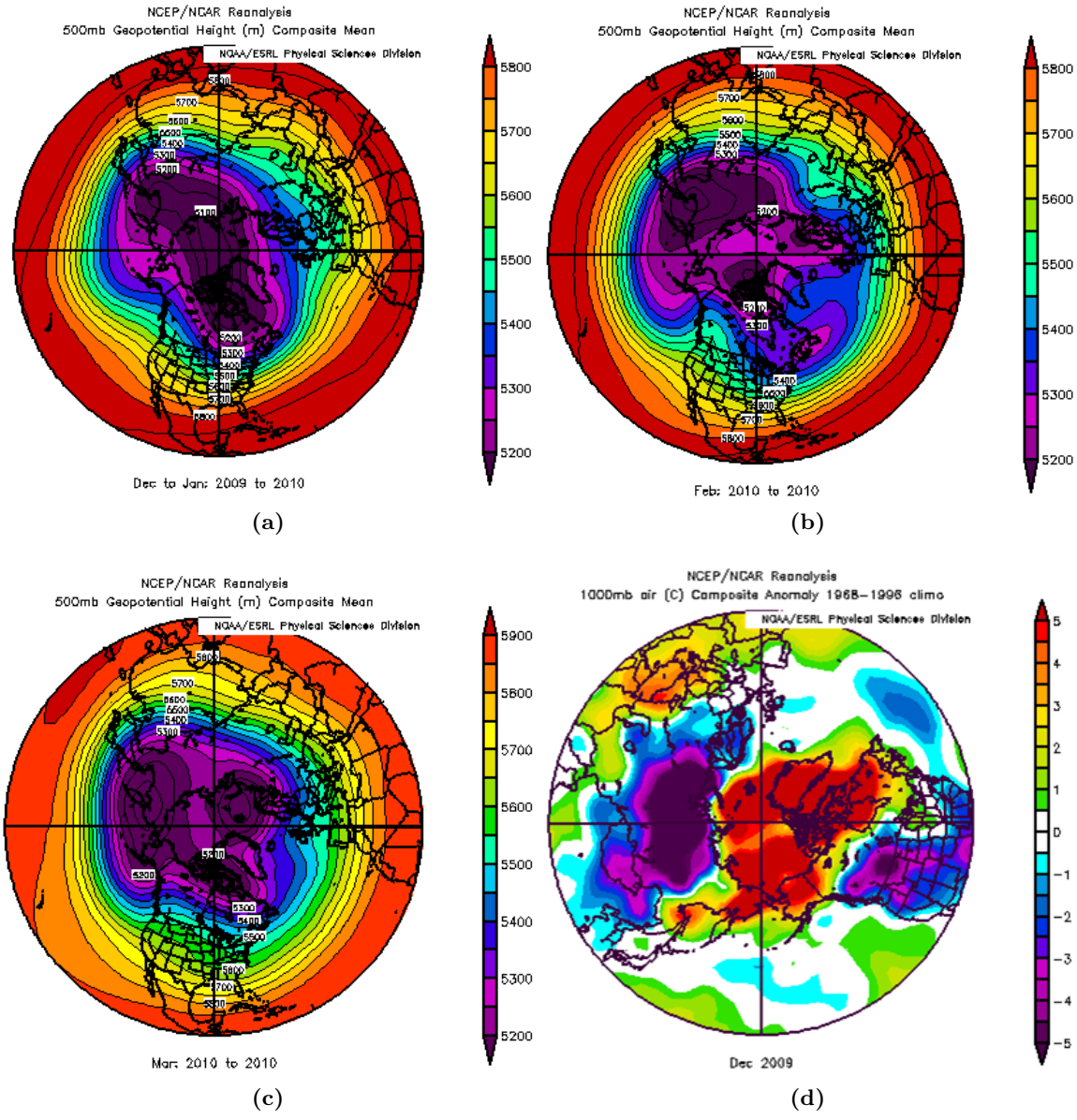

Figure 5.6: Arctic atmospheric pressure $500\,\mathrm{mb}$ geopotential height-contours observed for winter period 2009/2010 in (a) December/January, (b) February and (c) March. In (d) the temperature Anomalies for December 2009, where an extreme negative AO-mode occur [National Oceanic and Atmospheric Administration (NOAA 2) and U.S. Department of Commerce, 2011].

According to Overland [2011] this results in a breakdown of the Polar Vortex in December 2009 and again in February 2010, which is clearly seen in figure 5.6b and the 850 mb geopotential height-contours in appendix (Figure A.3). This is also highly reflected in the AO mode and the NAO mode for the same months. Actually the winter of 2009/2010 occurred with the most negative NAO-index in the 145 years of the record. This extreme negative mode led to temperature anomalies which indicate a warm Arctic and cold continents (Figure 5.6d).
In general, the indices and the two small vortices (weak Polar Vortex) this winter period indicate even greater exchange of air masses between the Arctic and the sub mid-latitudes. Therefore the transport of polluted air masses into the Arctic this winter is limited, because it is most likely that the wet deposition of particulate matter has been dominating rather than accumulation of particulate matter in the Arctic winter troposphere. Furthermore, the found temperature anomalies which indicate a warm Arctic and cold continents indicate the very unstable atmospheric situation this winter period and thereby the high exchange of air masses.

Winter 2010/2011

Figure 5.7 shows the AO mode, the NAO mode and the P-NAO mode for winter 2010/2011. Here the autumn and winter is dominated of negative indices for the AO mode and the NAO mode.

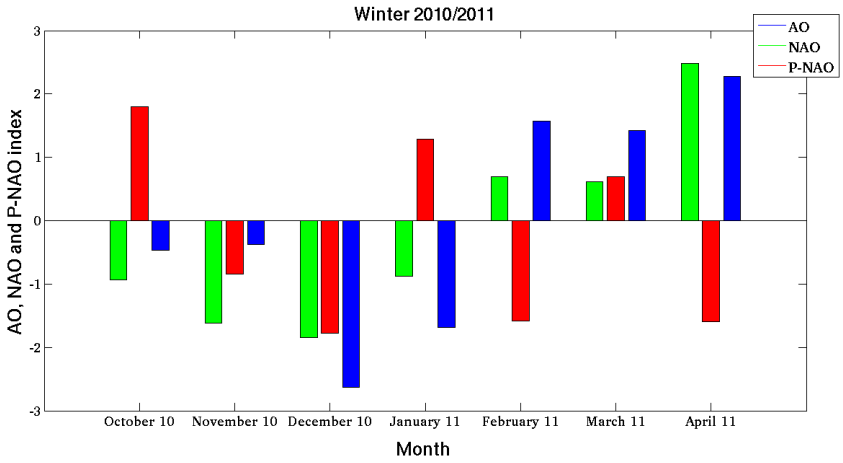

Figure 5.7: The mode of Arctic Oscillation, North Atlantic Oscillation and Pacific-North American Oscillation for the winter period 2010/2011. The observed modes are from [National Oceanic and Atmospheric Adminstration (NOAA 1), 2011].

In December 2010 the AO mode shifts into a strong negative index, but not as strong as in February 2010. In the early spring the AO mode and NAO mode shift towards more positive mode, which is the dominating pattern for the AO mode and the NAO mode in spring 2011. The P-NAO mode is negative during the late autumn and early winter, but in January 2011 it changes towards a positive mode. In the spring season it shifts between positive and negative indices. In figure 5.8, the 500 mb geopotential height-contours are shown for the winter period 2010/2011 in (a) December, (b) January, (c) February and (d) March.

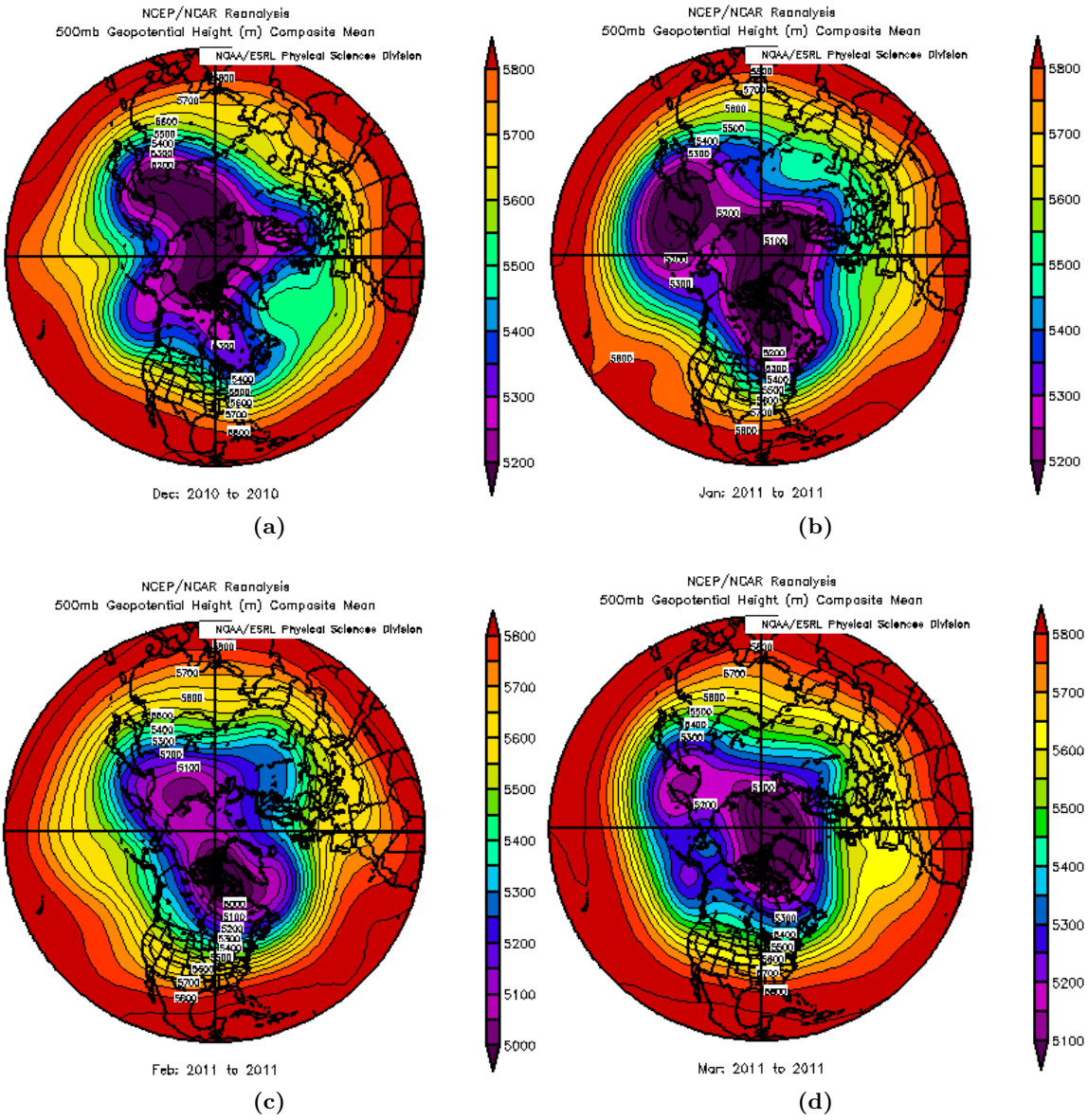

Figure 5.8: Arctic atmospheric pressure 500 mb geopotential height-contours observed for winter period 2010/2011 in (a) December, (b) January, (c) February and (d) March [National Oceanic and Atmospheric Administration (NOAA 2) and U.S. Department of Commerce, 2011].

In this winter a weak Polar Vortex is dominating the Arctic winter atmosphere, especially in December 2010. The lowest negative AO mode this winter is also found in December 2010, which indicates an increase in meridional winds and an exchange of air masses between the Arctic region and the sub mid-latitudes. This is to some extent reflected in the strength of the Polar Vortex for December 2010 (Figure 5.8a). Here the Polar Vortex consists of one core. If the 850 mb geopotential height-contours are investigated, as shown in appendix in figure A.3c, the weakening of the Polar Vortex is seen even more clearly. Here the weakened Polar Vortex has a core divided into 4 small vortices. In January 2011 (figure 5.8b) and February 2011 (figure 5.8c) the Polar Vortex is divided into two vortices, roughly found over

North-east Canada and east Siberia. In February and March 2011 the AO mode is increasing towards a positive mode. This is also reflected in the strength of the Polar Vortex, which rebuilds to a single core, roughly found over Baffin Bay and North Greenland in March 2011.

In December 2011 and January 2011 the effect of a negative and positive P-NAO mode is clearly reflected in the strength of the Polar Vortex on the Canadian side of the Arctic region. In figure 5.8a the cold dry air masses are moving southward and are located over Alaska and North-western Canada. This is due to the increase of meridional winds during a negative P-NAO mode. In January the P-NAO mode shifts into a positive mode which is reflected in figure 5.8b where the cold and dry air masses are located over the eastern Canada instead.
In general, this winter period is very similar to the winter period of 2009/2010 with a high exchange of air masses between the Arctic and the sub mid-latitude. Furthermore, is some period (January and March) with a positive P-NAO mode the transport of particulate matter from the eastern Canada has better condition to reach the Arctic region. Therefore is it more likely that the polluted air masses in this winter situations is from this site.

5.1.1 Summary

It appears that the NAO mode has some association with the AO mode, which probably reflects the interaction between the different atmospheric phenomena the AO mode and the NAO mode describes. In general, the AO mode and the NAO mode describe the strength of the Polar Vortex core located over Baffin Island in Canada and North-east of Greenland, where the P-NAO mode more describes the strength of the Polar Vortex core found over Alaska and North-western Canada. In addition, the strength of the Polar Vortex on the Siberian side of the Arctic region is difficult to address with these indices. After this study of the Polar Vortex the AO mode is found to be the best indicator of the strength of the Polar Vortex on the Siberian site.

From this analysis of the actual flow pattern (the strength of the Polar Vortex) the Arctic winter atmosphere in the winter period of 2007/2008 is found to be the most favourable for transport of polluted air masses into the Arctic and for accumulation of particulate matter in the Arctic troposphere. This is due to the high positive modes of AO and NAO which reflected a very stable atmosphere in the Arctic and thereby limit the exchange of air masses between the Arctic and the sub mid-latitude (more zonal winds). Further, the positive AO and NAO mode was also reflected in the strength and expansion of the Polar Vortex and results in a homogeneous cold and dry air mass covering the Arctic troposphere. Thereby provides better condition for accumulation of particulate matter in the Arctic winter troposphere. Furthermore, the strength of the Polar Vortex this winter enhance the transport of polluted air masses into the Arctic, because a larger fraction of the Northern Hemispheres air masses has the same potential temperature as the Arctic region (see section 3.5). A sufficiently colder receptor site in winter helps to meet the requirement that the polluted air masses shall have the same potential

temperature as the Arctic region in order to be transported into the Arctic region.

The winters of 2008/2009, 2009/2010 and 2010/2011 were characterized by an increase in meridional winds, which allow cold and dry air to move southward and be replaced by warm more moist air masses, especially in late autumn and early winter of 2008 and 2010. This result in a flow pattern where exchange of air masses between the Arctic and the sub mid-latitudes is dominate and enhance the deposition of particulate matter. Furthermore, the strength of the Polar Vortex is not that persistent during these winter and thereby limits the amount of polluted air masses to reach the Arctic region according to fulfill the assumption of the same potential temperature as the receptor site.

The low sea ice extent in the Arctic Ocean in the last few years, are suggested by Overland and Wang [2010] to work against the stability of the Polar Vortex. The new ice-free areas in the Arctic Ocean is seen as a heat transfer between the ocean and the atmosphere (Figure 5.9). "These temperatures contribute to an increase in the 1000 hPa to 500 hPa thickness field in every recent year with reduced sea ice cover" [Overland and Wang, 2010]. If this is the case it can perhaps explain the very unstable Polar Vortex in winter of 2008/2009, 2009/2010 and 2010/2011.

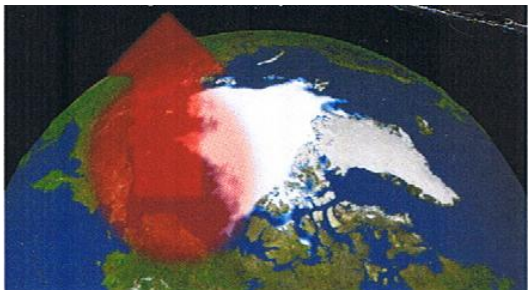

Figure 5.9: Added ocean heat storage and heat flux from new ice free areas works against the stability of the polar vortex [Overland, 2011].

5.2 Processing of PSAP-data

The PSAP-dataset is covering the period from March 2008 to April 2011 and in order to *quality control* the dataset, the behaviour of the voltage signals *real signal* (S) and the *reference signal* (RS) were investigated. The quality control was performed in order to detect any outliers or obvious not-normal behaviour of the instrument reflected in the dataset. The detected signal S was only allowed to decrease due to the accumulation of particles on the filter. The detected signal RS should theoretically be constant, but it was allowed to vary in a limited range. Besides that, the detected voltage signals were not allowed to be below 3.5 volt according to a specific noise limit of the instrument.

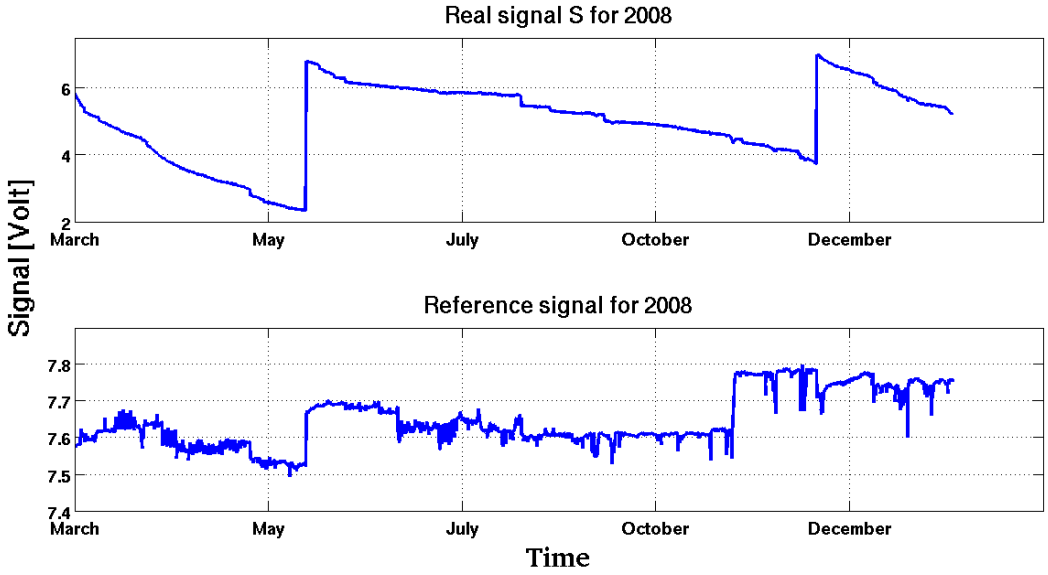

Figure 5.10: The voltages signal from the PSAP at Station Nord in the period March 2008 to December 2008. Other years (2009/2010/2011) can be found in appendix A.

In figure 5.10 the signal S and signal RS are shown for 2008 and the voltage signals from the PSAP in 2009, 2010 and 2011 can be found in appendix A, figure A.2.
In the voltage signal S high steps occurred which are due to filter changes of the PSAP (clean filter results in low absorption, reflected in higher voltage signal S). In general, the signal S varies between 2 V to 6.5 V and the detected signal S decreases slightly over the time as expected. The detected voltage signal RS varies between 7.5 V to 7.8 V, which is considered as a very limited size range and therefore meets the assumption of constant behaviour.
In autumn 2009 and spring 2010 small fluctuations in the voltage signals S occurred regularly. These fluctuations in signal S were assumed to be assigned to daily temperature variations, because the air-conditioning in Flugers hut was inoperative in some periods, especially in 2010. The voltage signals S were compared to temperature measurements from another instrument located in Flygers hut (Figure not shown), thus this assumption was rejected.

The quality control was further performed on the light absorption coefficient (σ_{abs}), calculated from the detected signals S and RS by using equation 4.10, in time intervals of 15 min for the period covering March 2008 to April 2011. Here, very high light absorption coefficients were assigned to local pollution at Station Nord (*local activity*[2]) or systematic failure behaviour of the instrument. In spring 2010 (the same period with small fluctuations) very high values occurred compared to other years. These high values were marked and then excluded from the dataset as potential outliers.

The measurements of the light absorption coefficient were converted to BC concentrations according to equation 4.11, where a specific absorption coefficient ($\sigma_{specific}$) of $10\,\mathrm{m^2\,g^{-1}}$ was used. A $\sigma_{specific}$ of $10\,\mathrm{m^2\,g^{-1}}$ was chosen according to a study by Ström [2010] and for further explanation see section 5.5.

In order to analysis the dataset, it was thought that the Grubb's test could be applied on the BC concentrations with a time resolution of 15 min. The Grubb's test is a statistic tool to determine outliers and is explained in appendix A. The BC concentrations are expected to be log-normal distributed and therefore can the test only be applied to positive concentration values. The PSAP detects values very close to the detection limit and result in negative and also zeros concentrations and therefore failed the test on this dataset.
Thus, the Grubb's test was performed on BC concentration averages of daily values. This was done in order to eliminate the random error by negative and zeros concentration values obtained from the PSAP instrument, but where the systematic error would still be representative. Negative BC concentrations were still found in this dataset, but those were limited and determined as outliers. In addition, negative values in the daily dataset are associated with mass loss on averages of the filter, which is not physically acceptable.

	BC (1)	BC (2)	Final BC
$G \gg$	4.0086	4.0071	4.0128
G_{test} MAX	9.4625	2.9234	4.3707
G_{test} MIN	12.4560	3.7638	4.1702
N	884	876	896

Table 5.1: The result from the Grubb's test on different daily BC concentrations, where G denotes the critical value. BC (1) denotes the Grubb's test on the 15 min BC concentration averages into a daily time resolution. BC (2) denotes the dataset where the detected outliers by the first Grubb's test is eliminated. Final BC denotes the dataset where both the *quality control* and the Grubb's test is performed on the BC concentrations.

[2] *Local activity* is reflecting emissions from waste burning, snow removal at the airfield or air-transport to and from Station Nord. In some special meteorological cases emissions from local activity can reach Flygers hut.

The result from the Grubb's test is listed in table 5.1. Here, the test did confirm outliers in the daily BC concentration dataset. These values were compared to *the quality control* of the dataset, where the behaviour of the absorption coefficient and the voltage signals S and RS were investigated. This comparison confirmed most of the noted outliers in *the quality control* as an outlier.

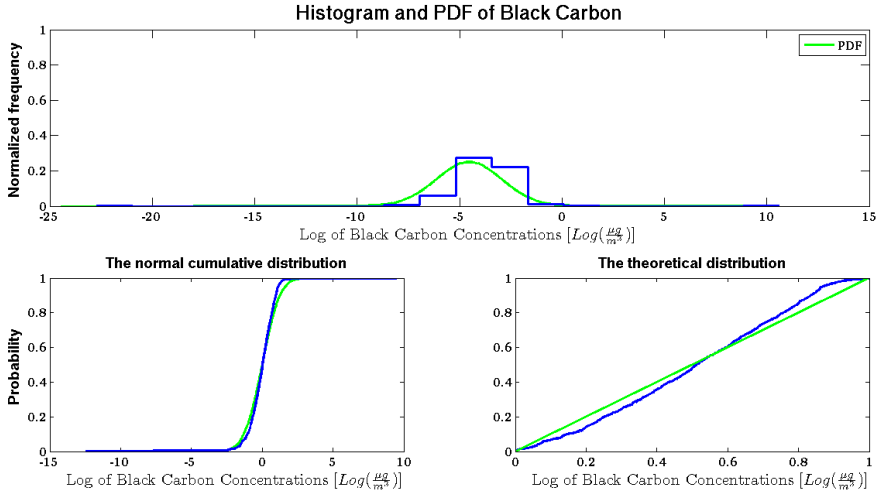

(a) With outliers

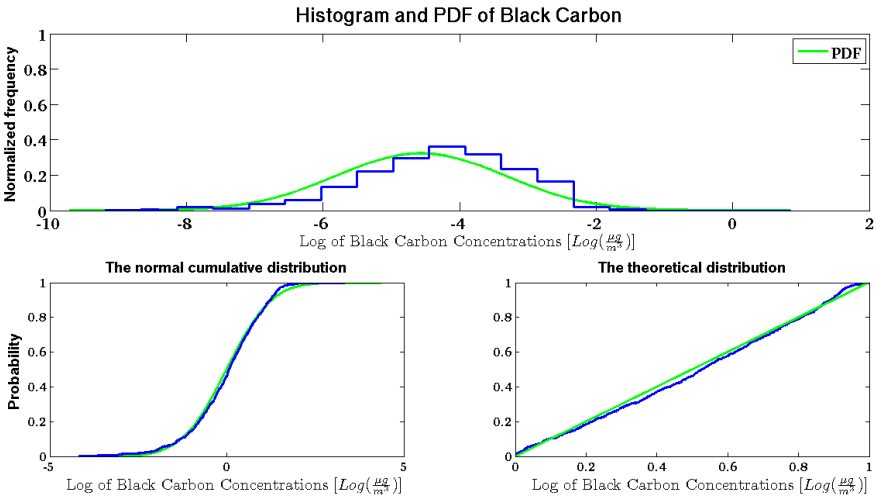

(b) Without outliers

Figure 5.11: The distribution of the daily BC concentrations from March 2008 to February 2011. (a) the daily BC concentrations with outliers and (b) the final daily BC concentrations, where the *quality control* and the Grubb's test is performed on the dataset.

Afterwards, the distribution of the daily BC concentrations was explored both with the outliers and without the outliers determined by the Grubb's test. In figure 5.11a, the distribution of the BC concentrations with outliers is shown. The outliers cause the dataset to deviate from the theoretical expected distribution. If the outliers, confirmed by the Grubb's test, are eliminated from the daily BC concentrations, the distribution of the BC concentrations is very close to the theoretical distribution as

shown in figure 5.11. The distribution of the final *quality controlled* Grubb's tested daily BC concentrations, which are used in the following sections, were investigated by the probability distribution as shown in figure 5.11b. This shows a reliable dataset without any significant outliers which follows the theoretical distribution very well.

5.2.1 Uncertainty on BC concentrations

The uncertainty on BC concentrations was needed as input data for the COPREM model. Therefore another PSAP-instrument of the same type, was set up at Department of Environmental Science, Aarhus University, as described in chapter 4, section 4.3.2.
The BC concentrations are defined from the linear relation in equation 4.11, but the related uncertainty on the absorption coefficient (σ_{abs}) and the specific absorption coefficient ($\sigma_{specific}$) is not known.

Factors	Value
Area ($\frac{1}{4}\pi r^2$)	$\pi \cdot 10^{-6}$ [m^2]
Flow Q	20 [ml min^{-1}] $= 2 \cdot 10^{-6}$ [L Week^{-1}]
Mean Signal S	9.1079 [Voltages]
Δ_A	$5\% \sim 1.57 \cdot 10^{-7}$
Δ_Q	$5\% \sim 1 \cdot 10^{-7}$
$\Delta_{S,weekly}$	0.0183

Table 5.2: The parameters which contribute to the estimate of the uncertainty of the BC concentration.

Therefore, to estimate the BC uncertainty (Δ_{BC}) it was assumed that the only contributor was from σ_{abs}, which has a contribution from the signal S, the area A and the volume flow Q ($\sigma_{abs} = f(S, A, Q)$). This leads to the following expression:

$$\sigma_{abs} + \Delta\sigma_{abs} = f(S, A, Q) + \frac{df}{dS} \cdot \Delta S + \frac{df}{dA} \cdot \Delta A + \frac{df}{dQ} \cdot \Delta Q$$

Here σ_{abs} is the absorption coefficient and $\Delta\sigma_{abs}$ is the uncertainty of the absorption coefficient. The variance (σ^2_{SAQ}) of the measurement of σ_{abs} is obtained from:

$$\begin{aligned} \left\langle (\sigma_{abs} + \Delta\sigma_{abs})^2 \right\rangle &= \sigma^2_{abs} + 2\sigma_{abs} \left\langle \Delta\sigma_{abs} \right\rangle + \left\langle \Delta\sigma^2_{abs} \right\rangle \\ &= f(S, A, Q)^2 + \left\langle \Delta\sigma^2_{abs} \right\rangle \\ &= f(S, A, Q) + \sigma^2_{SAQ} \end{aligned} \tag{5.1}$$

Then the uncertainty is expressed by the *error propagation equation*:

$$\begin{aligned}\sigma_{SAQ}^2 &= \left\langle \Delta\sigma_{abs}^2 \right\rangle \\ &= \left\langle \left(\frac{df}{dS} \cdot \Delta S + \frac{df}{dA} \cdot \Delta A + \frac{df}{dQ} \cdot \Delta Q \right)^2 \right\rangle \\ &= \left(\frac{df}{dS} \right)^2 \cdot \left\langle \Delta S^2 \right\rangle + \left(\frac{df}{dA} \right)^2 \cdot \left\langle \Delta A^2 \right\rangle + \left(\frac{df}{dQ} \right)^2 \cdot \left\langle \Delta Q^2 \right\rangle \\ &+ \frac{df}{dS}\frac{df}{dA} \cdot \langle \Delta A \cdot \Delta S \rangle + ...5terms\end{aligned}$$

Here $\langle \Delta A \cdot \Delta S \rangle = 0$, because the measured parameters are uncorrelated and therefore the 6 terms disappear and the final equation for the uncertainty on BC can be expressed as:

$$\sigma_{SAQ} = \sqrt{\left(\frac{df}{dS} \right)^2 \cdot \langle \Delta S^2 \rangle + \left(\frac{df}{dA} \right)^2 \cdot \langle \Delta A^2 \rangle + \left(\frac{df}{dQ} \right)^2 \cdot \langle \Delta Q^2 \rangle} \tag{5.2}$$

$$= 0.1666 \quad m^{-1} \tag{5.3}$$

Here the calculated parameters are listed in table 5.2, where the mean value of voltage signal S over a week are used together with the known area of the filter and volume flow for a week. To obtain Δ_{BC} the linear relation in equation 4.11 was used and result in following expression:

$$\begin{aligned}\Delta_{BC} &= \frac{\sigma_{SAQ}}{\sigma_{specific}} \\ &= \frac{0.1666 \text{ m}^{-1}}{10 \text{ m}^2 \text{ g}^{-1}} \\ &= 0.0166 \quad [\text{g m}^{-3}]\end{aligned} \tag{5.4}$$

This gives a final uncertainty of 0.0166 g m^{-3} on the BC concentration and is illustrated in figure 5.12.

5.2.2 Final BC concentrations

The *quality controlled* daily BC concentrations were averaged into weekly values, where the number of measurements were taken into account through a weighted average. The weekly averages of BC concentrations from March 2008 to April 2011 at Station Nord are shown in figure 5.12, where a specific absorption coefficient of $10\,\text{m}^2\,\text{g}^{-1}$ was used (See also section 5.5). Those concentrations show seasonal variations in accordance with the Arctic haze cycle. The greatest concentrations if found in December to April or March (about $60\,\text{ng m}^{-3}$) and the lowest concentrations from June to September (about $7\,\text{ng m}^{-3}$).
Generally for the four-year period, there is a decrease in winter BC concentrations at Station Nord. The winter of 2007/2008 has maximum BC concentrations of $110\,\text{ng m}^{-3}$ where the winter BC in 2008/2009 ($20\,\text{ng m}^{-3}$ to $60\,\text{ng m}^{-3}$), in winter 2009/2010 ($20\,\text{ng m}^{-3}$ to $40\,\text{ng m}^{-3}$) and in winter 2010/2011 ($15\,\text{ng m}^{-3}$ to $50\,\text{ng m}^{-3}$) were found well below the winter 2007/2008 high BC event.

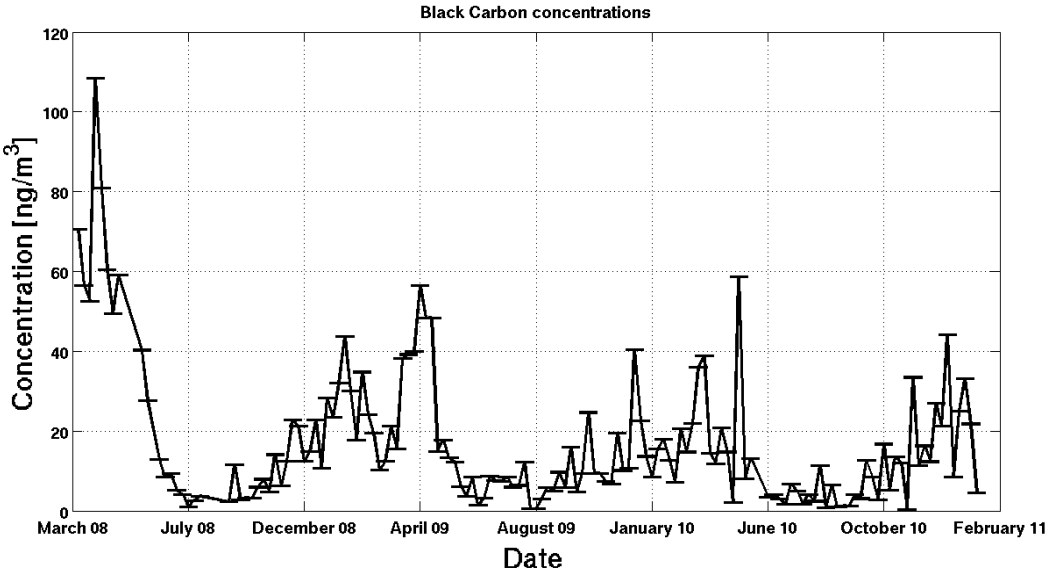

Figure 5.12: Weekly BC concentrations in $[\mathrm{ng\,m^{-3}}]$ during the period of March 2008 to February 2011. The measurements originate from the PSAP at Flygers Hut at Station Nord by using a specific absorption coefficient of $10\,\mathrm{m^2\,g^{-1}}$.

In comparison, reported BC concentrations from the measuring station Alert, Canada (62.3°W, 82.5°N, 210 m ASL) and the measuring station Zeppelin on Svalbard, Norway (11.9°E, 78.9°N, 478 m ASL), shows the same seasonal variation. At Alert the highest BC concentrations (about $125\,\mathrm{ng\,m^{-3}}$) are found in the period from January to March and the lowest (about $15\,\mathrm{ng\,m^{-3}}$) from June to September, in the measuring period from 1989 to 2005 [Quinn et al., 2011]. At Zeppelin on Svalbard the highest BC concentrations (about $60\,\mathrm{ng\,m^3}$) are found in the period from January to March and the lowest (about $10\,\mathrm{ng\,m^{-3}}$) from June to September, in the measuring period from 1998 to 2008 [Quinn et al., 2011]. This seasonal variation is in accordance with the Arctic haze cycle, which also has maximum concentrations during the winter and early spring and minimum concentrations in the summer. To some extent, this seasonal cycle is also found in the indices of AO, NAO and P-NAO and the related strength of the Polar Vortex.

In winter times such as winter 2007/2008, where a strong Polar Vortex is dominating the Arctic troposphere and the AO and the NAO mode is high, isolation is dominating the Arctic atmosphere (Section 5.1). Furthermore, the Polar Vortex is located further to the south in winter, which allow polluted air masses from the sub and mid-latitudes with the same low potential temperature as in the Arctic region to reach the Arctic.
This leads to an isolation of the dry stable Arctic air masses found in the troposphere, which inhibit removal processes of particulate matter from the Arctic atmosphere and led to a accumulation of aerosol particles. In addition, mixing of the dry Arctic air masses (cA) with more moist Polar and Tropical air masses (mP, mT) is very limited in this winter situation and more common in the Arctic summer. A mixing with more moist air masses would increase the removal processes by particulate matter acting as a CCN. In comparison, for the summer

months the mixing is much more pronounced in the Arctic troposphere, which enhances the removal processes of particulate matter in the troposphere. This is also reflected in BC concentrations in summer, where the lowest concentrations is found.

5.3 BC concentrations from Flade Isblink ice core

The high BC event in winter 2007/2008 was not measured in the subsequent year and the measured BC concentrations for this winter period were limited at Station Nord. Therefore it is interesting to see if other years with high BC concentrations events also were associated with a strong Polar Vortex reflected in the AO and NAO mode.
The BC dataset from the Flade Isblink ice core was analysed together with the AO, NAO and P-NAO in the time period from 1950 to 2000 [Joseph R. McConnell, 2011, Private communication].

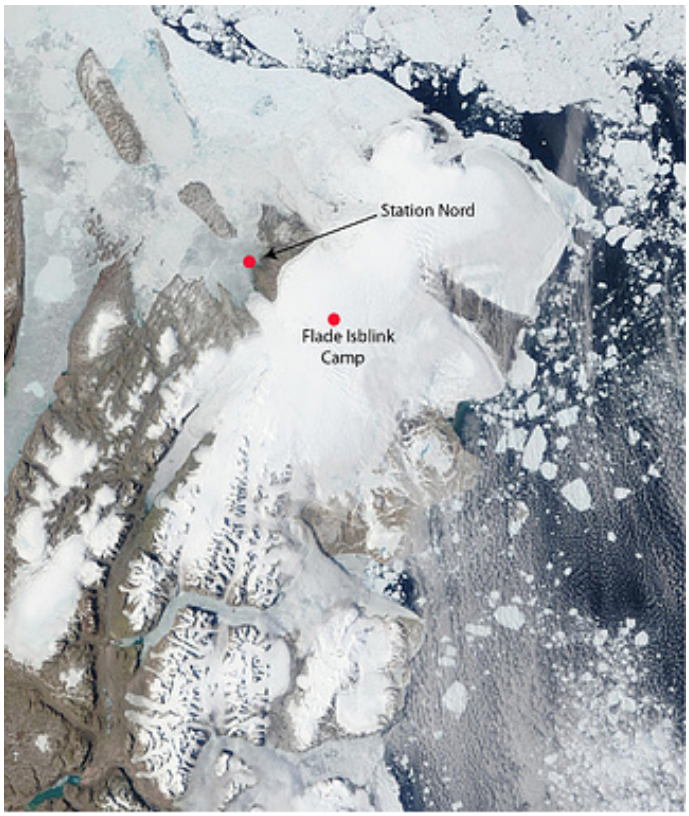

Figure 5.13: Kronprins Christian Land, where Station Nord and Flade Isblink is located. The Flade Isblink Camp is located about 30 km from Station Nord [Flade Isblink, 2011].

Flade Isblink is an isolated ice cap located close to Station Nord on Kronprins Christian Land as shown in figure 5.13. The ice cap has a surface area of 5000 km^2 and covers 100 km in the North-South direction and about 50 km in the West-East direction. The average height of the underlying bedrock is 100 m ASL and the

thickness of the ice cap reaches approximately 600 m [Lemark, 2010].
In the summer of 2006, a group led by the Centre for Ice and Climate, Copenhagen University, started a drilling of an ice core at the summit of Flade Isblink (about 30 km from Station Nord).

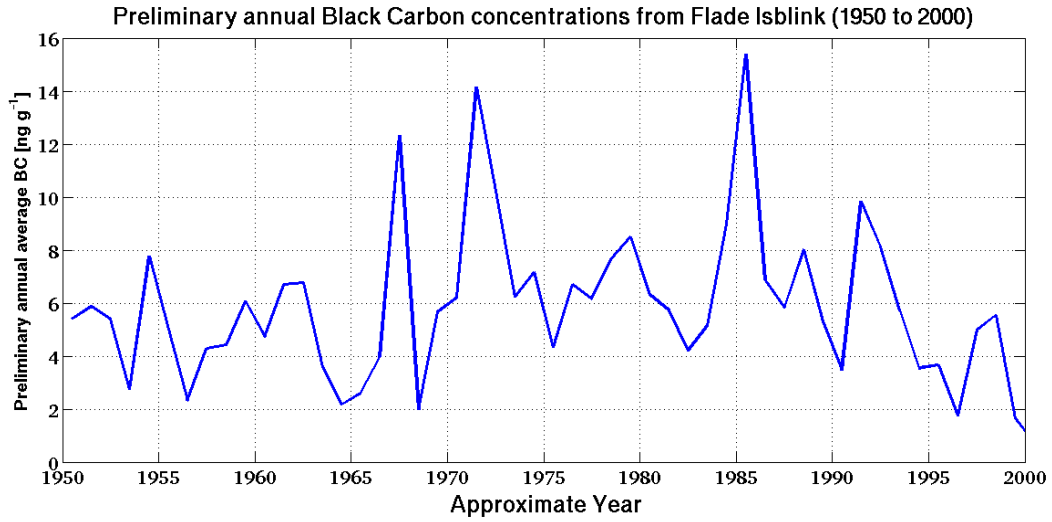

Figure 5.14: Preliminary annual Black Carbon concentrations [$\mathrm{ng\,g^{-1}}$] from Flade Isblink ice core in the period from 1950 to 2000. The preliminary dating result in a uncertainty of $\pm$ 4 years [Joseph R. McConnell, 2011, Private communication].

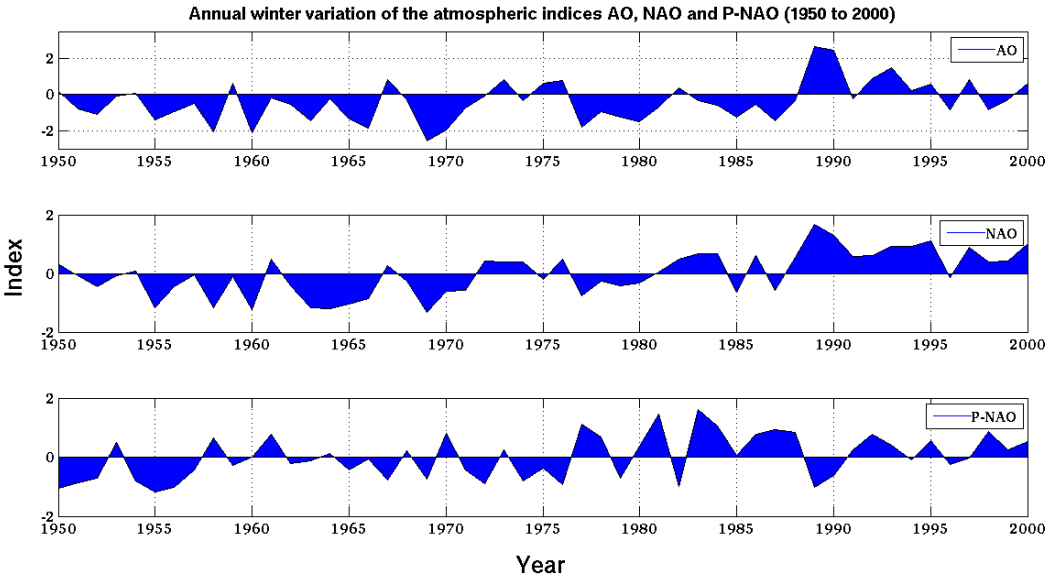

Figure 5.15: Annual variation of the atmospheric indices AO, NAO and P-NAO during the winter season. Here the winter season is represented with the mean of January, February and March indices [National Oceanic and Atmospheric Adminstration (NOAA 1), 2011].

The preliminary annual average BC concentrations from 1950 to 2000 are shown in figure 5.14. Here, the preliminary dating is based on two depth points: the surface and the summer 1783 (Laki volcanic eruption). This give a estimated uncertainty to ± 4 years. There is some variation in the BC concentrations over the decades, but also over the whole period (1950-2000). In the time period from 1950 to 2000 four high BC events occur; two in the period from 1968 to 1974 (mean about $7.38\,\mathrm{ng\,g^{-1}}$), one about 1985 (about $14\,\mathrm{ng\,g^{-1}}$) and again in the early 1990s (about $10\,\mathrm{ng\,g^{-1}}$). In comparison, the period from 1950 to 1966 (mean about $4.56\,\mathrm{ng\,g^{-1}}$) is presented by stable and lower BC concentrations.
The annual winter variation in the atmospheric indices AO, NAO and P-NAO is shown in figure 5.15 from 1950 to 2000. In general, from the 1950s through the early 1970's the winter indices were in a negative or neutral mode. Then from the 1970s through to the mid-1990s, the indices were more represented in their positive winter mode, while since then they have in general been found in a positive mode, except AO which since the mid-1990s has relaxed towards neutral modes.

If the four episodes with high BC concentrations are linked with the indices of AO, NAO and P-NAO it is found that:

- the events of high BC concentration in 1967 (about $12\,\mathrm{ng\,g^{-1}}$) and 1971-1972 ($10\,\mathrm{ng\,g^{-1}}$ to $14\,\mathrm{ng\,g^{-1}}$) are coincide with positive modes of AO, NAO and to a smaller extent also with the P-NAO mode.
- the high BC event in 1986 (about $15\,\mathrm{ng\,g^{-1}}$) is only coincide with a high event in NAO. The AO and P-NAO mode is found in a neutral mode.
- the high BC event in 1991-1992 (about $8\,\mathrm{ng\,g^{-1}}$ to $9\,\mathrm{ng\,g^{-1}}$) is highly reflected in positive indices for AO and NAO (Figure 5.15).

Due to the long term reflection of BC concentrations with the winter AO, NAO and P-NAO modes, these indices can certainly be coincide with high BC event. The indices are related to the strengths of the Polar Vortex which reflected the cold dry air masses which dominates the Arctic winter atmosphere. During the above mentioned high BC event accumulation of particulate matter is assumed to dominated these winters, because of a damped mixing with more warm and humid air masses from the sub mid-latitude which enhance removal processes. Further, the above mentioned high BC event is associated with a enhance long-range transport of particulate matter into the Arctic. This is due to a higher fraction of polluted air masses from outside the Arctic meets the requirement of same low potential temperature as the Arctic air masses in order to be long-range transported into the Arctic.
It has to be noted, that this above analysis has not taken into account that the emission have changed over the period. The decrease in BC concentrations since 1985 is more likely associated with a decrease in emissions rather than a change in the AO, NAO and P-NAO mode.

5.4 Processing of OC EC analysed data

In order to investigate long-range transported particulate matter further, the *standard sized samples* from the *High Volume Sampler* (HVS) were analysed by the OC EC analyser for *Organic Carbon* (OC) and *Elemental Carbon* (OC) as described in section 4.3.3.
To determine the concentrations of OC and EC on the total sample filter a scaling factor, defined by the ratio of the area of the filter ($A_{filter} = \pi \cdot r^2 = 156.145\,\mathrm{cm}^2$) and the area of the *standard sized sample* (2.5 cm^2 or 1.5 cm^2) is introduced:

$$Factor = \frac{A_{filter}}{2.5\ cm^2} = 62.458 \quad or \quad \frac{A_{filter}}{1.5\ cm^2} = 104.096 \tag{5.5}$$

The total OC and EC concentrations was then determined by knowledge of the volume flow sucked through the filter (about 5000 $\mathrm{m}^3\,\mathrm{week}^{-1}$). The above parameters result in the following expression for the total OC and EC concentrations:

$$C_{OC\ or\ EC} \quad \left[\frac{\mu g}{m^3}\right] = \frac{Con_{OC/EC} \cdot\ Factor}{Volume} \tag{5.6}$$

Here $Con_{OC/EC}$ refers to the OC and EC concentrations found on the *standard sized sample* by the OC EC analyser.

The weekly *total carbon* (TC), OC and EC concentration dataset consisted of 91 measurements covering the period from July 2008 to February 2011, where a period from mid-March to mid-May in 2009 does not exist (marked with black arrow in figure 5.19). For the period from July 2008 to May 2009 data was available every second week which led to two week time resolution of OC and EC concentrations. From May 2009 to February 2011 data was available every week which led to one week time resolution of the OC and EC concentrations.

A first handling of the TC, OC and EC concentrations included the *quality control* of the dataset. This quality control was performed by analysing the dataset for any negative concentration[3] A negative concentration was found in week 47 in 2008 and this value was therefore determined as a outlier and not used further in this analysis.

The HVS is located in the old DMU hut which is situated inside the field station. Therefore it cannot be excluded that local waste combustion at Station Nord affect the OC and EC concentration on the filter samples from the HVS. To investigate this hypothesis an additional quality control was necessary. Thus, the distribution of TC, OC and EC concentrations were explored and the Grubb's test was performed on the concentrations in order to detected outliers.

[3]Negative concentration is assigned to mass leaving the filter which is not physically acceptable and probably more likely due to a handling errors of the sample.

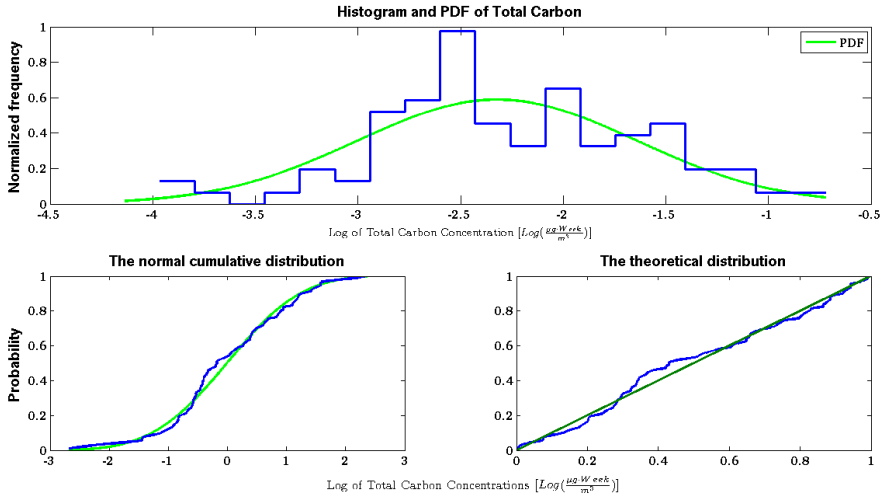

Figure 5.16: The distribution of the TC concentrations by the probability distribution (PDF), the cumulative distribution and the theoretical distribution.

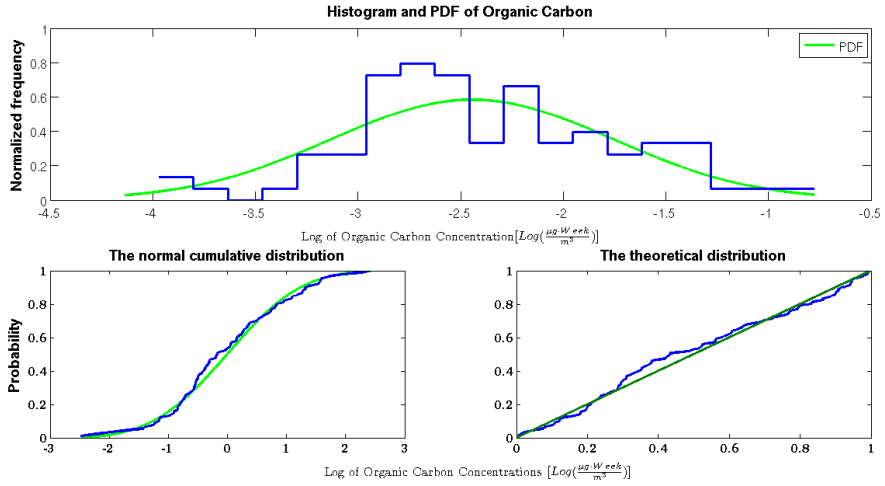

Figure 5.17: The distribution of the OC concentrations by the probability distribution (PDF), the cumulative distribution and the theoretical distribution.

In figure 5.16, 5.17 and 5.18 the *probability density function* (PDF), the normal cumulative distribution and the theoretical distribution of TC, OC and EC concentrations is visualized. Here, the concentrations are assumed log-normally distributed. In order to experiences how different distributions of datasets behaviour according to e.g. outliers, a small exercises was made. This exercises is described in appendix B.

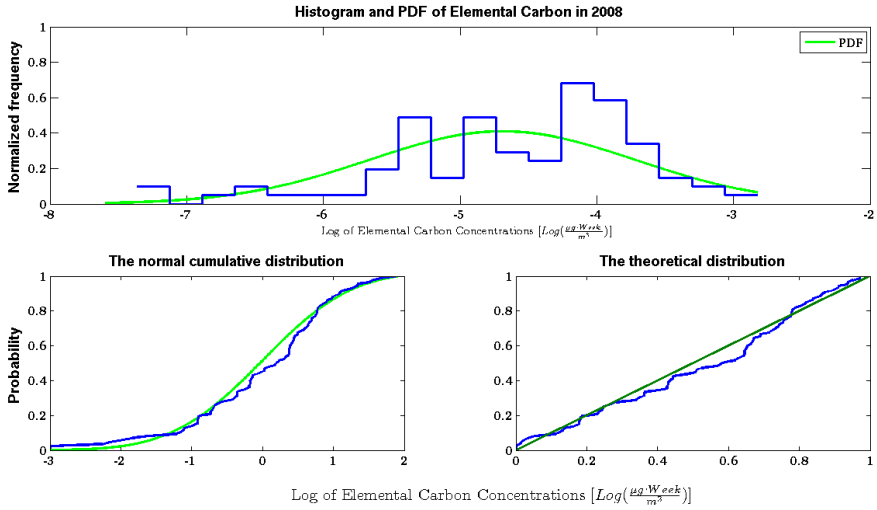

Figure 5.18: The distribution of the EC concentrations by the probability distribution (PDF), the cumulative distribution and the theoretical distribution.

In general, for the histogram of OC and EC concentrations high frequencies of certain concentrations do occur. This can perhaps be due to Arctic haze episodes, where the concentrations deviates from a normal long-range transported signal.
For OC concentrations (Figure 5.17) two high frequencies occur in the interval from -3 to -2.25, compared to the EC concentrations (Figure 5.18) where three high frequencies occur in the interval from -5.5 to -3.75. Besides that, it could also be a reflection of the low amount of measurements in the dataset, compared to the amount of measurements in the BC dataset from the PSAP.
The histogram of TC is highly reflecting the amount of OC, which is the largest contributor to the total amount of carbon and therefore this histogram is very similarly to the histogram of OC.
The normal cumulative distribution and the theoretical distribution for the OC and EC concentrations is closely following the theoretical and their deviates not significantly from the theoretical to be related to outliers. Therefore it was not expected to find any outliers in the TC, OC and EC dataset when the Grubb's test was performed on these datasets.

Table 5.3: The result from the Grubb's test on OC, EC and TC concentrations, where G denotes the critical value.

	TC	OC	EC
$G \gg$	3.34	3.343835	3.3318
G_{test} MAX	2.4194	2.4832	1.9133
G_{test} MIN	2.5440	2.3198	2.9889

The described Grubb's test in appendix B.2 is normally used to detect outliers in normal distributed datasets. The OC and EC concentrations are assumed to be log-normally distributed, therefore it can be argued that the Grubb's test cannot

be used to detect outliers in this dataset. Anyway the Grubb's test was determined to be the best known tool to investigate outliers in the dataset. The final result from the Grubb's test is listed in table 5.3 and this confirms clearly, that no outliers are found in the datasets. The critical value (G) is found about 3 and either the maximum or the minimum of the total, organic or elemental carbon concentrations are found close to the critical value.

5.4.1 Uncertainty of OC and EC measurements

The uncertainty of OC and EC concentrations from the OC EC analyser was estimated from the following formula:

$$\delta_{Relative\ uncertainty} = 0.05 \cdot \ Con_{OC\ or\ EC} \ + 0.2$$

Here the 0.05 value is the standard deviation from multiple analyses of a sugar solution, which is determined from another study. The value of 0.2 is related to the inevitable contamination of a handled blanc filter. This uncertainty from the OC EC analyser refers to OC and EC concentrations from the *standard sized samples*, therefore the related uncertainty of OC and EC concentration was scaled with the scaling *Factor* (Equation 5.5) so that the final uncertainty represents the uncertainty of OC and EC concentration of the entire filter from the weekly filter samples.

5.4.2 Final OC and EC concentrations

The final quality controlled total TC, OC and EC concentrations from the *standard sized samples* in the period from July 2008 to February 2011, analysed by the OC EC analyser, are presented as time series in figure 5.19. Here the EC concentration values are found between $0\,\mu g\,m^{-3}$ and $0.05\,\mu g\,m^{-3}$, where the TC and OC concentrations values are found in the size range of $0\,\mu g\,m^{-3}$ to $0.5\,\mu g\,m^{-3}$. The EC concentrations have an Arctic haze seasonal pattern with maximum concentrations (about $0.05\,\mu g\,m^{-3}$) in winter/early spring and minimum concentrations (about $0.01\,\mu g\,m^{-3}$) in summer. In figure 5.20 the seasonal pattern for EC concentrations is illustrated and this seasonal pattern in EC concentrations was also found for the BC concentrations which in general had a maximum in winter/early spring at about $0.06\,\mu g\,m^{-3}$.

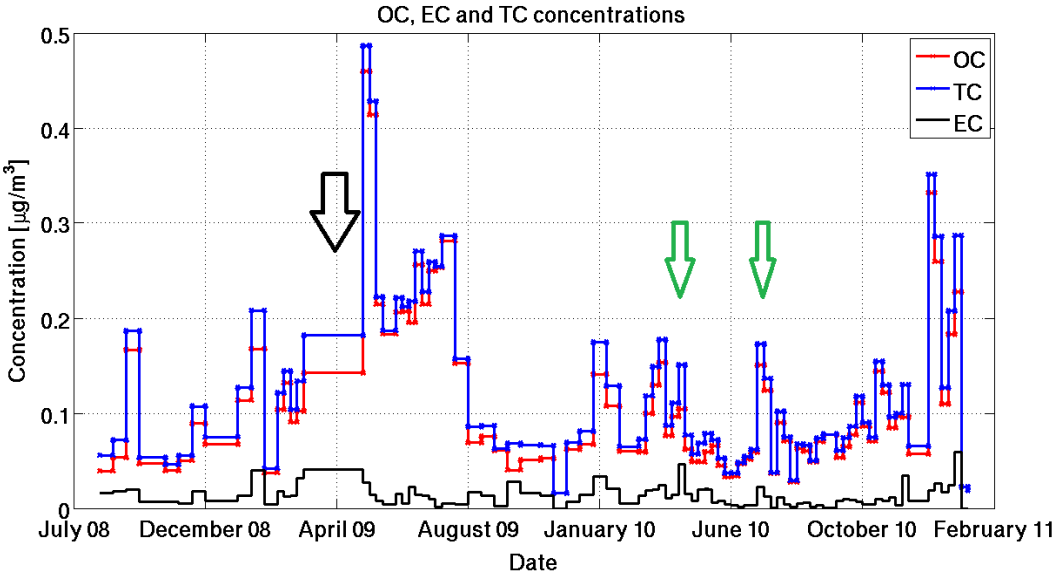

Figure 5.19: Weekly *Total Carbon* (TC), *Organic Carbon* (OC) and *Elemental Carbon* (EC) concentrations [$\mu g\,m^{-3}$] measured with the OC EC analyser in the time period of July 2008 to February 2011. Here, the black arrow indicates the period from mid March to mid May in 2009 where data do not exist. The green arrows indicate possible biomass events. An increasing level in EC occurs in winter and high levels of OC occur in winter as well as in summer.

The OC concentrations are found two to three times higher compared with EC concentrations. In general, high OC event occurs on irregular interval, but with a small tendency to higher OC concentrations in late spring/summer compared to winter. In addition, the highest OC event (about $0.45\,\mu g\,m^{-3}$) occurs in mid-May 2009.

Parameter / **Site**	**n**	**OC** [$\mu g\,m^{-3}$]	**EC** [$\mu g\,m^{-3}$]	**TC** [$\mu g\,m^{-3}$]	**EC/TC** [%]
Station Nord	88	0.11±0.08	0.01±0.01	0.12±0.08	11±8
Birkenes (Norway)	49	1.57±1.54	0.17±0.19	1.74±1.66	12±5
Virolahti (Finland)	51	2.08±1.86	0.36±0.25	2.44±2.04	16±6
Danish ambient	323	1.76	0.45	2.21	20

Table 5.4: The annual mean concentrations of EC, OC, and TC and the relative contribution of EC to TC from Station Nord, covering the time period from July 2008 to February 2011. Here n denotes the number of samples. The value from Norway and Finland is obtain from a one year (July 2002 to July 2003) study of 12 European rural background sites by Yttri et al. [2007]. The value from *Danish ambient* is from the semi-rural background concentrations at Lille Valby, Denmark, in 2010. Here the ± denotes the value of the sample standard deviation.

In table 5.4 the annual mean concentrations of EC, OC and TC in [$\mu g\,m^{-3}$] from Station Nord in the period from July 2008 to February 2011 are listed. Together with a similar one-year study in Europe in the period from July 2002 to July 2003

by Yttri et al. [2007] and the semi-rural background concentrations at Lille Valby, Denmark, in 2010. Similar studies in the Arctic region are not known.
In general, for all the stations, the amount of OC is higher than of EC, but the lowest concentration of both compounds is found at Station Nord. This is also reflected in the relative difference between OC and EC, which decreases at the sites close to the densely populated area in Europe. This could indicate a gradient in OC and EC concentrations between the Arctic sites and Europe. Furthermore, the OC concentrations are ten times higher than EC concentrations at Station Nord.

5.4.3 EC and BC comparison

According to similar chemical structure the EC and BC concentrations were expected to follow the same seasonal pattern with the same magnitude in concentrations. In figure 5.20, the EC and BC concentrations are shown for the period of July 2008 to February 2011. In this particular case the EC and BC concentrations are following the same seasonal pattern with the same order of magnitude in concentrations.

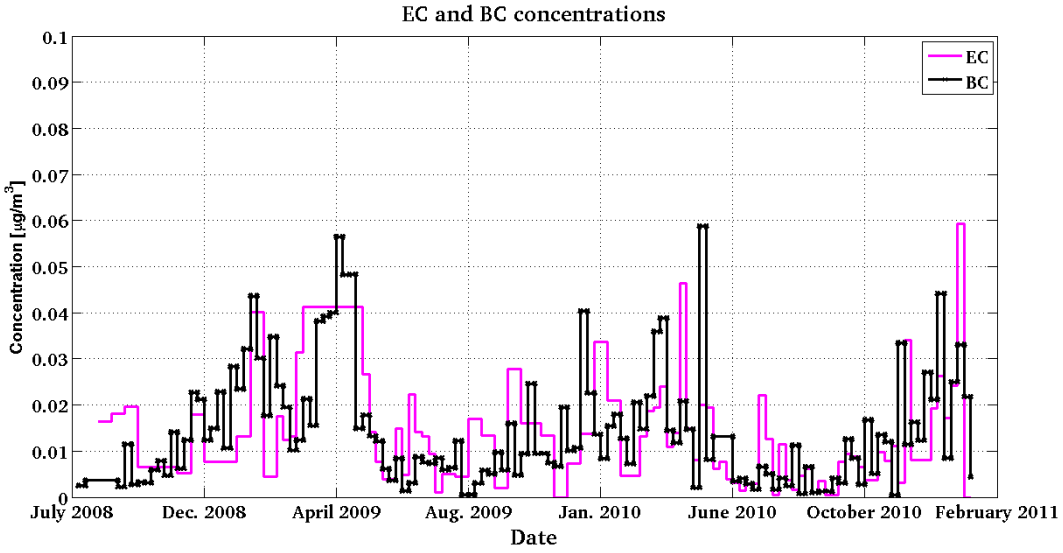

Figure 5.20: Weekly *elemental carbon* (EC) and *black carbon* (BC) concentrations [$\mu g\,m^{-3}$] measured with the OC EC analyser and the PSAP-instrument, respectively, in the time period of July 2008 to February 2011. Here, a good agreement between the concentrations of EC and BC is found.

5.4.4 EC/TC ratios

The EC and OC are formed under fossil fuel combustion processes or originate from natural emissions[4]. Depending on the emissions conditions of OC and EC (e.g. combustion engine or type of fuel) the ratio can either be associated with biomass burning or fossil fuel combustion. In general, for biomass burning the emission of OC is higher than for EC (low EC/TC ratio), while combustion is the

[4]Natural emission cover terpene emissions from plants and biomass burning in general.

primary source of EC, and results in a high content of EC compared to OC (high EC/TC ratio) for those emissions [Quinn et al., 2011; Yttri et al., 2007]. Furthermore, OC can also be formed from gasses which undergo transformation in the atmosphere and form *secondary organic aerosols* (SOA's). Therefore OC can also be a maker for SOA, although not a specific one (see also section 5.4.5).

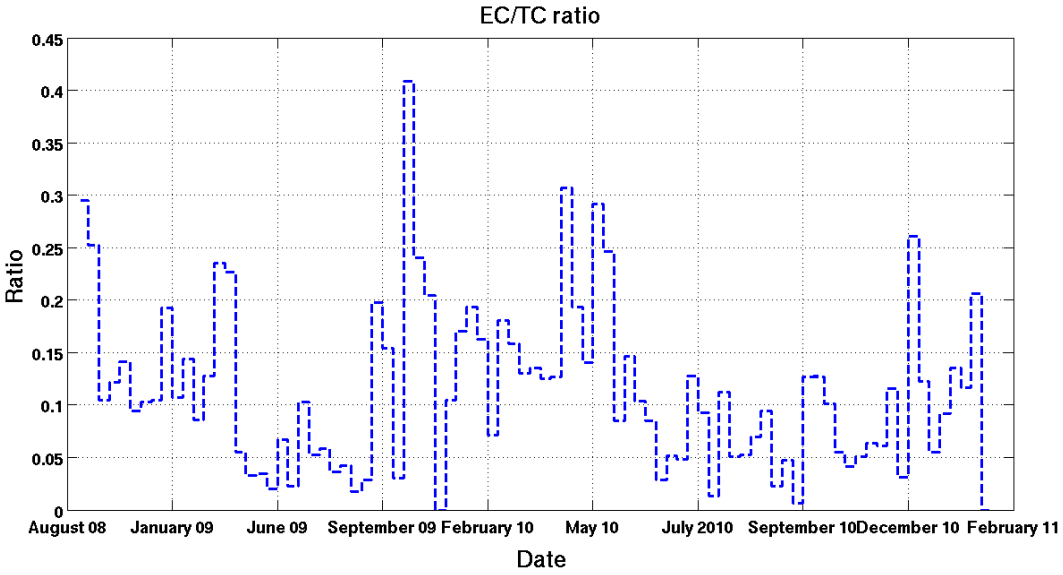

Figure 5.21: The relative contribution of EC to TC (EC/TC ratio) in the time period from August 2008 to February 2011. A high EC/TC ratio indicated high levels of EC, while a low EC/TC ratio indicate a low concentration of EC.

In figure 5.21, the relative contribution of EC to TC is shown for Station Nord in the time period from August 2008 to February 2011. A low OC/TC ratio is more pronounced in the summer than in winter. The EC/TC ratio is about 5 % to 10 % in summer and about 15 % to 40 % in winter, which highly reflects the seasonal pattern with high EC contents in winter. In addition, the low EC/TC ratio in February 2011 reflects more likely a wrong splitting point detected by the OC EC analyser rather than a low concentration value of EC.
If the annual mean EC/TC ratio at Station Nord (about 11 %) is considered together with the EC/TC ratio from the Scandinavian site listed in table 5.4, the ratio fall only slightly below the ratio reported from European rural background sites. This is in accordance with other studies which report that: "ageing of air masses tends to lower the EC/TC ratio of the aerosol due to oxidation and condensation of organic material" [Yttri et al., 2007].

The EC/TC ratios was calculated in order to investigates the sources at Station Nord, but it is difficult to determine at which ratio it can be distinguished between emission from biomass and emission from combustion processes. However, it is known that massive forest and peat fires occurred in Russia during July and August 2010 [Giere and Querol, 2010] and perhaps some of the low EC/TC ratio events in this period can be addressed to this forest and peat fires events in Russia.

5.4.5 Levoglucosan as a tracer for biomasses burning

Levoglucosan ($C_6H_{10}O_5$) is an organic compound formed from pyrolysis of cellulose and is a source-specific tracer of particulate matter emissions from biomasse burning [Engling et al., 2006; Simoneit et al., 1999].
The filter samples from the HVS at the old DMI hut at Station Nord were analysed for levoglucosan. This analysis is performed with *liquid chromatography-tandem mass spectrometry* (LC-MS-MS) with electrospray ionization in negative ionization mode. The LC-MS-MS method is based on the method published by Gambaro et al. [2008].

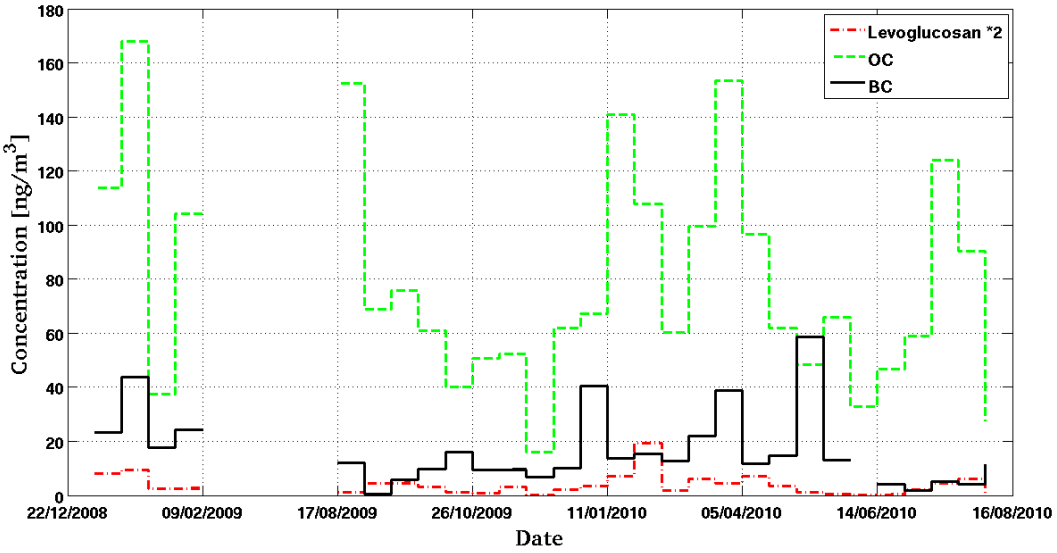

Figure 5.22: Concentrations of levoglucosan, OC and BC in [$\mathrm{ng\,m^{-3}}$] in the time period from January 2009 to August 2010. An event in April 2010 with high levels of levoglucosan, OC and BC could indicate a biomass burning episode.

In figure 5.22, the concentration of levoglucosan, OC and BC is shown for the overlapping time period from January 2009 to August 2010. Here the levoglucosan is multiplied by a factor of two in order to magnify the variation. The time resolution of levoglucosan is weekly and data exist every second week, but with a time period from mid-February 2009 to mid-August 2009 where no data are available. The levoglucosan concentrations vary in the size range of $0\,\mathrm{ng\,m^{-3}}$ to $9\,\mathrm{ng\,m^{-3}}$, where the highest event (about $9.7\,\mathrm{ng}^{-3}$) occurred in the last week of January 2010. In general, massive forest fires or wildfires are a late spring/summer-time phenomenon [AMAP 2006]. Therefore this high levoglucosan event is perhaps more likely a reflection of local waste combustion at the station. In order to investigate this, the Grubb's test was used to detect any outliers in the dataset of levoglucosan. The result is listed in table 5.5. Here, the test rejects the maximum levoglucosan concentration as an outlier, but rather founds the minimum levoglucosan concentrations as an outlier in the dataset. Therefore it can be concluded that high event of levoglucosan is not coincide with local waste combustion at Station Nord.

Table 5.5: The Grubb's test on levoglucosan concentrations, where G denotes the critical value and the number of samples is 30. Here the minimum concentrations of levoglucosan differ from the critical value.

	Levoglucosan
$G \gg$	2.9085
G_{test} MAX	1.3218
G_{test} MIN	3.7462

A signal of possible biomass plumes is expected to be reflected in high events of OC, levoglucosan and BC concentrations and such episode occurred in April 2010 (Figure 5.22). Here high concentrations of levoglucosan ($2\,\mathrm{ng\,m^{-3}}$ to $4\,\mathrm{ng\,m^{-3}}$) and OC ($100\,\mathrm{ng\,m^{-3}}$ to $150\,\mathrm{ng\,m^{-3}}$) are found and to some extent also in the BC concentrations (about $40\,\mathrm{ng\,m^{-3}}$).
The EC/TC ratios were specifically calculated for this month of April and found in the range of 12 % to 19 %. Therefore, any distinction between biomass and combustion sources can perhaps be found in this range of the EC/TC ratio. In addition, it is known that massive forest and peat fires occurred in July and August 2010 in Russia, which to some extent also is reflected in figure 5.22. Here the OC concentrations are high (about $60\,\mathrm{ng\,m^{-3}}$ to $120\,\mathrm{ng\,m^{-3}}$), but concentrations of BC and levoglucosan are not that pronounced. Therefore, these high OC concentrations are more likely associated with an event of a high amount of SOA which also can be related to biomass burning.

5.5 Specific absorption coefficient

A specific absorption coefficient ($\sigma_{specific}$) of $10\,\mathrm{m^2\,g^{-1}}$ was used to convert the absorption coefficient reported from the PSAP to BC concentration. This specific absorption coefficient of $10\,\mathrm{m^2\,g^{-1}}$ was found by Ström [2010] and gave a good agreement between EC measured by a thermo-optical method and BC measured by an optical method for the measuring station Zeppelin, Svalbard, Norway [Ström, 2010].
To investigate if this specific absorption coefficient can be applied at Station Nord a specific absorption coefficient was derived from the PSAP and from the EC concentrations obtained from the OC EC analyser. A scatter plot of the EC and the absorption coefficient (σ_{abs}) is shown in figure 5.23 and by using the relation in equation 4.11 the specific absorption coefficient was found as $7.82\,\mathrm{m^2\,g^{-1}}$.

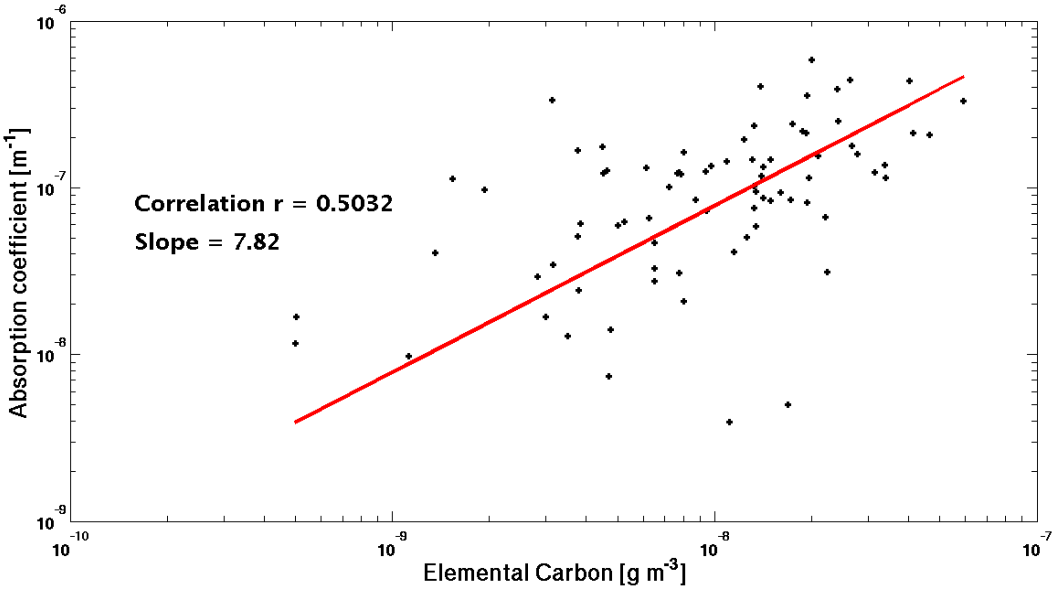

Figure 5.23: A scatter plot of EC concentrations and the light absorptions coefficient σ_{abs}. Here the slope is 7.82, which would be the value of the specific absorption coefficient at Station Nord.

In comparison, the specific absorption coefficient is found by Horvath [1993] in the range of $8\,m^2\,g^{-1}$ to $10\,m^2\,g^{-1}$ and Ström [2010] reported a specific absorption coefficient of $8.93\,m^2\,g^{-1}$ for the measuring station Zeppelin and found a good agreement by using a specific absorption coefficient of $10\,m^2\,g^{-1}$. In addition, Petzold et al. [1997] report variability in this coefficient, which seems to depend on regional variations of the predominant aerosol type. The observed variability ranges from $5\,m^2\,g^{-1}$ in remote areas to $14\,m^2\,g^{-1}$ at urban locations and to $20\,m^2\,g^{-1}$ at near-street measuring sites. According to this, it seems very plausible that the specific absorption coefficient at Station Nord is found as $7.82\,m^2\,g^{-1}$, because it is located in one of the most remote areas of the world and further north than the measuring station Zeppelin. Therefore, even if the correlation coefficient is not very good, this investigation confirms, that using the specific absorption coefficient of $10\,m^2\,g^{-1}$ is acceptable.

5.6 Results from the PIXE instrument

The filter samples from the FPS at Flygers hut were analysed for different atmospheric elements by either *Ion Chrometography* (IC) or *Proton Induced X-ray emission* (PIXE), where last-mentioned is described in chapter 4, section 4.3.4. The different elements are listed in table 5.6 together with the different analytical method, the annual mean concentration in $[ng\,m^{-3}]$ and the related uncertainty in [%].

Table 5.6: The chemical elements, their analytical method, annual mean concentration in [$\mathrm{ng\,m^{-3}}$] units for the period from March 2008 to December 2009 and their uncertainty in [%]. The OC, EC and TC are listed for the time period from July 2008 to February 2011 in [$\mathrm{ng\,m^{-3}}$] units and Levoglucosan are listed for the 28 samples from January 2009 to August 2010 in [$\mathrm{ng\,m^{-3}}$] units. Here following abbreviations denote: *Ion Chrometography* (IC), *Proton Induced X-ray emission* (PIXE) and *liquid chromatography-tandem mass spectrometry* (LC-MS-MS).

The Elements	**Method**	**Annual mean** [$\mathrm{ng\,m^{-3}}$]	**Uncertainty** [%]
Aluminum	PIXE	39.35	18
Silicon	PIXE	79.95	18
Sulfur	PIXE	181.52	18
Chlorine	PIXE	135.14	18
Potassium	PIXE	25.90	18
Calcium	PIXE	30.09	18
Titanium	PIXE	1.94	18
Vanadium	PIXE	0.11	18
Chromium	PIXE	0.08	18
Manganese	PIXE	0.47	18
Iron	PIXE	20.05	18
Nickel	PIXE	0.1	18
Copper	PIXE	0.1	18
Zinc	PIXE	1.23	18
Gallium	PIXE	0.021	18
Arsenic	PIXE	0.05	18
Selenium	PIXE	0.044	18
Filterable Bromine	PIXE	1.49	18
Rubidium	PIXE	0.085	18
Strontium	PIXE	0.35	18
Zirconium	PIXE	0.07	18
Lead	PIXE	0.52	18
Levoglucosan	LC-MS-MS	1.96	
Sulfur dioxide	IC	80.55	20
Sulfate	IC	178.55	20
SO_x, $(SO_4^{2-} + SO_2)$	IC	259.11	20
Organic Carbon	OC EC analyser	11	-
Elemental Carbon	OC EC analyser	1	-
Total Carbon	OC EC analyser	12	-

To investigate the measured elements at Station Nord (Listed in table 5.6) together with the black carbon concentrations derived from the PSAP, the correlation between BC and the elements was calculated (Table 5.7) for the period from March 2008 to February 2010.

This investigation was performed in order to obtain an understanding of which elements there might be emitted together with BC and thereby identify possible

particle sources for BC in the Arctic region. The correlation coefficient r is defined as:

$$r = \frac{< \tilde{x} \cdot \tilde{y} >}{\sqrt{< \tilde{x^2} > \cdot < \tilde{y^2} >}} \tag{5.7}$$

Here the x and y are the elements under investigation and $\tilde{x} = x - \langle x \rangle$. In addition, the hypothesis of no correlation was tested by the P-values. Each P-value in table 5.7 is the probability of getting a correlation as large as the observed value by random chance, when the true correlation is zero. If $P(x, y)$ is small, less than 0.05, then the correlation $r(x, y)$ is significant at the 95% confidence level. The calculation was performed in Matlab and the result obtained is listed in table 5.7.

Table 5.7: The significant correlation coefficients between different elements and black carbon for the period of March 2008 to February 2011. The amount of data points for the correlation is 92 for the elements, for OC and EC 46 and for levoglucosan 29.

The Elements	**Symbol**	**Correlation coefficient** r	P**-value** $[10^{-2}]$
Aluminum	(Al)	0.4368	0.00
Silicon	(Si)	0.2863	0.57
Sulfur	(S)	**0.7836**	0.00
Chlorine	(cl)	-0.0342	74.60
Potassium	(K)	0.2275	2.92
Calcium	(Ca)	0.4186	0.00
Titanium	(Ti)	0.3296	0.13
Vanadium	(V)	0.2324	2.58
Chromium	(Cr)	0.4011	0.01
Manganese	(Mn)	**0.6797**	0.00
Iron	(Fe)	0.3928	0.01
Nickel	(Ni)	0.4351	0.00
Copper	(Cu)	0.4515	0.00
Zinc	(Zn)	0.4266	0.00
Gallium	(Ga)	0.3099	0.26
Arsenic	(As)	0.5668	0.00
Selenium	(Se)	0.5829	0.00
Filterable Bromine	(Br)	**0.6960**	0.00
Rubidium	(Rb)	0.5864	0.00
Strontium	(Sr)	0.4013	0.01
Zirconium	(Zr)	0.2158	3.88
Lead	(Pb)	**0.6360**	0.00
Levoglucosan	$(C_6H_{10}O_5)$	0.1327	49.24
Sulfur dioxide	(SO_2)	0.2009	7.03
Sulfate	(SO_4^{2-})	**0.8803**	0.00
SO_x	$(SO_4^{2-} + SO_2)$	**0.7232**	0.00
Organic Carbon	(OC)	0.3637	1.30
Elemental Carbon	(EC)	**0.5232**	0.02
Total Carbon		0.4258	0.52

A significant correlation is found between BC and the elements of *manganese* (Mn) (0.6797) and *lead* (Pb) (0.6360). Those two elements are typical prominent anthropogenic sources from combustion processes at Station Nord [Heidam et al., 2004, 1999]. Therefore BC concentrations at Station Nord can be associated with combustion sources. Besides that, an additional anthropogenic source is metal, where specifically *Copper* (Cu) and *Nickel* (Ni) are ascribed to have high emissions rates from this source. Here, the significant correlation between BC and metallic elements; (Ni) (0.4351); (Cu) (0.4515) and *Zinc* (Zn) (0.4266) is not very pronounced. Therefore, it is difficult to identify metals and BC as emitted by the same sources only based on this correlation.

Another significant correlation occurs between BC concentrations and *Sulfur* concentrations (S) (0.7836), but this elements S is difficult to assign to a single source. In addition, it can be seen that the related sulphate ion (SO_4^{2-}) (0.8803) correlates better with BC than pure sulfur. Sulphate is typically associated with combustion processes as well as BC. Therefore, the correlation between sulphate and BC was investigated further.

5.6.1 Sulphate results

The filter samples from the FPS were returned to the laboratory at NERI to be analysed for atmospheric pollutants such as SO_4^{2-} and SO_2 by *Ion Chromatography* (IC), which is a method that separates and determines ions concentrations [Fritz, 1987].

In figure 5.24, the measurements of SO_4^{2-}, SO_2 and BC concentrations in [$\mu g\,m^{-3}$] are shown for the overlapping time period from March 2008 to December 2009. The SO_2 has a maximum winter concentration (about $0.8\,\mu g\,m^{-3}$) and a minimum summer concentration (below $0.1\,\mu g\,m^{-3}$). The SO_4^{2-} concentration has a maximum winter concentration in the range of $0.3\,\mu g\,m^{-3}$ to $0.8\,\mu g\,m^{-3}$ and a minimum summer concentration (below $0.1\,\mu g\,m^{-3}$). In general, the concentrations is found with the same seasonal variation as the BC concentrations, but SO_2 seems to achieve its maximum value in the late winter and then rapidly declines. This is highly associated with the amount of solar radiation, which is necessary for OH radical formation by photolysis to form sulphate. Therefore, the oxidation rate of sulphur dioxide to sulphate depends on the time of the year.

This seasonal pattern in SO_2 and SO_4^{2-} has been observed at Station Nord since the early 1990's [Heidam et al., 2004]. From the measured concentrations in the time period of 1989 to 2000, the SO_2 appears with winter concentrations about $0.8\,\mu g\,m^{-3}$ to $1.8\,\mu g\,m^{-3}$ and the SO_4^{2-} has a winter concentration of about $0.75\,\mu g\,m^{-3}$ to $1\,\mu g\,m^{-3}$. In comparison with this study (Figure 5.24) the SO_2 and SO_4^{2-} are found with the same size in winter concentration as the time period of 1989 to 2000.
Furthermore, BC particles can be aged by coagulation with more soluble aerosols such as sulphate or by condensation of *sulfuric acid* (H_2SO_4). Sulphate is also emitted from combustion processes, but also a chemical compound that dominates the

marine atmosphere. Air masses which pass Station Nord have most likely passed a sea area or ice covered sea before passage of Station Nord. Therefore, the trend of BC following sulphate is probably related to the ageing processes of carbonaceous aerosol particles.

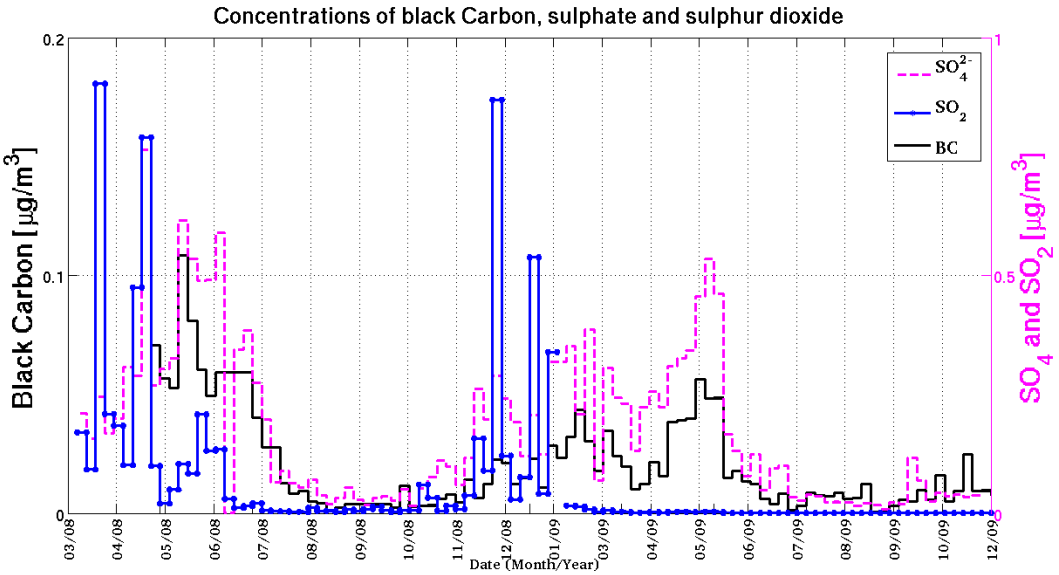

Figure 5.24: Weekly SO_4^{2-}, SO_2 and BC concentrations in [$\mu g\,m^{-3}$] from March 2008 to December 2010. Here BC concentrations follows the sulphate concentrations with the same seasonal pattern.

5.7 COPREM results

The seasonal distribution of BC concentrations at Station Nord was found to be very uneven with almost no BC pollution in the summer and a high concentration in winter. The same seasonal pattern was found for sulphate as well as EC. However, a large number of elements which are listed in table 5.7 are reported from Station Nord and some of them are assigned to the Arctic haze pattern [Heidam et al., 2004]. This results in a large dataset which can be used to link the observation at Station Nord with emissions from different sources outside the Arctic. Therefore, an investigation of sources for different elements was performed with the *Constrained Physical Receptor Model* (COPREM) described in section 4.5.

5.7.1 First COPREM results

The measured concentrations at Station Nord were divided into 4 main sources for the Arctic region: a crustal source (Soil), a marine source (Sea), an anthropogenic source associated with combustion processes (Combustion) and an additional anthropogenic source associated with metal industrial activity (Metals). These profiles are described further in section 2.6 and the profile matrix and form matrix used in this analysis can be found in section 4.5.

The strengths of the sources were determined in COPREM by minimizing the statistical parameter the *Error* E. During processing of the model the E-value was improved by a factor of 1.3, since E was improved by E = 34 498 − > 26 433 with 1708 degrees of freedom. The final presented results ended with a squared standard deviation of 1.64 of all the calculated source strengths.

In figure 5.25, 5.26 and 5.27 the most interesting elemental source apportionment obtained from COPREM is shown for the time period from March 2008 to December 2009. The four main sources are indicated with the following colours: Soil (Green), Sea (Blue), Combustion (Black) and Metal Industry (Yellow). The elemental weekly concentrations are denoted with white circles and the related uncertainty is marked with error bars.

According to Station Nord the main contributor to BC concentrations is found from the anthropogenic sources, combustion and metal industry (Figure 5.25a). The main part in winter is from combustion, but in late spring the emission from metal industry seems to dominate. Last-mentioned is the main pattern in late spring 2008 and 2009. In the summertime the contribution from both anthropogenic sources seems to be equal, but in general for this season the BC concentrations are quite small as discussed in section 5.2.2.

The main contributor to sulphate concentrations is found from the anthropogenic sources, combustion and metal industry, with a small contribution from marine sources (Figure 5.25b). The anthropogenic sources are found with the same pattern as BC concentrations, where the main part in winter is from combustion and in late spring the metal source is dominating. The marine source seems to contribute in late autumn and winter, which probably can be related to the autumn and winter storms at sea. In addition, the sulphur concentrations are found with the same trends in sources as sulphate (Figure 5.25e) and both have a high correlation with the BC concentration 0.7836 and 0.8803, respectively. This gives an indication that these chemical compounds either originates from the same source or reflecting ageing processes of BC.

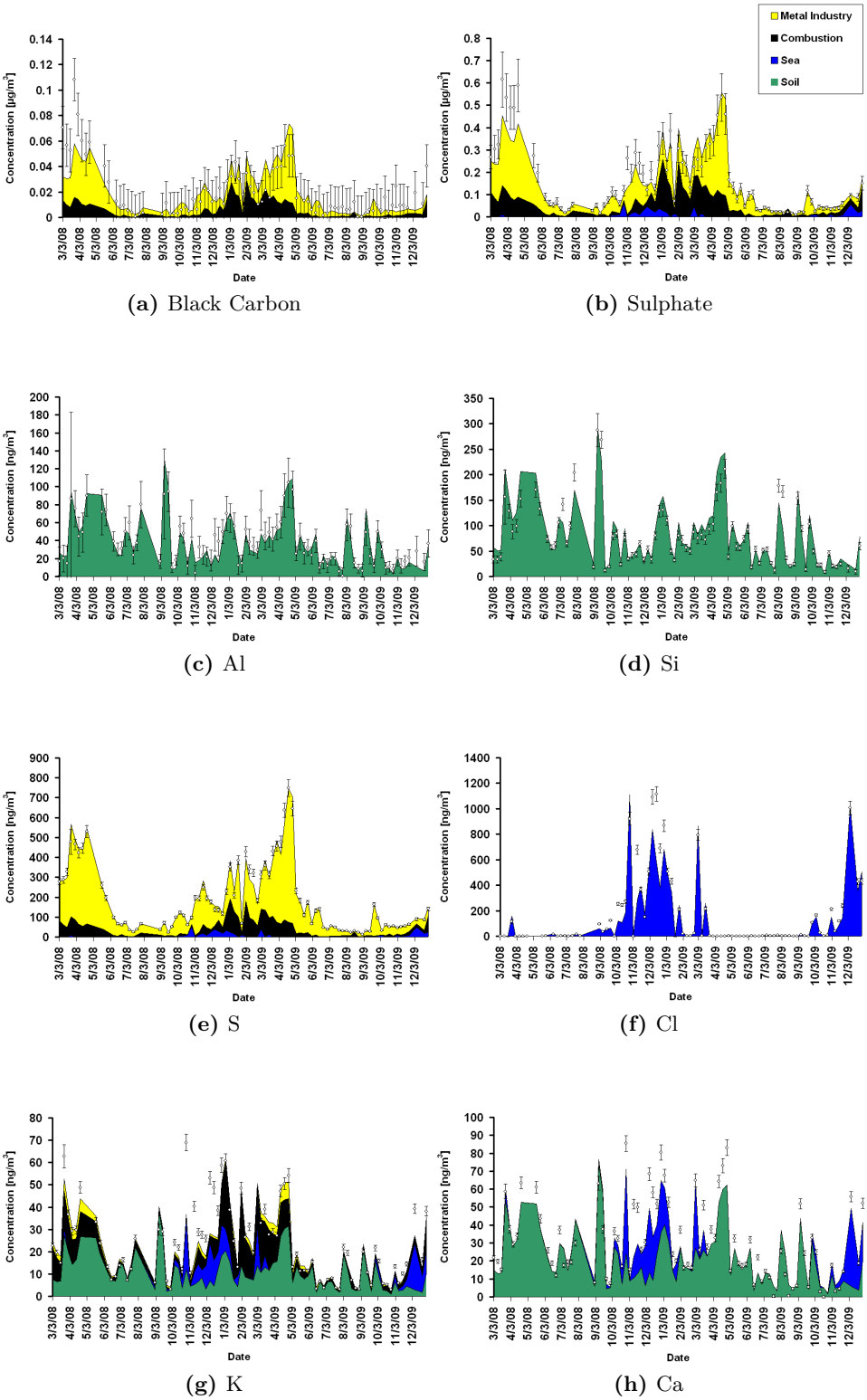

(a) Black Carbon **(b)** Sulphate

(c) Al **(d)** Si

(e) S **(f)** Cl

(g) K **(h)** Ca

Figure 5.25: The variation in elemental concentrations [$\mathrm{ng\,m^{-3}}$] and source apportionments according to the four main source from COPREM for the time period March 2008 to December 2009. Here, BC and sulphate concentrations are shown in [$\mu\mathrm{g\,m^{-3}}$]. The colours indicate the following sources: Soil (Green), Sea (Blue), Combustion (Black) and Metal industry (Yellow).

The prominent anthropogenic source combustion is dominating the source apportionment of Zn (Figure 5.26g), Ga (Figure 5.26h) and Pb (Figure 5.27b). This combustion source has its maximum contribution in winter and minimum in summer, which corresponds to the typical Arctic haze cycle. In general, COPREM obtain a adequate source apportionment for those compounds compared to measurements, but for the summer and autumn 2009 it underestimates the elements of Zn and Ga. This might be an indication of changes in sources. Furthermore, the elements of Ni, Cu, Mn, V and K are to some extent also associated with the combustion source. Especially Mn is associated with combustion processes in winter.

The additional anthropogenic source associated with metal industrial activity is dominating the source apportionment of Cu (Figure 5.26f) and Ni (Figure 5.26e) and to some extent K (Figure 5.25g) and Fe (Figure 5.26d). The metal source has the typical Arctic haze cycle with a maximum in winter and during this time of the year the metal source is contributing to elements such as K and Fe. In general, COPREM underestimates elements of Cu and Ni, especially Cu. These elements are highly associated with metal industry activity and in Heidam et al. [2004] these elements are found with a source strength almost equally with the measured. Therefore is the underestimated source apportionment found in this study an expression for a inconclusive source profile. Furthermore, the metallic elements Fe, Ni and Cu are found with an annual correlation with BC concentrations of 0.3928, 0.4351 and 0.4515, respectively. This correlation is significant and therefore it is unlikely than the annual prominent anthropogenic source for BC concentrations at Station Nord should be the metal industry. The metal industry is rather a source of BC concentrations at Station Nord in the winter and in the spring season, especially in the winter of 2009/2010 due to the strong correlation between BC concentration and these elements (Table 5.8).

Elements	Winter/Spring	Correlation coefficient r	P -value	Number n
Cu	2008/2009	0.5386	0.0045	26
Ni	2008/2009	0.4966	0.0048	26
Zn	2008/2009	0.3493	0.0803	26
Cu	2009/2010	**0.5841**	0.0283	14
Ni	2009/2010	**0.8252**	0.0003	14
Zn	2009/2010	0.5164	0.0587	14

Table 5.8: The elements associated with metal industrial activity and the correlation coefficient between selected elements and black carbon concentrations for the winter/spring period of November 2008 to April 2009 and the period of November 2009 to February 2010, the associated P-value and the number of measurements. The strongest correlations occur in winter/spring 2009/2010.

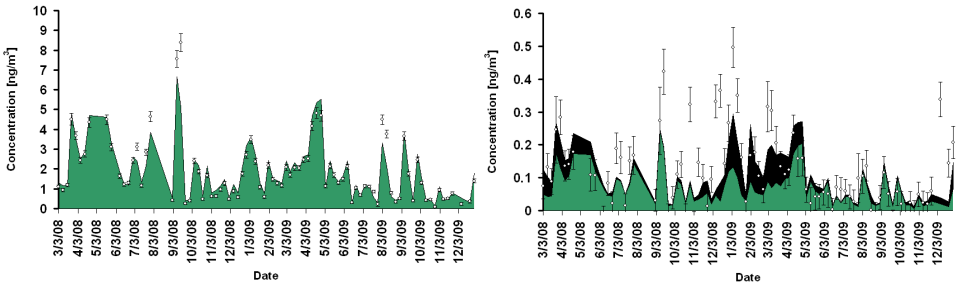

(a) Ti

(b) V

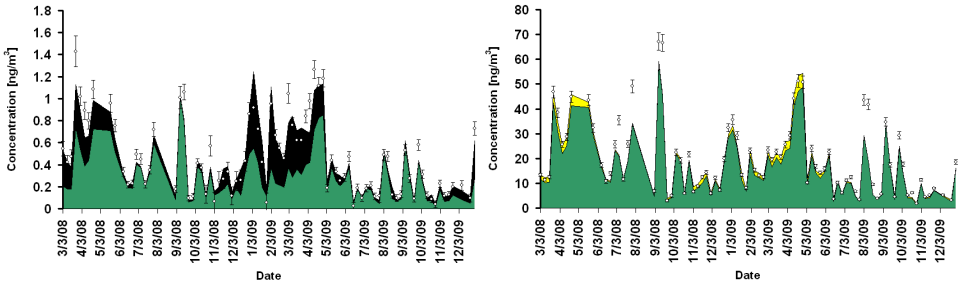

(c) Mn

(d) Fe

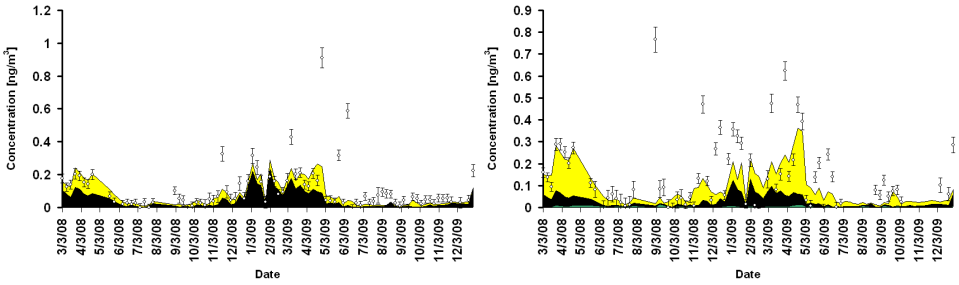

(e) Ni

(f) Cu

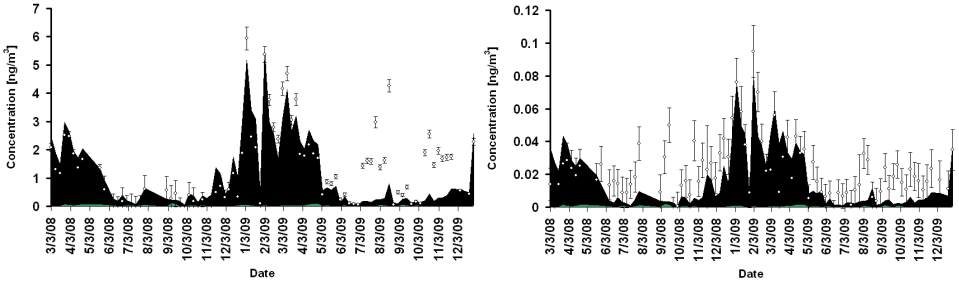

(g) Zn

(h) Ga

Figure 5.26: The variation in elemental concentrations [$\mathrm{ng\,m^{-3}}$] and source apportionments according to the four main sources from COPREM for the time period March 2008 to December 2009. The colours indicate the following sources: Soil (Green), Sea (Blue), Combustion (Black) and Metal industry (Yellow).

The remaining elements are associated with natural sources. The soil sources are associated with crustal elements e.g. Al (Figure 5.25c), Si (Figure 5.25d), Ti (Figure 5.26a) and Fe (Figure 5.26d). In general, these elements are not coinciding with seasonal pattern which was found for the metallic elements, but some peaks occur during the spring and late summer. This might be addressed to soil or dust aerosols which are released to the atmosphere during strong wind conditions e.g. during spring and autumn storms. Furthermore, this soil sources are also contributing to the source apportionment of Mn, Ca V and K. In general, for these elements only a small part of the concentration is associated with anthropogenic origins. However, K deviates from this pattern with a large contribution from anthropogenic sources in winter and spring (Figure 5.25g). Furthermore, *Potassium* (K) is related to plant activity, because K is an essential nutrient for plants to grow [Yao et al., 2010] and thereby a tracer for biomass burning [Jacob K. Nøjgaard, 2011, Private communication]. Therefore can the contribution from combustion in the K source apportionment in spring might be addressed to biomass burning. In addition, in April 2010 a signal of biomass burning was found from the tracers of Levoglucosan, BC and OC. Therefore it is likely, that this period at Station Nord is influenced by biomass burning sources. In order to investigate this further an additional source profile had to be added to the COPREM model.

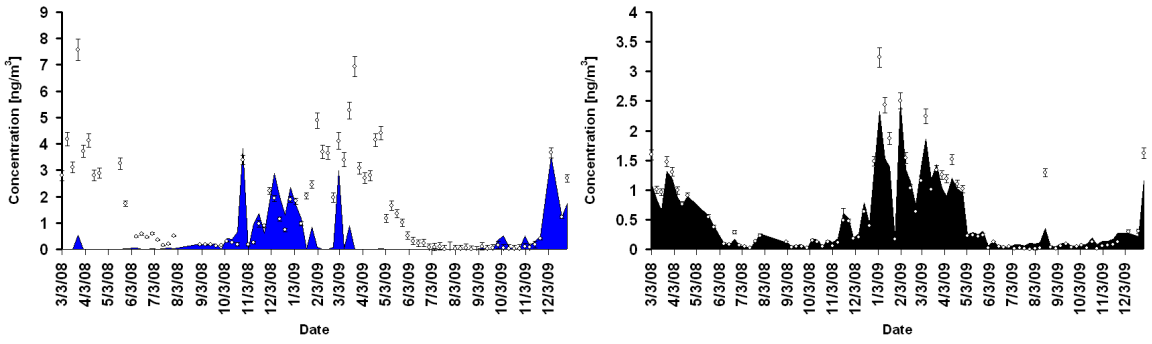

(a) Br **(b)** Pb

Figure 5.27: The variation in filterable Bromine and Lead concentrations [$\mathrm{ng\,m^{-3}}$] and source apportionments according to the four main source from COPREM for the time period March 2008 to December 2009. The colours indicate following sources: Soil (Green), Sea (Blue), Combustion (Black) and Metal industry (Yellow).

The sea source is associated with elements from marine activity (sea spray aerosols) e.g. Ca (Figure 5.25h), K (Figure 5.25g) and Cl (Figure 5.25f). These elements seems to have a strong winter maximum which is highly related to the autumn and winter storms at sea. Filterable Br (Figure 5.27a) is also associated with the sea source. The source apportionment found for Br is very poor and the Br concentrations are in general underestimated as illustrated in figure 5.27a. Therefore is Br also the largest contributor to the minimizing by the total statistical parameter E in COPREM. A reason for the poor Br source apportionment could be that there is a lot of chemistry involved with Br in the atmosphere. In addition, COPREM operates with sources that are constant and thereby ignoring the chemical pro-

cesses during the transport to Station Nord. Furthermore, filterable Br is found with a seasonal variations in Skov et al. [2004] and also with a strong correlation with SO_4^{2-} [Henrik Skov, 2011, Private communication]. Further, filterable Br is assumed to be released to the troposphere during crack and refreeze of the ice cover ocean [Henrik Skov, 2011, Private communication]. Therefore, to improve the Br source apportionment a new source assignet to natural source could be inplimented in COPREM.

In comparison, the result obtained by Heidam et al. [2004] and the above found source apportionment seems to be in a good agreement. Only Cu seems to have a better source strength compared to the measured concentrations in Heidam et al. [2004] than in this source apportionment. This is most likely an expression of the element variability at Station Nord. If the full mass concentration from all the different elements at Station Nord would be known then this would improve the source apportionment for the different elements considerably.

5.7.2 Preliminary COPREM results

A further COPREM analysis was obtained in order to investigate the amount of *Secondary Organic Aerosols* (SOA) at Station Nord. SOA is highly associated with biomass burning due to SOA formation from the oxidation of volatile or semi-volatile organic compounds released to the atmosphere from burning of biomass [Andreae and Merlet, 2001; Iinuma et al., 2010].

In figure 5.28 the most important elements for the source apportionment investigations are shown for the time period of December 2009 to February 2010. Here, the five main sources are indicated with the following colours: Soil (Green), Sea (Blue), Combustion (Black), Metal Industry (Yellow) and SOA (Pink). The elemental weekly concentrations are denoted with white circles and the related uncertainty is marked with error bars.

In figure 5.28a, it is illustrated that the large amount of OC is related to SOA and the large concentration of OC is found in the spring and summer season. However, a small amount is found to be related to metallic sources during the spring season. The source apportionment for OC is rather a primary result than a final result. The SOA formation is still related to a lot of research questions and in order to obtain a satisfactory source apportionment tracers related to SOA formation have to be investigated further. Then, these tracers can be used as markers of source strength in the source profile in COPREM.
In this analysis of SOA in COPREM an almost similar form and source profile as in the first COPREM investigation was used. Here, the filterable Br was removed from the dataset, because a lot of chemistry is expected to be involved with Br. Further, in order to improve the source apportionment, sulphate was added with sulphur dioxide (SOx=SO_4^{2-} + SO_2), because SO_2 will eventually be oxidized to SO_4^{2-} during transport.
The result obtain according to this COPREM investigation is shown for OC (Figure 5.28a), BC (Figure 5.28b) and SO_x (Figure 5.28c). Here, the minimized E- value

was found to 7142 with 768 dof and a related squared standard deviation of 1.05 of all the calculated source strengths.
In general, a similar pattern is found for the elements source apportionments. Here, illustrated with the source apportionment for Black Carbon (Figure 5.28b) and SO_x (Figure 5.28c), where again the main contributors is found from the anthropogenic sources, combustion and metal industry.

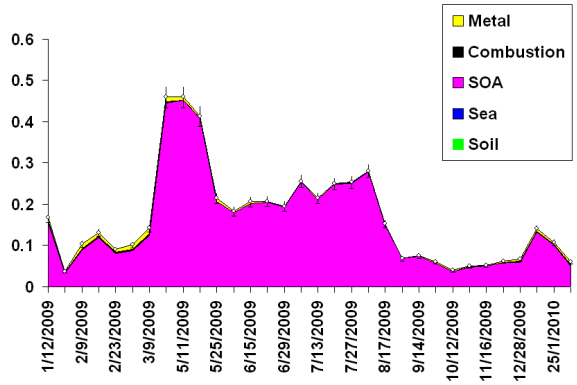

(a) Organic Carbon

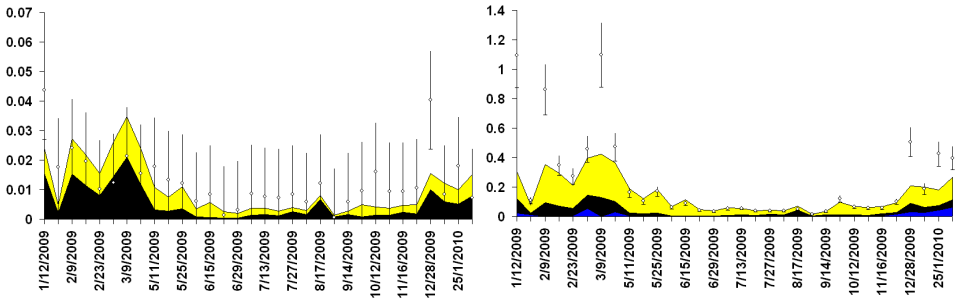

(b) Black Carbon

(c) SOx ($SO_4^{2-} + SO_2$)

Figure 5.28: The variation in elemental concentrations [$\mu g\,m^{-3}$] and source apportionments according to the results obtained from COPREM in the time period December 2009 to February 2010. The colours indicate the following sources: Soil (Green), Sea (Blue), Combustion (Black), Metals industry (Yellow) and *Secondary Organic Aerosols* (SOA) (Pink).

Chapter 6

Conclusion from the present study

The characteristics of particulate Arctic air pollution with special attention to Black Carbon and its sources at the high Arctic Station Nord was investigated throughout this project by three main methods. The meteorological conditions were analysed by considering the 500 mb geopotential height-contours in the northern hemisphere and by the indices of AO, NAO and P-NAO mode from autumn 2007 to spring 2011. This analysis was done in order to investigate the strength of the Polar Vortex in the Arctic region. In order to investigate the characteristics of BC concentrations, the measurements from the PSAP at Station Nord were analysed in the time period from March 2008 to April 2011. In addition, the source for pollutants at Station Nord and their source apportionment were investigated using the COPREM model.

Throughout this project following conclusion were found:

- The Arctic winter atmosphere is characterised by strong radiational cooling which enhance radiation inversions (very stable stratification of the lower troposphere) and thereby reduce turbulent exchange. Further, high positive modes of AO and NAO was coincide with a strong Polar Vortex, which is associated with a cold and dry air mass over the pole which form itself into a cyclonic vortex (Polar Vortex).
- The Arctic winter atmosphere in the winter period of 2007/2008 is found to be the most favourable for transport of polluted air masses into the Arctic and for accumulation of particulate matter in the Arctic troposphere. This is due to the high positive modes of AO and NAO which reflected a very stable atmosphere which enhance the accumulation of particulate matter. Further, the high positive mode of AO and NAO reflects a strong Polar Vortex which enhance the transport of polluted air masses from receptor site into the Arctic due to the same potential temperature as in the Arctic.
- The winter of 2008/2009, 2009/2010 and 2010/2011 is found with a very unstable modes of the indices of AO, NAO and P-NAO which reflected a weak Polar Vortex. This is associated with more meridional winds which

allow cold dry air to move southward and be replaced by warm and moist air masses, especially in late autumn and early winter 2008 and 2010. This type of air masses enhances the removal of particulate matter by deposition and limits the transport of polluted air masses into the Arctic.

- A seasonal variation is found in the BC concentrations with the high concentrations in winter and low concentration in summer. This is consistent with the Arctic haze cycles as well as BC concentrations reported from the measuring station of Alert, Canada and Zeppelin, Spitsbergen, Norway. Generally for the four-year period, there is a decrease in winter BC concentrations at Station Nord. The winter of 2007/2008 has maximum BC concentrations of $110\,\mathrm{ng\,m^{-3}}$, where the winter BC concentrations in 2008/2009 is found in range of $20\,\mathrm{ng\,m^{-3}}$ to $60\,\mathrm{ng\,m^{-3}}$, in winter 2009/2010 is found in range of $20\,\mathrm{ng\,m^{-3}}$ to $40\,\mathrm{ng\,m^{-3}}$ and in winter 2010/2011 is found in range of $15\,\mathrm{ng\,m^{-3}}$ to $50\,\mathrm{ng\,m^{-3}}$. This decrease of BC concentrations in summer and during the four-year period is found coincide with unstable modes of the indices AO, NAO and to some extent also P-NAO.

- An event of high BC concentrations was found in March 2008 (about $110\,\mathrm{ng\,m^{-3}}$) which is the same period with high positive modes of AO and NAO and a strong Polar Vortex was presented in the Arctic winter atmosphere. Therefore a strong Polar Vortex is highly associated with high pollution event at Station Nord. This is to some extent also reflected in the BC concentrations from the ice core from Flade Isblink and the indices of AO and NAO for the time period of 1950 to 2000.

- The uncertainty related to BC was assumed to have a contribution from the voltage signal, the filter area and the volume flow and is estimated to $0.0166\,\mathrm{g\,m^{-3}}$.

- The specific absorption coefficient needed for converting the light absorption coefficient into BC concentration is found to $7.82\,\mathrm{m^2\,g^{-1}}$ at Station Nord.

- A high correlation was found between annual BC concentrations and sulphate (0.8803) and manganese (0.6797), which is associated with combustion processes. This indicated that BC concentrations are assigned to combustion processes. In addition, high correlation was found in the winter/early spring of 2008 and 2009 between BC concentrations and the metallic elements of copper, nickel and zinc. This indicated that metal industry is a source for BC concentrations at Station Nord in winter/early spring.

- BC concentrations was found with a very similar seasonal pattern as sulphate which is assumed to be related to coagulation and ageing processes with the more soluble aerosols of sulphate.

- From the COPREM result, anthropogenic sources seems to contribute with the largest fractions in winter and early spring, where soil sources seem to have a more varying contribution pattern, but with some peaks in spring and late summer. The marine source contribute with large fractions in late autumn and winter most likely due to autumn and winter storms at sea.

- The main contributor to BC concentrations according to COPREM is found from anthropogenic sources, combustion and metal industry. Further, the BC source apportionment seems to have a larger contribution from metal industry in spring. This was consistent in the winter of 2007/2008 and 2008/2009. The same anthropogenic contributor was found for sulphate concentrations, but also with small contributions from marine sources in late autumn and winter.
- A signal of biomass plume at Station Nord is found in April 2010 reflected in concentration of levoglucosan ($2\,\mathrm{ng\,m^{-3}}$ to $4\,\mathrm{ng\,m^{-3}}$), concentration of organic carbon ($100\,\mathrm{ng\,m^{-3}}$ to $150\,\mathrm{ng\,m^{-3}}$) and concentration of BC ($40\,\mathrm{ng\,m^{-3}}$). Therefore it is very likely that biomass burning is a stampe source of particulate matter at Station Nord.
- The specific EC to TC ratio was calculated for the episode of biomass plume (April 2010) at Station Nord and found in the size range of 12% to 19%. Therefore, any distinction between biomass and combustion sources can perhaps be found in this sites range of the EC/TC ratio.

If the main pattern for the Arctic winter atmosphere continues to be a weak Polar Vortex, it might be the case, that events of high BC concentrations will not be that persistent in the future. A winter situations with a weak Polar Vortex will enhance the removal process of particulate matter from the receptor site before reaching Station Nord and accumulation of BC in the troposphere will not have the same favourably conditions. This leaves the Arctic winter pollution in 2007/2008 quite extraordinary. However, Arctic haze is still assumed to be a widespread phenomenon in the Arctic dominated by anthropogenic sources as well as natural emission and biomass plumes. Thereby contributing to the radiative forcing in the Arctic enforced by Arctic haze aerosols.

Chapter 7

Perspectives for the future

In this chapter the main conclusions will be perspective into the future and the adequate knowledge which is needed in order to improve accurate modeling of the radiative forcing due to Arctic haze aerosols would be identified.

More research was found to be needed to improve our knowledge of particulate matter related to biomass burning and the transformation of those organic processes into SOA. This is important in order to model more reliable results of the source apportionment of SOA in COPREM. In addition, an additional investigation of tracers related to biomass burning besides levoglucosan could improve the source apportionment of BC in the Arctic and might give an estimate of the contribution from biomass sources at Station Nord. Furthermore, an improvement of COPREM would might occur if the total mass concentrations would be known at Station Nord.

In order to improve our knowledge of source-receptor relationships in the Arctic an adequate investigation of the transport pathways of particulate matter to Station Nord could be performed by using trajectory statistics [Stohl, 1996]. This is a method developed by Stohl et al. [2002] which used a backward Lagrangian particle dispersion model and cluster analysis of the particle position to develop the transport pathways.

Future publication

I had hoped that during this year an article stating my main findings from this thesis could be prepared. I had learnt one important thing: science takes time. Therefore I hope that after submission of this master thesis to the Niels Bohr Institute (NBI), University of Copenhagen, in September 2011, an article related to this thesis will be published.

Bibliography

Andersen, P. (2006, February). Measurement of particulate carbon in relation to traffic and validation of a Particulate Soot Absorption Photometer (PSAP). Master's thesis.

Andreae, M. and A. Gelencser (2006, July). Black carbon or brown carbon? The nature of light-absorbing carbonaceous aerosols. *Atmos. Chem. Phys 6*, 3131–3148.

Andreae, M. O. and P. Merlet (2001, December). Emission of trace gases and aerosols from biomass burning. *Global Biogeochemical cycles 15*, 955–966.

Angell, J. K. (2006, June). Changes in the 300-mb Northe Circumpolar Vortex, 1963-2011. *Jounar of Climate 19*, 2984 – 2994.

Arctic Climate Impact Assessment (ACIA) (2004, November). *Impacts of a warmin Arctic*. Cambridge University Press.

Arctic Monitoring and Assesment Programme (AMAP). *Arctic Pollution 2011*. ISBN-13 978-82-7971-066-0: AMAP, P.O. Box 8100 Dep., N-0032 Oslo, Norway.

Arctic Monitoring and Assesment Programme (AMAP) Working Group (2006). *AMAP Assessment 2006 - Acidifying Pollutants, Arctic Haze, and Acidification in the Arctic*. AMAP, P.O.Box 8100 Dep, N-0032 Oslo, Norway.

Arctic Monitoring and Assesment Programme (AMAP) conference, Copenhagen (2011). The arctic as a messenger for global processes - climate change and pollution.

Bond, T. C., T. L. Anderson, and D. Campbell (1999, June). Calibration and Intercomparison of Filter-Based Measurements of Visible Light Absorption by Aerosols. *Aerosol Science and Technology 30*, 582–600.

Dydkjær, G., R. Tonboe, and L. T. Pedersen (2008, August). Den Arktiske havis. *Vejret 116*, 39 – 46.

Engling, G., C. M. Carrico, S. M. Kreidenweis, J. L. C. Jr, D. E. Day, W. C. Malm, E. Lincoln, W. M. Hao, Y. Iinuma, and H. Herrmann (2006). Determination of levoglucosan in biomass combustion aerosol by high-performance anion-exchange chromatography with pulsed amperometric detection. *Atmospheric Environment 40*, S299–S311.

Engvall, A.-C., J. Ström, P. Tunved, R. Krejci, H. Schlager, and A. Minikin (2009, May). The radiative effect of an aged, internally mixed Arctic aerosol originating from lower-latitude biomass burning. *Tellus*.

Flade Isblink (2011, August). `http://www.flickr.com/photos/stableisotopelab/534842217/in/set-72157600322895583`. Pictures from Greenland, Flade Isblink 2006.

Fritz, J. S. (1987). Ion chromatography. *Analytical Chemistry 59*, 335A–344A.

Gambaro, A., R. Zangrando, P. Gabrielli, C. Barbante, and P. Cescon (2008). Direct determination of levoglucosan at pictogram per milliter level in Antarctic ice by high performance liquid chromatography/electrospay ionization triple quadrupole mass spectrometry. *Anal. Chem. 80*, 1649 – 1655.

Giere, R. and X. Querol (2010, August). Solid Particulate Matter in the Atmosphere. *Elements 6*, 215–222.

Goodsite, M. E., J. M. C. Plane, and H. Skov (2004, February). A Theoretical Study of the Oxidation af Hg^0 to $HgBr_2$ in the Troposphere. *Environ. Sci. Technol 38*, 1772–1776.

Govil, I. M. (2001, June). Proton Induced X-ray Emission - a tool for non-destructive trace elements analysis. *Current science*.

Heidam, N. Z. (1984, September). The components of the arctic aerosol. *Atmospheric Environment 18*, 329–343.

Heidam, N. Z., J. Christensen, P. Wahlin, and H. Skov (2004, March). Arctic atmospheric contaminants in NE Greenland: levels, variations, origins, transport, transformations and trends 1990-2001. *Science of the Total Environment 331*, 5–28.

Heidam, N. Z., P. W. hlin, and J. H. Christensen (1999, January). Tropospheric Gases and Aerosols in Northeast Greenland. *The Atmospheric Sciences 56*, 261–278.

Hirdman, D., J. F. Burkhart, H. Sodemann, S. Eckhardt, A. Jefferson, P. K. Quinn, S. Sharma, J. Ström, and A. Stohl (2010, October). Long-term trends of black carbon and sulphate aerosol in the Arctic: changes in atmospheric transport and source region emissions. *Atmospheric Chemistry and Physics 10*(19), 9351 – 9368.

Horvath, H. (1993). ATMOSPHERIC LIGHT ABSORPTION - A REVIEW. *Atmospheric Environment 27A*(3), 293–317.

Iinuma, Y., O. Böge, R. Gräfe, and H. Herrmann (2010, October). Methylnitrocatechols: Atmospheric tracer compounds for biomass burning secondary organic aerosols. *Environ. Sci. Technol 44*, 8453–8459.

Intergovernmental Panel on Climate Change (IPCC) (2007a). *Changes in Atmospheric Constituents and in Radiative Forcing, The Physical Science Basis. Contribution of Working Group I to the Fourth Assessment Report of the Intergovernmental Panel on Climate Change*.

Intergovernmental Panel on Climate Change (IPCC) (2007b). *Summary for Policymakers, Contribution of Working Group 1 to the 4th Assessment Report*.

Johansen, P., K. Rydahl, J. Christensen, B. Deutch, J. C. Hansen, P. Johansen, F. F. Riget, and K. Vorkamp (2007). *Miljøgifte i Grønland*. Danmarks Miljøundersøgelser, Forlaget Hovedland.

Johansson, T. B., R. E. V. Grieken, J. W. Nelson, and J. W. Winchester (1975, May). Elemental trace analysis of small samples by proton induced x-ray emission. *Analytical Chemistry 47*, 855–860.

K., Q. P., S. G., A. E., D. E., R.-A. T., and G. S. L. (2006, October). Arctic Haze: current trends and knowledge gaps. *Tellius*, 99–114.

Kourtchev, I., T. Ruuskanen, P. Keronen, L. Sogacheva, M. D. Maso, A. Reissell, X. Chi, R. Vermeylen, M. Kulmala, W. Maenhaut, and M. Claeys (2006, December). Determination of isoprene and α-/β-pinene oxidation products in boreal forest aerosols from Hyytiälä, Finland:diel variations and possible link with particle formation events. *Plant Biol. 10*, 138–149.

Kourtchev, I., J. Warnke, W. Maenhaut, T. Hoffmann, and M. Claeys (2008, August). Polar organic marker compounds in PM2.5 aerosol from a mixed forest site in western Germany. *Chemosphere 73*, 1308–1314.

Law, K. S. and A. Stohl (2007, March). Arctic Air Pollution: Orgins and Impacts.

Lemark, A. (2010, June). A study of the Flade Isblink ice cap using a simple ice flow model. Master's thesis.

National Oceanic and Atmospheric Administration (NOAA 2) and U.S. Department of Commerce (2011, May). `http://www.esrl.noaa.gov/psd/cgi-bin/data/composites/printpage.pl`. This webpage were used to generated the Monthly/Seasonal Climate Composites of the 500 mb geopotential height.

National Oceanic and Atmospheric Adminstration (NOAA 1) (2011, May). `http://www.cpc.ncep.noaa.gov/`. This webpage were used to get information of the mode of AO, NAO and P-NAO.

National Snow and Ice Data Center (NSIDC) (2011a, January). `http://nsidc.org/arcticseaicenews/`.

National Snow and Ice Data Center (NSIDC) (2011b, Julys). `http://nsidc.org/news/press/20101004_minimumpr.html`. This articel is covering the Arctic sea ice extent in 2010.

Nielsen, M. J. and J. L. Hansen (2011, July). Station Nord. `http://www.eastgreenland.com/database.asp?lang=eng&num=538`.

Norilsk Nickel (2011, June). `http://www.nornik.ru/en/our_products/polar_divisions/`.

Overland, J. E. (2011, May 3-6). Warm Artic-cold continents:Increased linkages between Arctic climate and sub-Arctic weather. Volume Abstract. Arctic Monitoring and Assesment Programme conference, Copenhagen. Poster 129.

Overland, J. E. and M. Wang (2010). Large-scale atmospheric circulation changes are associated with the recent loss of Arctic sea ice. *Tellus 62A*.

Petzold, A., C. Kopp, and R. Niessner (1997). The dependence of the specific attenuation cross-section on black carbon mass fraction and particle size. *Atmospheric Environment 31*(5).

PhysicalGeography.net (2011, January). Earth-Sun Relationships and Insolation. `http://www.physicalgeography.net/fundamentals/6i.html`.

Pöschl, U. (2003). Aerosol particle analysis: challenges and progress. *Anal. Bioanal. Chem. 375*, 30–32.

Quinn, P., A.Stohl, A. Arneth, T. Berntsen, J. F. Burkhart, J. Christensen, M. Flanner, K. Kupiainen, H. Lihavainen, M. Shepherd, V. Shevchenko, H. Skov, and V. Vestreng (2011). The Impact of Black Carbon on Arctic Climate. Arctic Monitoring and Assesment Programme (AMAP), Oslo.

Quinn, P. K., T. S. Bates, E. Baum, N. Doubleday, A. M. Fiore, M. Flanner, A. Fridlind, T. J. Garrett, D. Koch, S. Menon, D. Shindell, A. Stohl, and S. G. Warren (2008, March). Short-lived pollutants in the Arctic: their climate impact and possible mitigation strategies. *Atmospheric Chemistry and Physics 8*(6), 1723 – 1735.

Rasmussen, E. and J. Turner (2003). *Polar Lows - Mesoscale Weather Systems in the Polar regions*.

Recognized State Climate Office and NC state university (AASC) (2011, May). `http://www.nc-climate.ncsu.edu/climate/patterns/PNA.html`. This webpage were used as litteratur for the behaviour of P-NAO oscialltion.

Saathoff, H., K. Naumann, M. Schnaiter, W. Schöck, O. Möhler, U. Schurath, E. Weingartner, M. Gysel, and U. Baltenseperger (2003, January). Coating of soot and $(NH_4)_2SO_4$ particles of ozonolysis products of α-pinene. *Aerosol Science 34*, 1297–1321.

Schmidt, N. (2003, February). A dry el nino winter. `http://www.climas.arizona.edu/feature-articles/february-2003-Schmidt`. Climate Assessment for the Southwest (CLIMAS), The university of Arizona.

Seinfeld, J. H. and S. N. Pandis (2006). *Atmospheric chemistry and physics - from air pollution to climate change*. ISBN-13: 978-0-471-72017-1: Second Edition, John Wiley & Sons, INC.

Serreze, M. C., M. M. Holland, and J. Stroeve (2007, March). Perspectives on the Arctic's Shrinking Sea-Ice Cover. *Science 315*, 1533 – 1536.

Simoneit, B., J. Schauer, C. Nolte, D. Oros, V. Elias, M. Fraser, W. Rogger, and G. Cass (1999). Levoglucosan, a tracer for cellulose in biomass burning and atmospheric particles. *Atmoshperic Environment 33*, 173–182.

Skov, H., J. H. Christensen, M. E. Goodsite, N. Z. Heidam, B. Jensen, P. W. hlin, and G. Geernaert (2004). Fate of Elemental Mercury in the Arctic during Atmospheric Mercury Depletion Episode and the Load of Atmospheric Mercury to the Arctic. *Environ. Sci. Technol. 38*, 2373–2382.

Skov, H., P. Wåhlin, J. Christensen, N. Z. Heidam, and D. Petersen (2006, March). Measurements of elements, sulphante and SO_2 in Nuuk Greenland. *Atmosperic Environment 40*, 4775 – 4781.

Stohl, A. (1996). Trajectory statistics- a new method to establish source-receptor relationships of air pollutants and its application to the transport of particulate sulfate in europe. *Atmospheric Environment 30*, 579–587.

Stohl, A. (2006, June). Characteristics of atmopsheric transport into the Arctic troposphere. *J. Geophys. Res. 111*(D11306), 1–17.

Stohl, A., S. Eckhardt, C. Forster, P. James, N. Spichtinger, and P. Seibert (2002, June). A replacement for simple back trajectory calculations in the interpretation of atmospheric trace substance measurements. *Atmospheric Environment 36*, 4635–4648.

Ström, J. (2010, June). Specific absorption coefficient, Seasonal variation of OC and EC: Obsercations from the Zeppelin station, Ny Ålesund, Svalbard. Poster at IPY Oslo Science Conference.

Waahlin, P. (2003, August). COPREM - A mulitivariate receptor model with a physical approach. *Atmospheric Environment 37*, 4861 – 4867.

Wallace, J. M. and P. V. Hobbs (2006). *Atmospheric science - An introductory survey*. ISBN-13: 978-0-12-732951-2: Second Edition, Academic Press is an imprint of Elsevier.

Weatherbase (2011, July). `http://www.weatherbase.com/weather/weather.php3?s=21340&refer=&units=metric&cityname=Nord-Greenland`.

Weingartner, E., H. Saathoff, M. Schnaiter, N. Streit, B. Bitnar, and U. Baltensperger (2003, May). Absorption of light by soot particles: determination of the absorption coe cient by means of aethalometers. *Aerosol Science 34*, 1445–1463.

Yao, X., T. Horie, S. Xue, H.-Y. Leung, M. Katsuhara, D. E. Brodsky, Y. Wu, and J. I. Schroeder (2010, January). Differential Sodium and Potassium Transport Selectivities of the Rice $OsHKT_{2;1}$ and $OsHKT_{2;2}$ Transporters in Plant Cells[1[C][OA]].

Yttri, K. E., W. Aas, A. Bjerke, J. N. Cape, F. Cavalli, D. Ceburnis, C. Dye, L. Emblico, M. C. Facchini, C. Foster, J. E. Hanssen, H. C. Hansson, S. G. Jennings, W. Maenhaut, J. P. Putaud, and K. TÃ¸rseth (2007). Elemental and organic carbon in PM_{10}: a one year measurement campaign within the European Monitoring and Evaluation Programme EMEP.

Appendix A

Figure

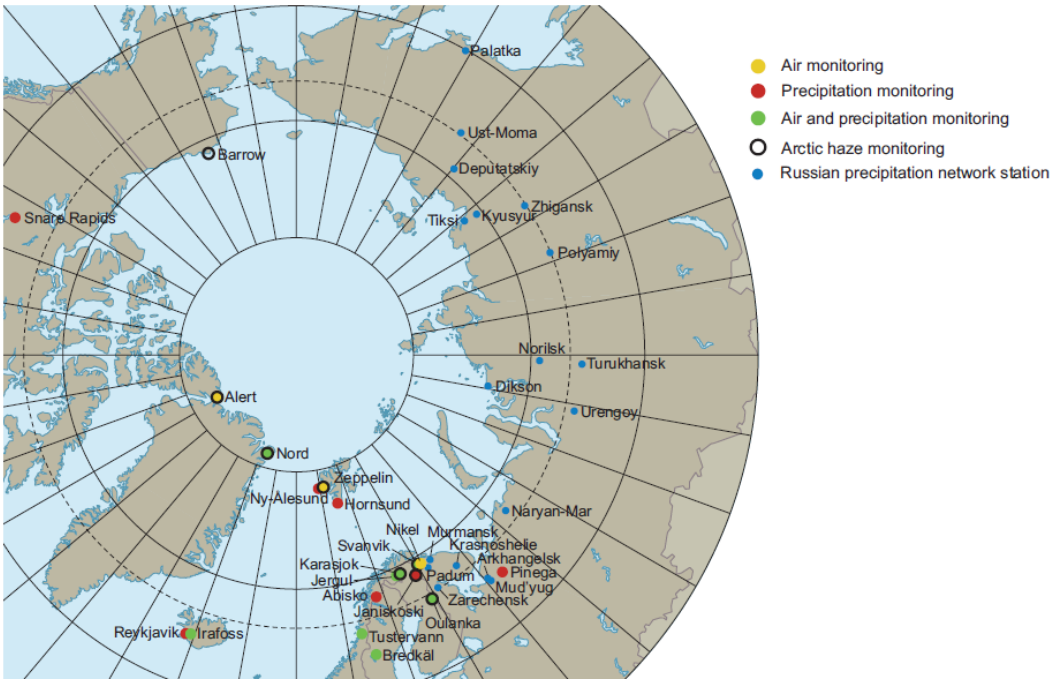

Figure A.1: The locations of monitoring station for chemical elements and arctic haze as well as precipitation within the Arctic region [AMAP 2006].

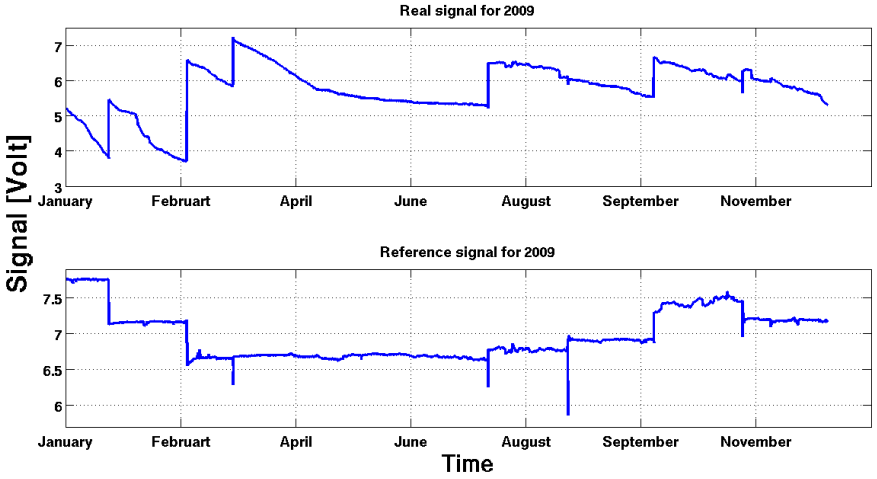

(a) Voltages signal for 2009

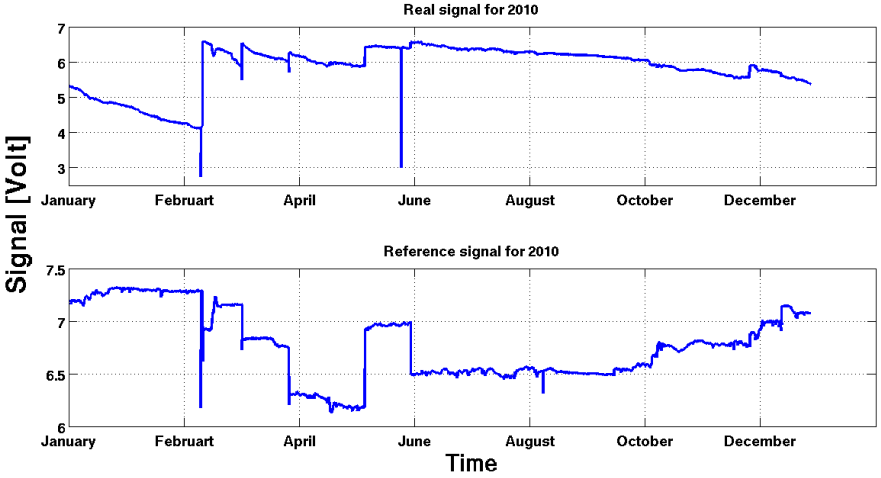

(b) Voltages signal for 2010

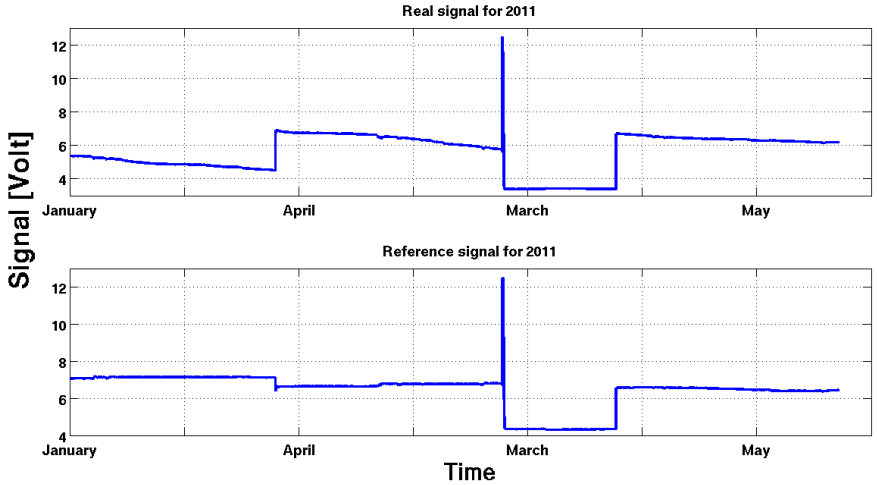

(c) Voltages signal for 2011

Figure A.2: The PSAP voltage signals S and RS from January 2009 to April 2011.

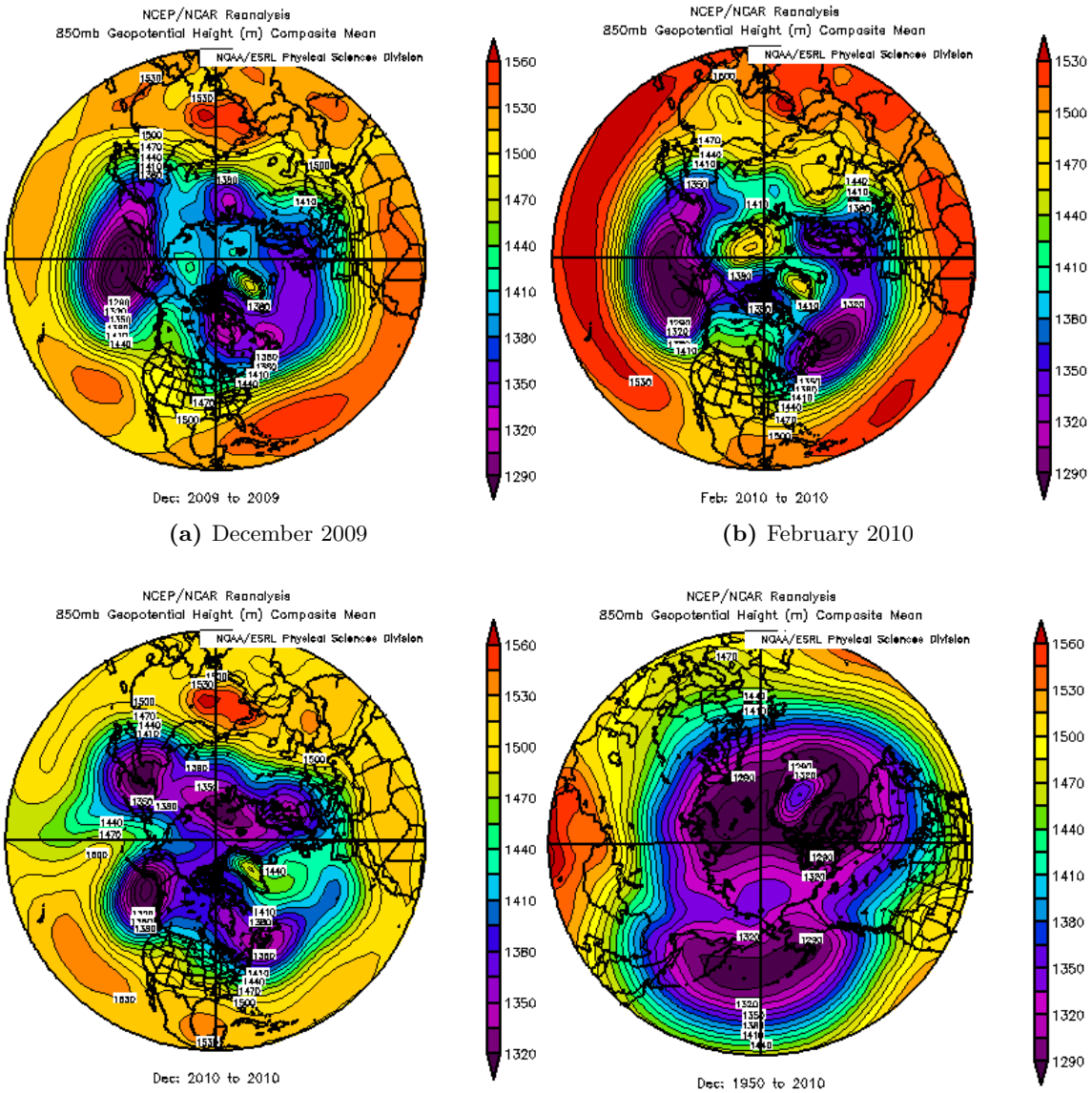

(a) December 2009 **(b)** February 2010

(c) December 2010 **(d)** Climatology

Figure A.3: Arctic Atmospheric Pressure $850\,\mathrm{mb}$ geopotential height-contours observed for (a) December 2009, (b) February 2010 and (c) December 2010, which is the months where the Polar Vortex brake down. (d) is the $850\,\mathrm{mb}$ geopotential height-contours observed for December 1950-2010, which indicated a "normal" PV [National Oceanic and Atmospheric Administration (NOAA 2) and U.S. Department of Commerce, 2011].

Appendix B

Code

B.1 Static exercise

This exercise was in order to give some experience of how different dataset behaviour. In exercise nr. 1 a uniform normally distributed dataset were use for making a histogram fitted to a Gaussian function and to make a plot of the *Cumulative Distribution Function (CDF)*. In exercise nr. 2 there were added a series of numbers and in exercise nr. 3 there were added some outliers to the uniform normally distributed dataset. The histogram fitted with a Gaussian function and the CDF for the 3 different exercises is shown in figure B.1 and B.2. The Matlab script for the exercises is found below figure B.2.

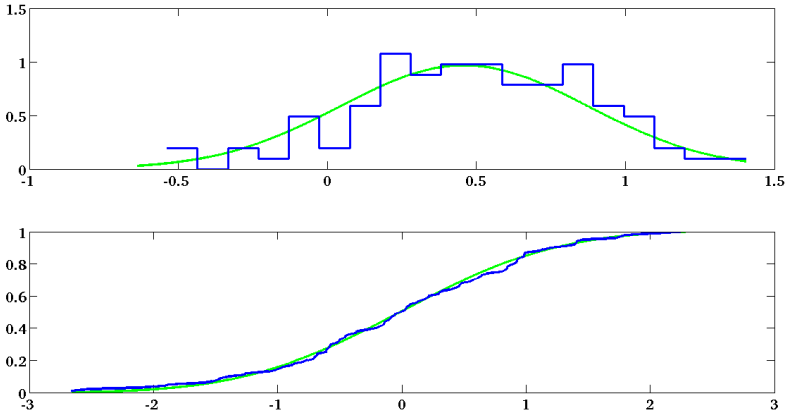

Figure B.1: The plots from the first static exercise.

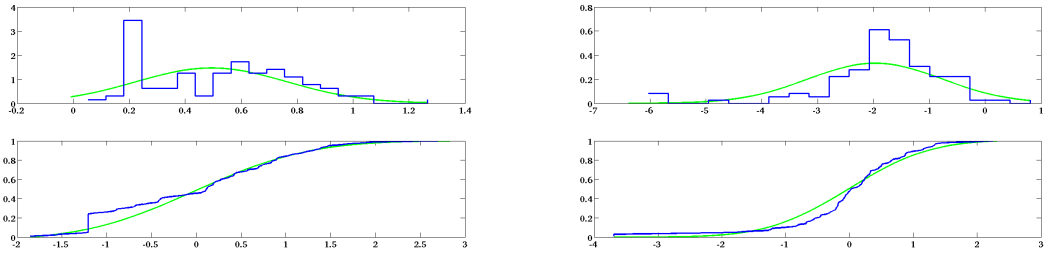

(a) Exercise 2 **(b)** Exercise 3

Figure B.2: The plots from the static exercise 2 and 3.

```
%%%%%%%%%% The Dataset for Exercise nr. 1
% Make a random dataset, where rand produce uniformly distributed ...
    numbers
% and randn produce normally distributed numbers.
par = rand(1,2);
my = par(1); %Mean
sigma = par(2); % SD
NN = 100  ; % Amount of numbers in the dataset
x = sigma * randn(1,NN) + my; % The dataset

%%%%%%%%%% The Dataset for Exercise nr. 2
par1 = rand(1,2,3,4);par = rand(1,2);
my = par(1);
sigma = par(2);
NN = 100  ;

beta = 0.2; %par1(1);
x0 = par1(2);
my = par1(3);
sigma = par1(4);
m = floor(NN*(1-beta));

x(1:m) = sigma *randn(1,m) + my;
x(m+1:NN) = x0*ones(1,NN-m);

%%%%%%%%%% The Dataset for Exercise nr. 3
par = randn(1,2);
my = par(1);
sigma = par(2);
NN = 100;

x = sigma * randn(1,NN) + my;
x(1:3) = 5*sigma * ones(1,3) + my;

%%%%%%%%%% The script for making the Histogram and CDF.

nbin = 20; % Amounts of bins in one hist.
Xmin = min(x); % Def. the min and max of x
Xmax = max(x);
db = (Xmax - Xmin) / (nbin); % \Delta bins
bin = zeros(1,nbin); % A matrix with zeros, in order to run the ...
    script farster.

% The index def. the numbers of datapoints in the different hist.
for i = 1:NN
```

```
44
45      index =  floor(((x(i) - Xmin)/(Xmax -Xmin)) * (nbin -1) +1 );
46      bin(index) = bin(index) + 1;
47
48 end
49
50 bin = bin / (NN*db);
51 sigmax = std(x); % SD of x
52 meanx = mean(x); % Mean of x
53 M=1000; % Make a smoother plot
54 x1 = ((1:M)/M) *nbin * db + Xmin ;
55
56 % ni def. the normalized PDF
57
58 ni = (1 / (sqrt(sigmax^(2) *2*pi))) * (exp(- (x1 - meanx).^(2) / (2 *...
       sigmax^(2) )));
59
60 %%%%%%%%% Make a histogram
61 figure(1);
62 x2=Xmin + db * (1:nbin);
63
64 subplot(2,1,1), plot(x1,ni,'g');
65 hold on
66 subplot(2,1,1), stairs(x2,bin);
67 hold off
68
69 %%%%%the Cumulative Distribution Function
70
71 ini = ni; % the integrale of the normalized PDF
72
73 for j = 2:M
74
75    ini(j) = ini(j-1) + ni(j);
76
77 end
78
79 ini = ini / ini(M);
80
81 subplot(2,1,2),plot((x1-meanx)/sigmax,ini,'g');
82 hold on
83 subplot(2,1,2), plot((sort(x)-meanx)/sigmax, ((1:NN) /NN));
84 hold off
```

B.2 The Grubb's test

The Grubb's test is a statistical test, which is used to detect outliers in a dataset, which is assumed to be normally distributed. Our measurements are not normally distributed, but log-normally distributed. Though the measurements differ from a normally distribution, the outliers were investigated by the Grubb's test. The Grubb's test is defined as:

$$G = \frac{max_{i,..,N}|x_i - \mu|}{\sigma}$$

Here μ and σ is denoting the mean and the standard deviation of the data x_i, respectively. The test is defining the largest absolute deviation from the mean in

units of the standard deviation (maximum).
The value for rejecting a data-point or the hypothesis of no outliers at a significance level σ is determined by:

$$G > \frac{N-1}{\sqrt{N}} \sqrt{\frac{(t_{test})^2}{N-2+(t_{test})^2}}$$

Here N is the number of data-points, $N-2$ is the degrees of freedom and t_{test} is the critical value of the student's t-distribution at a significance level σ divided by $2N$. The student's t-distribution is defined as:

$$t_{test} = \frac{\Gamma\left(\frac{v+1}{2}\right)}{\sqrt{v\pi} \cdot \Gamma\left(\frac{v}{2}\right)} \cdot \left(1 + \frac{t^2}{v}\right)^{-\frac{1}{2}(v+1)} \tag{B.1}$$

here is $v = N-2$ the number of degree of freedom, Γ is the gamma function and $t = \frac{\alpha}{2N}$. In this analysis is the significance level assumed to be equally $\sigma = 0.01$.
The test were performed on the concentrations of BC, OC, EC, TC and Levoglucosan and below the Matlab script for the test is found.

```
%%%%%%%%%%%%%%%%% The Grubb's test
% Defines variable
v = NN-2; % The number of degrees of freedom
alpha = 0.05; %level of significance
t = alpha/(2*NN); % two-sided test

% Estimates the critical value G by the inverse of Student's T ...
    cumulative distribution function (CDF).
ttest = tinv(t,v);

G = (NN-1) / (sqrt(NN)) * sqrt(ttest^(2)/((NN-2) + ttest^(2)))

Gmax = (TCmax - meanx) / sigmax

Gmin = abs(TCmin - meanx) / sigmax
```

Appendix C

Publications and presentations

Published

Poster AMAP conference, Mai 2011, Denmark, Copenhagen *Observation of carbonaceous anthropogenic tracers at the high Arctic site Station Nord, Northern Greenland* Grube, A G., Nguyen, Q., Nøjgaard, J. K., Bossi, R., Skov, H., Sørensen, L. L., Jensen, B., Massling, A. (2011). The Poster is found in figure C.2.

Poster AMAP conference, Mai 2011, Denmark, Copenhagen *Source to receptor analysis of anthropogenic species at the high Arctic site Station Nord, Northern Greenland* Nguyen, Q., Grube, A. G., Massling, A., Skov, H., Sørensen, L. L., Bossi, R., Jensen, B., Nøjgaard, J. K. (2011)

Poster The International Aerosol Conference, August 29 - September 3 2010, Helsinki, Finland *Observations and model results of soot-containing particulate matter at the higher Arctic site St. Nord* Grube, A. G., Skov, H., Sørensen, L. L., Christensen, J., Wåhlin, P., Bossi, R., Nguyen, Q., Nøjgaard, J. K., Jensen, B., Kristensen, K., Fenger, M., Glasius, M., Massling, A. (2010). The Poster is found in figure C.1.

Other significant conference contributions

Talk AMAP conference, Mai 2011, Denmark, Copenhagen *Measurements of air pollution at Station Nord, North East Greenland* Skov, H., Bossi, R., Christensen, J., Glasius, M., Grube, A. G., Hansen, K. M., Jensen, B., Massling, A., Nguyen, Q., Nøjgaard, J. K., Sørensen, L. L. (2011)

Talk CRAICC kick-off meeting, Nordic centre of Excellence February 2011, Helsinki, Finland *Physical particle measurements at a high Arctic site in Northern Greenland: Present measurements and future plans* Massling, A., Skov, H., Glasius, M., Christensen, J., Grube, A.G., Nguyen, Q., Sørensen, L. L., Bossi R., Nøjgaard, J. K. (2011)

Observations and model results for soot-containing particulate matter at the higher Arctic site St. Nord.

Anna Grube[1], Henrik Skov[1], Lise Lotte Sørensen[1], Jesper Christensen[1], Peter Wåhlin[1], Rosanna Bossi[1], Quynh Nguyen[1,2], Jacob K. Nøjgaard[1], Bjarne Jensen[1], Marlene Fenger[2], Kasper Kristensen[2], Marianne Glasius[2] and Andreas Massling[1]

[1]Department of Atmospheric Environment, National Environmental Research Institute, University of Aarhus, 4000 Roskilde, Denmark,
[2]Department of Chemistry, University of Aarhus, 8000 Aarhus C, Denmark.

Aim
To identify the sources and transport patterns of Black Carbon into the Arctic and in particular to Greenland.

Introduction
The Arctic is warming with twice the rate of the rest of the Earth (*Hassol, 2004*). It is expected that due to this large temperature increase the clearest signals in terms of a compositional change of air pollution can be observed in the Arctic. The compositional change is based on the presence of greenhouse gases and on aerosol particles. Long range transported aerosol particles have a large influence on Earths' radiation budget in the Arctic in terms of their direct effect and their indirect effect. Furthermore the deposition of Black Carbon to snow and ice leads to acceleration of the melting of ice.

Therefore it is very important to determine the concentration and sources of Black Carbon to the Arctic area.

References
Hassol, S. J. (2004): ASIA, Impacts of a Warming Arctic, ARC-TIC CLIMATE IMPACT ASSESSMENT. "Cambridge University Press".
*Wåhlin, P. (2003):*COPREM- A multivariate receptor model with a physical approach. Atmos. Environ. 37, 4861-4867.

Acknowledgement
The Danish Environmental Protection Agency financially supported this work with means from the MIKA/DANCEA funds for Environmental Support to the Arctic Region. The findings and conclusions presented here do not necessarily reflect the views of the Agency. The Royal Danish Air Force is acknowledged for providing free transport to Station Nord, and the staff at Station Nord is especially acknowledged for excellent support.

Studying site
Flygers Hut at Station Nord, North East Greenland: 81° 36' N, 16° 40' W, 25 m ASL.
Flygers Hut is equipped with a series of inlets for measuring gasses and particles.
In Table 1 ongoing measurements in Flygers Hut are listed.

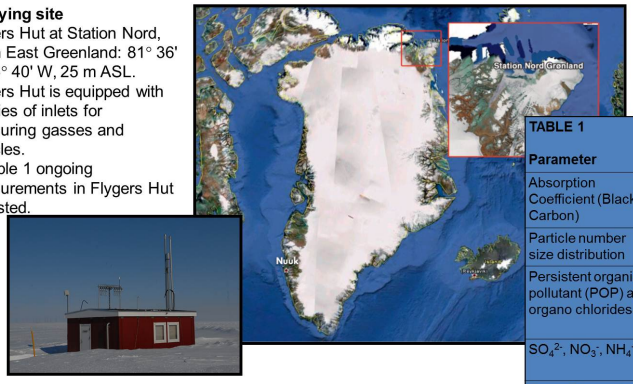

TABLE 1 Parameter	Instru-ment	Time res.
Absorption Coefficient (Black Carbon)	PSAP	1 day
Particle number size distribution	SMPS	1 hour
Persistent organic pollutant (POP) and organo chlorides	GC-MS	1 week
SO_4^{2-}, NO_3^-, NH_4^+	Chroma-tography	1 week
Trace Elements (>Al)	PIXE	1 week
GEM	Tekran	30 min.
Ozone	Gas monitor	30 min.
NOx	Gas monitor	30 min.

In Figure 1 changes in the concentration during the year 2008 for different chemical species and Black Carbon are shown. The correlation coefficient between Black Carbon and the different chemical species is shown in Table 2.

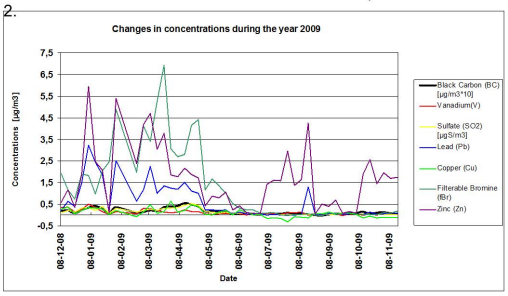

TABLE 2 Parameter	Correlation coefficient
BC / Sulfate	0.9166
BC / Pb	0.7387
BC / Br	0.7041
BC / Cu	0.6737
BC / V	0.5714
BC / Zn	0.4551

RESULTS
- Increase in concentration from early November.
- Decrease in concentration in the late spring.
- Sulfate and Vanadium is following the same pattern as Black Carbon.

Methods
To determine the sources of Black Carbon in Arctic the COnstrained Physical REceptor Model (COPREM) was used (*Wåhlin, 2003*). The first preliminary results of sources for Black Carbon and Sulfate are shown in the figure below.

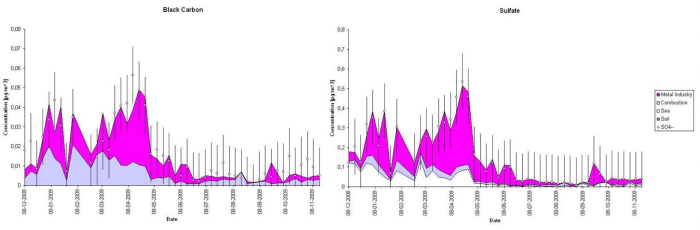

RESULTS
- The contribution from metal industry and combustion can not explain all the Black Carbon completely - indication that there must be other sources – possibly wildfires.
- Metal industry largely contributes to sulfate concentrations at Station Nord.

NATIONAL ENVIRONMENTAL RESEARCH INSTITUTE
AARHUS UNIVERSITY

Future work
The next step is to complete the picture of the combustion sources contributing to Black Carbon using the COPREM model.
Furthermore, we will determine the transport patterns and source areas for Black Carbon, this will be done by cluster analysis of back – trajectories.

Figure C.1: The Poster was presented at the International Aerosol Conference, August 29 - September 3 2010, Helsinki, Finland.

Observations of Black Carbon and Elemental Carbon at the high Arctic site Station Nord, Northern Greenland

Grube[1], Anna G., Nguyen[1,2], Quynh T., Nøjgaard[1], Jacob K. , Bossi[1], Rossana, Skov[1], Henrik, Sørensen[1], Lise Lotte, Jensen[1], Bjarne, Glasius[2], Marianne and Massling[1], Andreas

[1]Department of Atmospheric Environment, National Environmental Research Institute, University of Aarhus, 4000 Roskilde, Denmark,
[2]Department of Chemistry, University of Aarhus, 8000 Aarhus C, Denmark.

Mail: agg@dmu.dk

Aim

The aim of the study is to measure particulate matter in the high Arctic in order to enhance the understanding of aerosol transport pathways to the Arctic.

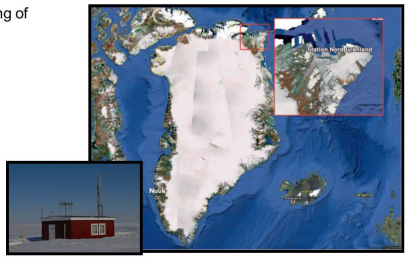

Introduction

Long range transported aerosol particles have a large influence in the Arctic; their direct effect and their indirect effect leads to a large influence on Earth's radiation budged in the Arctic; the deposition of Black Carbon (BC) and Elemental Carbon (EC) to snow and ice leads to acceleration of the melting of ice.

Since Arctic is very sensitive to changes in temperature it influences the extension of ice-cover and snow-cover. This change will in turn influence the surface reflection (albedo) drastically and enhance the temperature increase further (ACIA 2004; IPCC 2007; Quinn et. Al(2008)).

The dynamics processes controlling BC and EC in the high Arctic are speculative. Therefore is it very important to study the behavior of particulate matter In the Arctic.

References

ACIA report (2004), Arctic Climate Impact Assessment, Assessment report, Cambridge University Press.

IPCC report. (2003), International Panel on Climate Change, Assessment report, Cambridge University Press.

Quinn et. Al (2008),"Warming in the Arctic since Pre-Industria l Times".

Acknowledgement

This work was supported by AMAP (Arctic Monitoring Assessment Program, Aarhus University Research Foundation) and DANCEA (Danish Cooperation for Environment in the Arctic). The Royal Danish Air Force is acknowledged for providing free transport to Station Nord, and the staff at Station Nord is especially acknowledged for excellent support.

Method and studying site

Flygers Hut at Station Nord, North East Greenland (81° 36' N, 16° 40' W, 25 m ASL.), is equipped with a series of inlets for measuring gasses and particles.
Since March 2008, daily observations of aerosol light absorption has been conducted using a PSAP- instrument at 550nm. For the same time period, weekly samples have been collected by a High-Volume Sampler (HVS) inside Station Nord, on a quartz fibre filters. Subsequently, they were analyzed for organic and elemental carbon. The analysis was conducted using the thermo-optical method.

Concentrations

The figure below shows changes in the concentration of BC from March 2008 to February 2011 and changes in concentration of sulphate from March 2008 to December 2009. Besides the seasonal pattern, it is seen that the increase in concentration is coincides with events of strong North Circumpolar Vortex. The North Circumpolar Vortex is shown for a mean of December, January, February in 2008, 2009 and 2010, where 2008 were the strongest vortex.

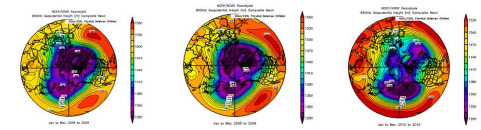

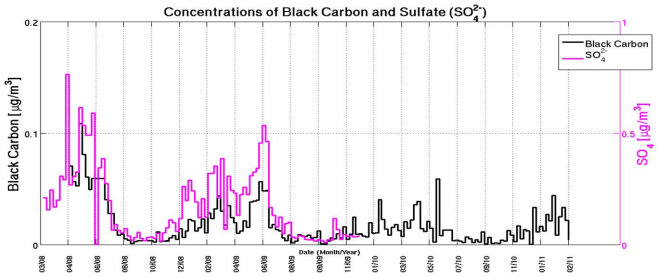

TABLE 1 Parameter	Correlation
BC / Sulfate	0.8803
BC / Br	0.6960
BC / Mn	0.6797
BC / Pb	0.6360
BC / Se	0.5829
BC / Zn	0.4266

Specific absorption coefficient

The figure below present the time series of weekly EC samples collected on quartz fibre filters and analysed by the thermo-optical method, and the weekly BC which is the averaged PSAP data using a specific absorption coefficient of 10 $m^2\ g^{-1}$.

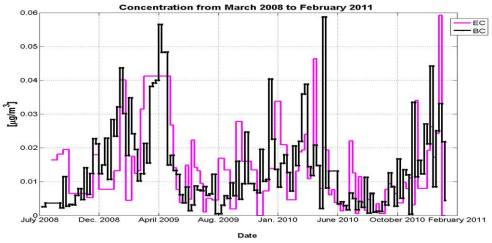

The figure below shows a scatter plot of the EC and BC concentrations with a specific absorption coefficient of 10 m2/g. The slope is very close to 1and the t-test confirms no significant difference between BC and EC.

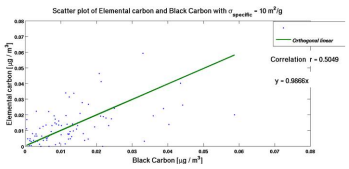

Conclusion

The transport of anthropogenically originated particles to the Arctic is observed at Station Nord showing a typical seasonal pattern. An increase of particulate mass concentrations of Black Carbon (BC) start in November and declines in the late spring of the following year. The same behaviour is observed for the particulate mass of sulphate and other anthropogenic originated metals as Bromine (Br), Led (Pb), Manganese (Mn) (Table 1).

NATIONAL ENVIRONMENTAL RESEARCH INSTITUTE
AARHUS UNIVERSITY

Figure C.2: The Poster was presented at the Arctic Monitoring and Assesment Programme (AMAP) conference, May 3rd-6th 2011, Copenhagen, Denmark.